University of Tennessee, Knoxville
TRACE: Tennessee Research and Creative Exchange

Doctoral Dissertations | Graduate School

8-2018

Characterization of Radiation Effects and *Ab Initio* Modeling of Defects in a High Entropy Alloy for Nuclear Power Application

Congyi Li
University of Tennessee, cli26@vols.utk.edu

Follow this and additional works at: https://trace.tennessee.edu/utk_graddiss

Recommended Citation

Li, Congyi, "Characterization of Radiation Effects and *Ab Initio* Modeling of Defects in a High Entropy Alloy for Nuclear Power Application. " PhD diss., University of Tennessee, 2018.
https://trace.tennessee.edu/utk_graddiss/5005

This Dissertation is brought to you for free and open access by the Graduate School at TRACE: Tennessee Research and Creative Exchange. It has been accepted for inclusion in Doctoral Dissertations by an authorized administrator of TRACE: Tennessee Research and Creative Exchange. For more information, please contact trace@utk.edu.

To the Graduate Council:

I am submitting herewith a dissertation written by Congyi Li entitled "Characterization of Radiation Effects and *Ab Initio* Modeling of Defects in a High Entropy Alloy for Nuclear Power Application." I have examined the final electronic copy of this dissertation for form and content and recommend that it be accepted in partial fulfillment of the requirements for the degree of Doctor of Philosophy, with a major in Energy Science and Engineering.

Brian D. Wirth, Steven J. Zinkle, Major Professor

We have read this dissertation and recommend its acceptance:

Takeshi Egami, Maik K. Lang, Geroge Stocks

Accepted for the Council:

Dixie L. Thompson

Vice Provost and Dean of the Graduate School

(Original signatures are on file with official student records.)

Characterization of Radiation Effects and *Ab Initio* Modeling of Defects in a High Entropy Alloy for Nuclear Power Application

A Dissertation Presented for the
Doctor of Philosophy
Degree
The University of Tennessee, Knoxville

Congyi Li
August 2018

ACKNOWLEDGEMENTS

I'd like to express my sincerest gratitude to all who have contributed and supported my graduate career. I would first like to thank to my major academic advisors, Dr. Steve Zinkle and Dr. Brian Wirth, for providing interesting and challenging research topics and for their kind, patient and consistent guidance throughout my six year graduate career. They also instilled their enthusiasm and prudence in nuclear material research in me through lectures, academic discussions and casual conversations. These qualities are invaluable in my growth as an independent researcher.

My research involves collaborations with numerous researchers at both the University of Tennessee and Oak Ridge and Lawrence Livermore National Labs. These collaborations have been crucial for the successful completion of my PhD research. I'd like to first express my thanks to three collaborators who put a significant amount of effort and time to help me climb over the obstacles in my research:

- Dr. Malcolm Stocks showed me the beauty of multiple scattering theory and taught me how the theory can be used to solve the complex magnetic structures of random solid solution alloys.

- Dr. Xunxiang Hu taught me positron annihilation spectroscopy, and also how to conduct safe and reliable experiments in a National Lab environment.

- Dr. Phil Sterne taught me the physics behind positron annihilation spectroscopy and showed me bit by bit how to perform theoretical calculations for positron annihilation observables.

I would also like to appreciate the contribution from other excellent collaborators; Dr. Brian Sales helped me experimentally measure the magnetic susceptibility of the high entropy alloy. Dr. Silva Chinthaka helped me obtain good quality X-ray diffraction patterns from samples of very small size. Dr. NAP Kiran Kumar and Dr. Tengfei Yang helped me perform transmission electron microscopy on ion and neutron irradiated samples. Dr. Junqi Yin conducted Monte Carlo simulation and helped me calculate the temperature dependence of magnetic susceptibility of the high entropy alloy. Without their assistance and work, I could not accomplish this comprehensive PhD research project involving both intensive experimental and modeling work.

The experimental characterization of neutron-irradiated samples was all conducted at the Low Activation Materials Development and Analysis (LAMDA) laboratory in Oak Ridge National Lab (ORNL). Thus, I would like to express my special thanks to the lab manager, Joshua Schmidlin, and the technicians for teaching me how to safely handle samples with residual radioactivity and for trusting me to work independently in the lab. Also, I acknowledge the funding support for this neutron irradiation study. The initial HEA sample preparation and neutron irradiation was supported by the Office of Fusion

Energy Sciences, U.S. Department of Energy, under contract DE-AC05-00OR22725 with UT-Battelle, LLC. The post irradiation characterization of the neutron irradiated samples in LAMDA was supported by the Office of Fusion Energy Sciences under the ORNL base program contract. Finally, I wish to acknowledge ORNL fusion materials program manager, Dr. Yutai Katoh, for supporting my research activities.

The computational studies were accomplished mainly at three computing facilities; the NEWTON supercomputer at University of Tennessee, Knoxville (UTK), the EDISON supercomputer at National Energy Research Scientific Computing Center (NERSC) and the JORVIK computing cluster at ORNL. I would like to thank Dr. Brian Wirth and Dr. Malcolm Stocks for offering the access to these computing resources. As well, I sincerely appreciate the support from the technical staff members at UTK and NERSC.

To my colleagues at UTK, I would like to thank Dr. Guiyang Huang for help with teaching me how to perform ab initio calculation and Daniel Clark for his help on preparing ion irradiation experiments and conducting nano-indentation experiments.

I also wish to acknowledge the comments and advice on my PhD thesis proposal and my PhD research project from my committee members, Dr. Takeshi Egami and Dr. Maik Lang.

I gratefully acknowledge the financial support from Dr. Steve Zinkle's Governor's Chair appointment, and from the Bredesen Center's fellowship program directed by Dr. Lee Riedinger. Also, I would like to thank the administrative support from Wanda Davis, Tracey Bucher and Jessica Garner at Bredesen Center. Their administrative and financial support have enabled me to pursue this research project.

Outside the research community, I would also like to thank my best friends in the United States who were willing to be at my side and offer help in the most challenging time of my graduate life. Their understanding, caring and love are precious treasures in my life.

Finally, I would like to express my deepest gratitude to my entire family, especially my parents. Their unconditional love, support and encouragement have empowered me in my whole graduate life to confront challenges and accomplish tasks that I alone would not have thought possible. I am always indebted to them, and with love, I dedicate this dissertation to them.

ABSTRACT

A novel Co-free NiFeMnCr HEA was synthesized for both ion and neutron irradiation studies. 3 and 5.8MeV heavy ion irradiations were conducted at room temperature and 400 – 700 ˚C from 0.03 to 10dpa. Post-irradiation examination included x-ray diffraction, nanoindentation hardness and transmission electron microscopy. The HEA exhibited quantitatively superior radiation resistance than conventional alloys, including suppressed void swelling and solute segregation.

Neutron irradiation was conducted at 60 ˚C from 0.1 to 1dpa. Microhardness, electrical resistivity and positron annihilation spectroscopy measurements were performed at room temperature before and after isochronal annealing up to 700˚C on the neutron-irradiated samples. The HEA retains fundamental stability after neutron irradiation. Compared with metals and conventional alloys, the HEA showed similar annealing trend of hardness and vacancy-type of defects. On the other hand, this HEA showed unique annealing trend of electrical resistivity. The large radiation induced resistivity increase (>10 μΩ·cm) did not recover up to 700 ˚C, suggesting short range ordering phenomena may be critical in radiation effects of HEA.

In parallel, *ab initio* modeling was conducted to establish a solid foundation for multi-scale modeling of HEA as well as to reveal unique defect physics of HEA. Magnetic structure was computed based on coherent potential. Vacancy energetics were computed by Vienna *Ab initio* Simulation Package (VASP). Modeling results shows that it is reasonable to neglect magnetic interactions. The statistical distribution of vacancy formation energy is weakly dependent upon either the chemical species of the atom site associated with the vacancy, or local chemical environment. The calculated migration energy values show a large spread, varying between 0.55 to 1.68eV, although the mean value is comparable to that of conventional austenitic alloys. Finally, positron lifetime of bulk HEA, mono-vacancy and small vacancy clusters were computed by a finite element based *ab initio* package to facilitate the interpretation of experimental results from positron annihilation spectroscopy.

TABLE OF CONTENTS

LIST OF TABLES

LIST OF FIGURES

CHAPTER ONE
INTRODUCTION

1.1 Enhanced radiation resistant material for advanced nuclear power technology

Many great changes in human civilization are realized by the invention of new energy technologies. During the industrial revolution, steam engines provided humans with power far beyond animals. The harnessing of electric power brings humans cleaner and more efficient lighting into every household. Nowadays, homes can be kept warm in winter and cool in summer. People all over the world are connected by modern transportation systems. Space exploration is no longer a dream and we are obtaining more and more knowledge regarding not only Earth, but also other planets. All of these accomplishments are impossible without the advancement of energy technologies.

Looking to the future, energy technologies face a two-fold challenge. According to the International Energy Agency (IEA)[1], it is projected that the consumption of energy would increase from 12 billion tonne oil equivalent (toe) in 2009 to 17 or 18 billion toe by 2035 based on new versus the current policy scenario, respectively. Carbon dioxide emission would accordingly increase from 29 gigatonnes (Gt) per year to 36 or 43 Gt per year based on new or current policy. On one hand, meeting this rapid growing demand would require more effective and efficient use of energy, such as increasing the efficiency of current solar panels, wind turbines and coal/gas/nuclear power plants. On the other hand, to reduce the emission of carbon dioxide and other greenhouse gases, the energy sector need to transition from the traditional fossil fuel to clean energy resources, such as solar, wind, hydro, biomass and nuclear (or alternatively, develop massive-scale carbon sequestration systems).

For nuclear energy, proposed Generation IV fission and fusion reactors are a group of advanced nuclear reactor designs currently researched for commercial application. These design concepts offer better fuel efficiency, higher safety margins or fewer nuclear proliferation issues than current commercial designs. However, these advanced designs all require structural materials to operate in harsher environments. Figure 1.1 shows a comparison of operating conditions for in-core structural materials between current Generation II-III technology and advanced nuclear reactor designs[2]. All advanced reactor designs require higher operating temperatures, and many of them require materials to function properly after higher radiation doses than current Generation II-III nuclear power reactors. However, other than the alloys in nuclear fuel cladding or steam generator, very few new materials have been introduced in the construction of nuclear power reactors[3]. The structural components in Generation III light water reactors, which are currently under construction in US and China, are still largely based on alloys developed in the 1960s. These alloys are known to have severe degradation issues at

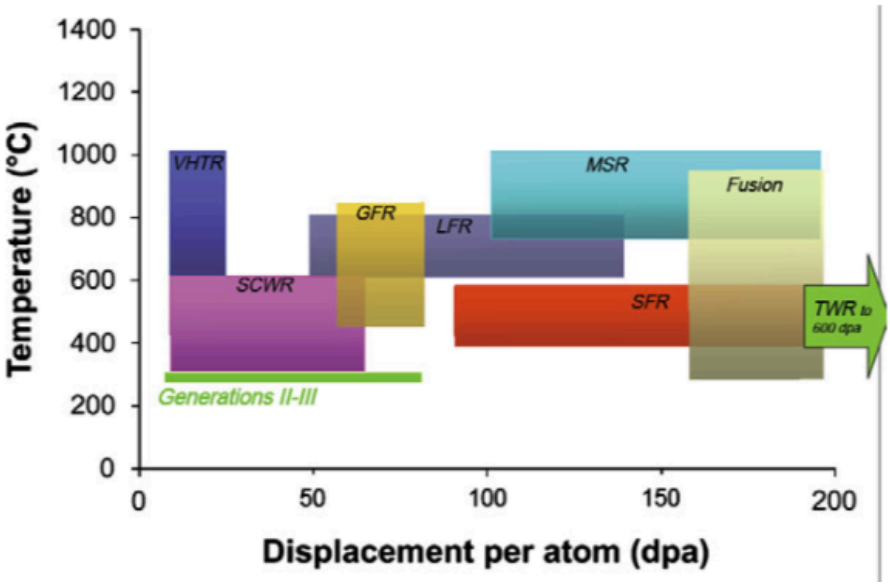

Figure 1.1 Comparison of temperature and dose requirements for the in-core structural materials between current commercial nuclear power reactors (Generation II - III) and advanced fission and fusion technologies, as reproduced from Ref [2].

large neutron damage dose or higher operating temperatures. Therefore, innovations need to take place in nuclear material research and development to realize the advanced reactor concepts with reliable radiation-resistant structural materials.

Several guidelines have been proposed for the development of enhanced radiation tolerant materials[4, 5]. One innovative path is to explore beyond the concept of conventional alloys. Conventional alloys generally consist of one predominant matrix element and several minor alloying elements, such as steel, zircaloy and Ni-based superalloy. To achieve superior mechanical behavior, they are typically designed to have multiple phases. Previous experience and knowledge in physical metallurgy indicate multiple phases would generally form with the increasing number of alloying elements due to a high probability that some of the different elements will have strongly attractive chemical interactions. However, recent experimental work of Yeh[6] and Cantor[7] have shown that several alloys consisting of five or more elements in equimolar or near equimolar ratio can form simple single phase structure, such as face-centered cubic (f.c.c) and body-centered cubic (b.c.c). The scientific basis responsible for formation of single phase alloys from large numbers (>4 to 5) of constituent elements is currently under debate[8-11]. One hypothesis is that the complex composition of the alloy results in high entropy, thus suppressing the formation of intermetallics that normally occur due to enthalpy considerations and stabilizing the single-phase microstructure. The most apparent source of entropy is configurational entropy. Also, depending upon the alloy composition and temperature, other sources may contribute to the overall entropy, such as

atomic vibration, electronic and magnetic excitation[12]. This type of new alloy is therefore named compositionally-complex alloy, or high entropy alloy (HEA).

This new type of alloy has also drawn considerable interest from nuclear material scientists due to its well-balanced combination of material properties, such as good mechanical strength and corrosion resistance. However, it is unclear whether the HEA microstructure remains stable upon irradiation since there are only very limited irradiation experiments studies on HEAs. Ultimately, the microstructure stability of a material under irradiation is determined by point defect and defect cluster properties and the diffusive evolution and fate of these defects. Due to the unique properties of HEAs, such as lattice displacement and chemical disordering, conventional theory of defects in alloys will not always apply for HEAs. New models need to be established from the very fundamental level to facilitate the understanding of radiation effects in HEA.

1.2 Key Properties of HEAs

The history of HEAs is relatively short. JW Yeh first described this material concept in 1996, but the new alloy did not draw much attention from researchers until 2004 when independent journals published papers by JW Yeh[6] and B Cantor[7], respectively. The term "HEA" was also coined by Yeh in the 2004 paper when he attributed the formation of the new alloy to the high configurational entropy. A general definition of HEA was also given in the paper as alloys composed of "five or more principal elements, with the concentration of element being between 5% and 35%". However, the definition is fairly loose in the HEA field and alloys composed of four elements at near-equimolar ratio can also form single-phase solid solution, and can be considered as HEA. Yeh's paper also highlighted the high temperature strength and stability of a list of HEAs and pointed out the grand possibility of HEAs due to huge number of alternate element combinations. On the other hand, Cantor's paper highlighted the microstructure of equimolar, single f.c.c phase FeCrMnNiCo.

Extensive research following these two pioneering papers tried to explore other possible HEA compositions. However, despite the huge number of alternative element combinations, to date only three major groups of element combinations have been discovered to exhibit simple single phase structure. The first one is f.c.c. HEAs formed by the combination of 3d elements Fe, Cr, Mn, Ni and Co[7, 13, 14]. The second one is b.c.c. HEAs formed by refractory metals such as Nb, Mo, Ta, W, Ti and V[15, 16]. The last one, which was developed recently, is h.c.p. HEAs formed by rare earth and transition metals[17]. Other HEAs usually exhibit co-existence of two or even more phases, such as $Al_xCoNiCrFeCu$[18], where the phase composition is dependent upon the Al concentration (x represents the concentration). The failure to find many other HEAs by simply mixing numerous different metallic elements suggests that the formation of HEA is not solely dictated by the configurational entropy[9, 10, 12].

Key phenomena of HEAs were summarized in Zhang and Yeh's review paper[19, 20], and include high entropy, sluggish diffusion, lattice distortion and cocktail effects. While the cocktail effect basically refers to the overall effect from the unique microstructure and composition, the other three effects are still under research. High entropy is supposed to suppress the formation of complex phases and intermetallic compounds particularly at elevated temperatures due to the predominant contribution of entropy (vs. enthalpy) to the Gibbs free energy. However, as noted above, mixing entropy and conventional empirical rules of physical metallurgy are not sufficient to explain why only limited element compositions of HEAs can form single-phase solid solutions.

Sluggish diffusion is discussed in detail in Tsai's paper[21] where it is claimed that slower atomic mobility occurs in HEA compared to conventional alloys. Unfortunately, other than Tsai's work, other research studies on atomic mobility of HEA do not provide further direct evidence of sluggish diffusion. Chang[22] reported that an (AlCrTaTiZr)N thin film was an effective diffusion barrier for Cu interconnects at high temperature. The composition of the thin film obeyed the definition of HEA, but the microstructure was a complex mix of crystalline and amorphous phase. Tsai[23] also reported that an AlMoNbSiTaTiVZr HEA was a diffusion barrier, but the so-called HEA was actually amorphous under X-ray diffraction (XRD), providing no supporting evidence for sluggish diffusion effects of HEA.

Lattice distortion effect refers to the severe lattice distortion resulting from the atomic size differences between nearest neighbors. Observation of lattice distortion in HEAs has been made by XRD on pure Ni, CoNi, CoFeNi, CoCrFeNi and CoCrFeMnNi and the result is shown on Figure 1.2[24]. All diffraction patterns showed characteristic f.c.c. diffraction peaks, and their peak intensities decreased as the number of constituents increased, suggesting the enhanced diffuse scattering caused by lattice distortion. Lattice distortion was also observed in an equimolar Zr-Nb-Hf alloy in an X-ray and neutron scattering study[25].

While the existence of lattice distortion is clear, its effect on the microstructure and material property is still being examined. One approach is to correlate the degree of lattice distortion with stacking fault energy (SFE)[24]. SFEs of Ni, CoNi, CoFeNi, CoCrFeNi and CoCrFeMnNi were measured by XRD, and it was shown that SFE decreases with the increasing number of elements. Similarly, Zaddach used ab initio methods to compute the SFEs[26] and the results suggested the same trend. The low SFE of HEA also agrees with experimental observation of its high ultimate tensile strength and yield strength, since lower stacking fault energy would inhibit cross slip of dislocations. Questions remain to be answered about the effects of lattice distortion on other material properties, such as vacancies and grain boundaries.

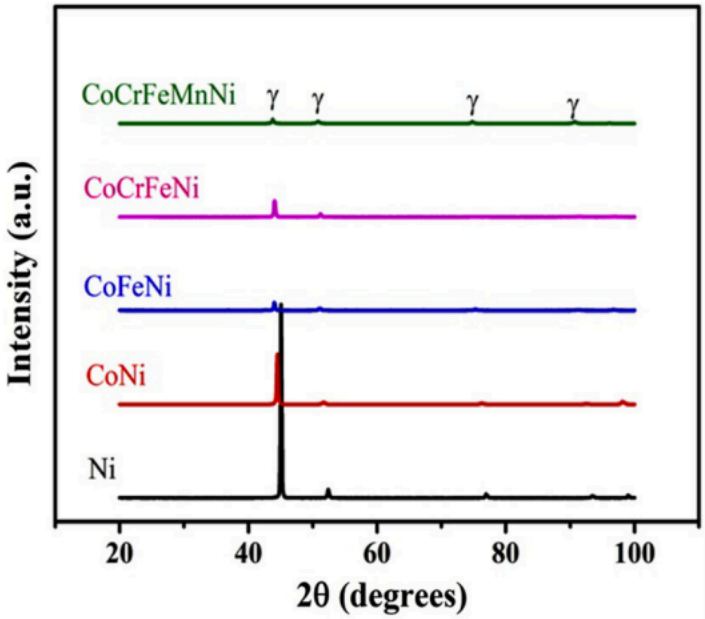

Figure 1.2 XRD patterns of the Co-Cr-Fe-Mn-Ni system from pure Ni metal to five- component alloy, as reproduced from Ref [24].

1.3 Current understanding of radiation effects in HEA

Though only one low dose neutron irradiation near room temperature has been performed to date on HEAs, several ion and electron irradiation experiments provide some useful guidance regarding radiation effects in HEA. On the modeling side, ab initio methods and molecular dynamics (MD) have provided some preliminary results on the bulk and defect properties of HEAs. Several hypotheses on radiation effects in HEA have been postulated based on these experimental observations and modeling data.

Egami[27-29] speculated that HEAs might have better irradiation resistance due to larger atomic size differences than conventional alloys. Electron irradiation experiments up to 40 displacements per atom (dpa) were conducted on Zr-Hf-Nb at -170 to 25 ˚C, and up to 60 dpa for CoCrCuFeNi at 25 to 500 ˚C HEA. No evidence of phase change nor radiation-induced amorphization were observed. However, radiation resistance encompasses much more than resistance to phase change. Amorphization is known as a problem for intermetallics and ceramics at low temperature[30]. For metals and alloys, resistance to radiation hardening, solute segregation, void and bubble swelling are more crucial phenomena because these degradation processes take place within the operating temperature window of current and advanced nuclear power reactors[2, 31, 32]. Microstructure examination needs to be more thorough to characterize the morphology

and evolution of defects at different temperatures and obtain a comprehensive understanding of irradiation resistance.

Some other studies have focused on the evolution of displacement cascades in HEAs[33]. In a displacement cascade, the number of surviving defects in the cascade may be related with the efficiency of heat dissipation from the localized "melt" region throughout the material. It is hypothesized that since HEAs have much higher chemical disorder than conventional alloys, heat dissipation in HEAs would be much less efficient. This would slow down the energy dissipation from the "melt" core and increase the duration of the thermal spike phase (where displaced atoms have relatively high kinetic energy and thereby high mobility) in the vicinity of this "melt" region. Thus, vacancy-interstitial recombination will be enhanced, resulting in smaller number of surviving defects before long-range diffusion. Experiments and electronic structure calculations have been performed to prove that HEAs have a lower thermal conductivity[33]. For the samples used in this experiment, high quality single crystals of Ni, NiCo, NiFe and NiCoFeCr were synthesized to solely focus on the effect of solid solution phase and eliminate effects from grain boundaries and precipitates.

In metals, heat is conducted through electronic and phonon scattering. The electronic part of heat conduction was calculated from the electrical resistivity by Wiedemann-Franz law. Electrical resistivity was measured from 5K to room temperature, and the electronic thermal conductivity decreased with increasing number of elements, as shown in Figure 1.3. Coherent potential approximation (CPA) method, which is an effective ab initio method to evaluate the configuration averaged properties of a disordered system, was also utilized to compute the Bloch spectral function (BSF) and density of state (DOS). Note that BSF is a generalized band structure to include the disordering effect of HEAs. From the simulation, BSFs of pure metals exhibited distinct band structures as expected. On the other hand, BSFs of NiCo and NiFe shows some smearing in minority electronic states, and BSFs of NiCoCrFe showed smearing not only in minority states, but majority ones as well. Since smearing of bands results in shorter electron mean free path, the simulation results indicate the electronic heat transfer is less efficient with the increased number of elements, in agreement with the decreasing trend with increasing number of elements for electronic thermal conductivity observed in Figure 1.3.

On the other hand, the phonon contribution to the thermal conductivity, or lattice thermal conductivity, is estimated by classical molecular dynamics and an empirical embedded-atom model potential. While reduced lattice thermal conductivity is observed for binary alloys, increasing the number of elements to ternary and quaternary alloys does not further decrease lattice thermal conductivity. Finally, the author reports the overall thermal conductivity for Ni, NiCo, NiFe and NiCoFeCr and highlights the significant decrease of overall thermal conductivity from Ni (88 $Wm^{-1}K^{-1}$) to NiCoFeCr (12.8 $Wm^{-1}K^{-1}$)[33].

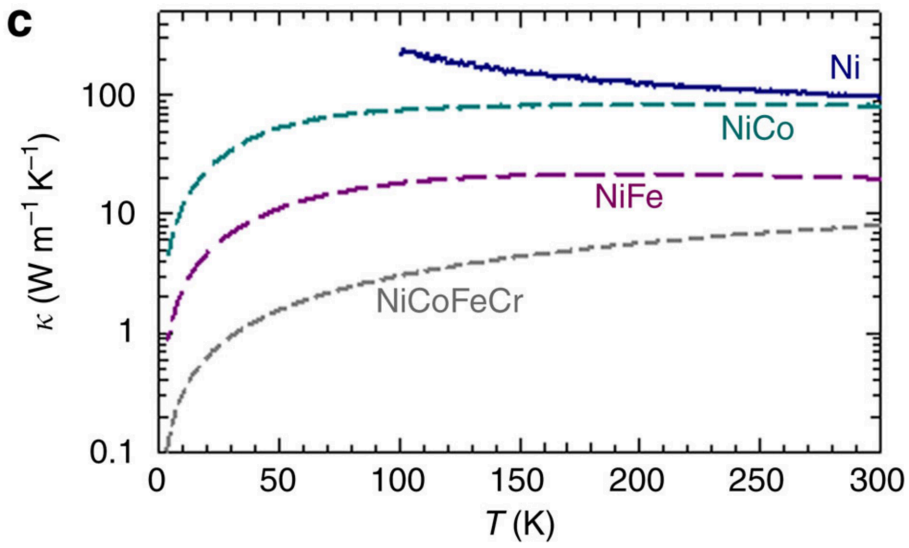

Figure 1.3 Electronic thermal conductivity of Ni, NiCo, NiFe and NiCoFeCr, as reproduced from Ref [33].

The above treatment to correlate low thermal conductivity with enhanced point defect recombination during displacement cascade, however, has several potential pitfalls. First, this treatment computes energy dissipation through electronic scattering and phonon scattering independently. By doing so, electronic-phonon coupling is not explicitly treated, which can be critically important during the energy transfer process in displacement cascade for metallic system[34-36]. One classical example is that while Cu has a higher overall thermal conductivity than Ni, the quench rate of low-energy cascades in Cu is actually slower than Ni due to the effect of electron-phonon coupling[37]. Second, in addition to chemical ordering, the effect of solutes[38-40] and magnetic scattering on electrical resistivity were not evaluated. Solute content and magnetic scattering resulting from disorder would generally increase electrical resistivity. In particular for alloys composed of 3d transition elements of large concentration, both effects can be pronounced. Finally, below ~350˚C NiFe should be a mixture of f.c.c and b.c.c phase according to the equilibrium Ni-Fe phase diagram. Presence of second phase can also contribute to electrical resistivity increase from pure metal to binary alloy system.

Ion irradiation experiments and molecular dynamics modeling have been performed by the same research team to investigate differences in radiation-induced defect production, i.e., before long-range diffusion, that could be attributed to concentrated solid solution alloy or HEA effects[33, 41, 42]. 3MeV Au ion irradiations were performed at room temperature and a relatively low fluence of $1x10^{13}/cm^2$ (~0.06 dpa peak dose) for pure Ni, and NiCo and NiFe alloys. Ion channeling technique showed higher backscattering yield of the pure metal compared to the binary alloys (Figure 1.4), indicating that the

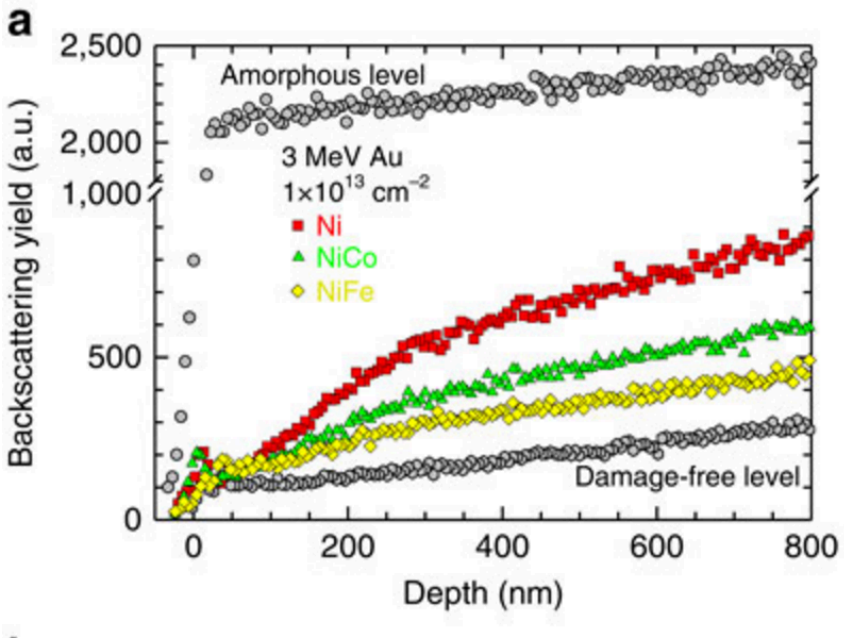

Figure 1.4 Backscattering yield of pure Ni metal, NiCo and NiFe alloys after heavy ion irradiation, as reproduced from Ref [33].

surviving irradiation damage (in the form of dislocations and defect clusters) is smaller for the two binary alloys after low dose irradiation near room temperature.

Interestingly, the most recent published channeling experiment by the same research team[43] showed an opposite effect at higher doses. In this experiment, the same Ni, NiCo and NiFe samples were irradiated by 3MeV Au ions at room temperature to $2x10^{13}$ and $5x10^{15}$ cm^{-2}, corresponding to a peak dose of 0.12 and 50 dpa. Channeling experiments were performed after irradiation and the channeling yields are plotted on Figure 1.5. At low ion fluence, both binary alloys have lower backscattering yield than pure Ni. However, at high ion fluence, both the backscattering yields of both binary alloys increase much more than the pure metal. At depths below 400nm, binary alloys basically reached the same or even higher yield than those from pure metal. This contradictory result suggests that it is still too early to definitively make the conclusion that chemical disordering would always facilitate the annihilation of radiation-induced defects. One further suggestion is that the channeling technique, which is most frequently used to probe the lattice disorder and amorphization in semiconductor, ceramics and intermetallics, may not be sufficient to accurately quantify the defect density in metals and metallic alloys and it does not provide any information regarding the nature, density or size distribution of radiation-induced defect clusters. In addition to the potential pitfalls of the RBS channeling technique, the experimental characterization in this study was only carried out on HEAs irradiated at room temperature. As a result, the HEA

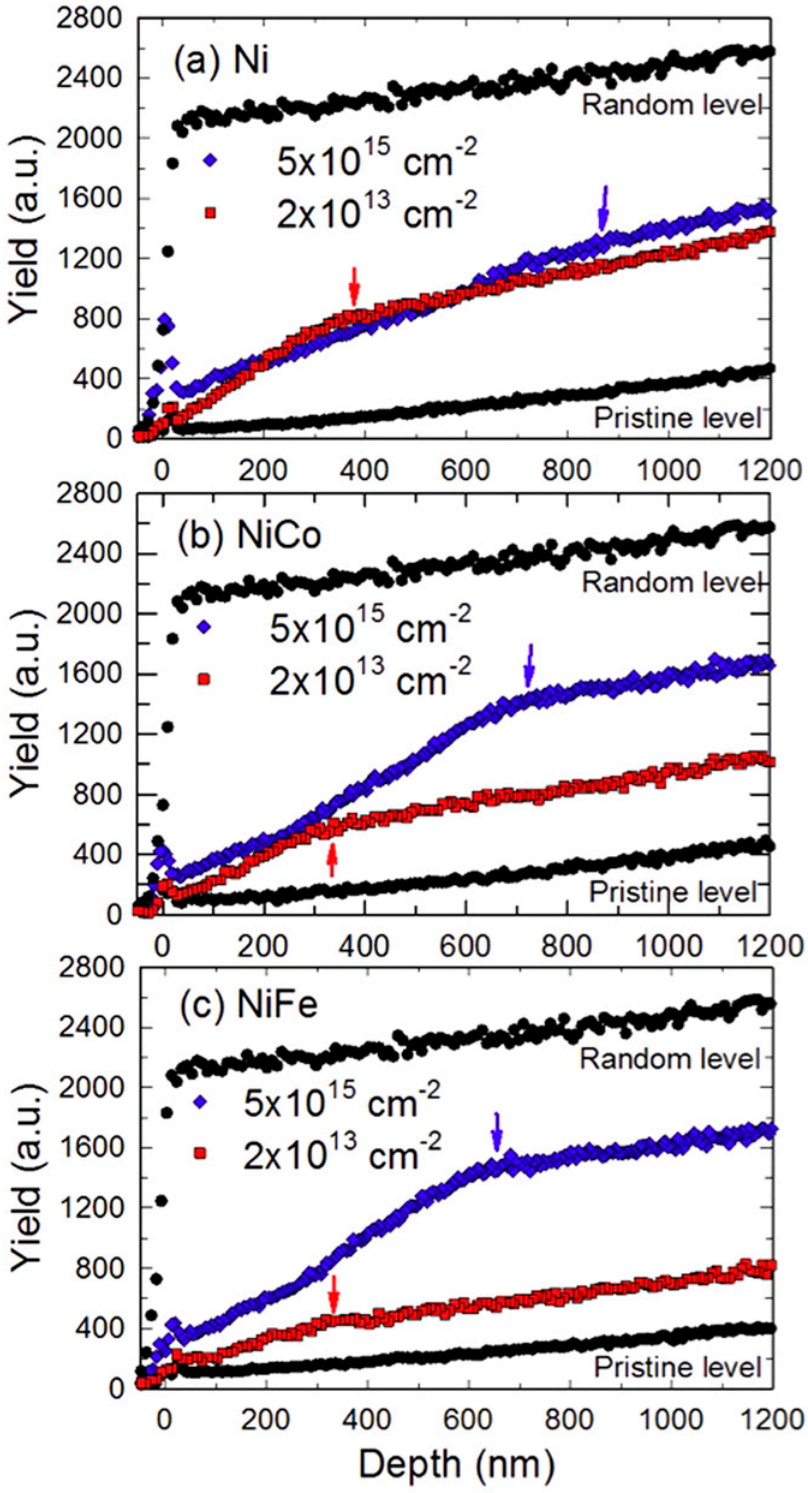

Figure 1.5 Backscattering yield of pure Ni metal, NiCo and NiFe alloys after two heavy ion irradiation of two different fluences, as reproduced from Ref [43].

resistance to degradation phenomena that occurs at intermediate and high temperature, such as swelling and elemental solute segregation, is still unknown. These degradation phenomena are generally more critical for actual engineering applications because they occur at the reactor operating temperature.

Some very recent irradiation experiments have started to explore radiation effects at higher temperature. Jin[44], Lu[45], Kumar[46] and Yang[47] have characterized void swelling after heavy ion irradiation at elevated temperature. Jin performed 3 MeV Ni ion irradiation up a peak dose of about 53 dpa at 500 ˚C for pure Ni, binary NiCo, ternary NiCoCr and the five-component NiCoCrMnFe HEA. Utilizing the step height profile, the authors showed that all the binary, ternary and multicomponent alloys exhibited much less swelling than pure Ni. Swelling calculated from TEM microscopy also agreed with the results from step height profile. The author also highlighted the exceptional performance of NiCoFeCrMn, which showed 40 times less swelling than pure nickel. Lu performed 1.5 and 3 MeV Ni ion irradiation at 500 ˚C for Ni, NiCo, NiFe, NiCoFeCr and NiCoFeCrMn. Transmission electron microscopy (TEM) showed that as the number of elements increased in the alloy, the amount of void swelling decreased, although there were important differences depending on the particular solute; for example, NiFe exhibited superior void swelling resistance compared to NiCo (Figure 1.5). Note that for comparison of radiation effects between alloys of different melting temperature, homologous temperature can be more important absolute temperature since defect thermodynamics and kinetics is generally related with homologous temperature[48]. Yang performed 3 MeV Au ion irradiation from 250 to 650 ˚C on $Al_{0.1}$CoCrFeNi and found no voids within the detection limit of TEM. Kumar performed 5.8 MeV Ni ion irradiation from 400 to 700 ˚C up to 10 dpa and also found no voids within TEM detect limits. It is worth noting that while all three of these studies showed suppressed void swelling for HEA, TEM is a more reliable technique than step height profile to detect void and quantify the extent of void swelling. Since step height profile characterizes the "collective" volume change over the whole irradiated sample, this technique cannot exclude low-swelling artifacts from the near-surface region (due to strong surface sink effects) and the ion implanted region with enhanced point defect recombination (low void swelling) due to implanted ion and compressive stresses due to the continuity with the unirradiated underlying substrate. On the other hand, cross-section TEM observations such as that shown in Fig. 1.6 can limit these artifacts of ion irradiation by strictly characterizing the microstructure at "mid-range dose" regions. For large dose, high temperature ion irradiation experiment, implanted ion effects will become more severe due to larger and wider implanted ion distribution, and enhanced self-interstitial diffusion. Thus, larger ion energy is usually desirable at these irradiation conditions.

In addition to void swelling, Lu[49], Yang[47], Kumar[46] and He[50] characterized elemental segregation at defect clusters. While He conducted electron irradiation at 400 ˚C for CrFeCoNi, CrFeCoNiMn and CrFeCoNiPd, both Yang and Lu conducted heavy ion irradiation at elevated temperature. Lu performed Ni ion irradiation at 500 ˚C for NiFe,

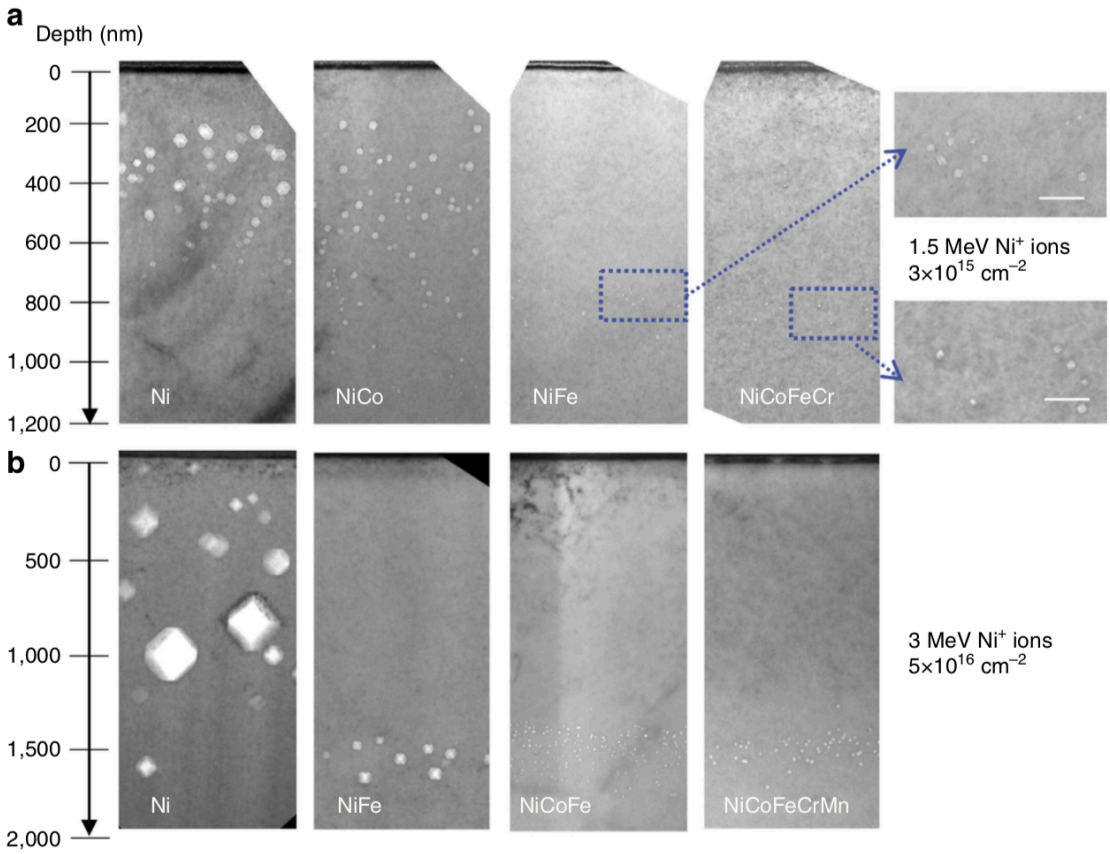

Figure 1.6 TEM micrographs showing the magnitude of void swelling in Ni, NiFe, NiCoFe, NiCoFeCr and NiCoFeCrMn, as reproduced from Ref [45]. As the number of elements in the alloy increases, the magnitude of void swelling decreases.

NiCoFe, NiCoFeCr and NiCoFeCrMn. Yang performed Au ion irradiation at 250 to 650 ˚C on $Al_{0.1}$CoCrFeNi. On one hand, all the above experimental characterizations find Cr depletion and Ni enrichment at defect clusters, which agrees with the Cr and Ni solute segregation behavior in conventional austenitic stainless steel. On the other hand, the experimental results of Lu revealed that as the number of elements in the HEA increases, the magnitude of elemental segregation decreases, suggesting superior resistance of HEA to elemental segregation. For NiFeMnCr HEA, Kumar's study found Cr depletion and Ni enrichment at grain boundaries. Their segregation profiles with respect to temperature show a "bell-shaped" curve, where the magnitude of segregation peaks at intermediate temperature. Both observations are consistent with Fe-Ni-Cr austenitic alloys. However, the scale of segregation is lower for both Cr and Ni in NiFeMnCr HEA than conventional alloys at similar irradiation conditions. Finally, TEM characterization in Lu's work also shows a higher fraction of faulted loops in the more compositionally complex alloys, suggesting suppressed loop growth in HEA. This is inconsistent with experimental

observations from a 400 ˚C electron irradiation study[51], where CrNiFeCo's loop growth rate was >40 times smaller than pure Ni, and also consistent with Kumar's comparison of defect cluster size and density between NiFeMnCr HEA and conventional Fe-Ni-Cr austenitic alloys at similar irradiation conditions.

These experimental observations of suppressed void swelling, elemental segregation and loop growth are consistent with sluggish diffusion effect in HEA. Some preliminary modeling studies also provide evidence to support this claim of "sluggish diffusion". Ab initio molecular dynamics (AIMD) modeled interstitial diffusion in NiFe, NiCo and NiCoCr[52]. Simulation results showed that interstitial diffusion is slower in binary and ternary alloys than pure Ni. In addition to suppression of interstitial dumbbell diffusion, diffusion of large interstitial clusters may also be suppressed. Gao simulated the migration of large interstitial clusters in NiCo and NiFe[45] through MD. Results showed that 1D diffusion of large defect clusters, which is commonly seen in pure metal, is largely suppressed in NiFe. As well, the MD study by Granberg[53] found reduced mobility of dislocations in NiFe and FeCoCr compared with pure Ni. This finding is also consistent with sluggish diffusion of point defect and defect clusters. While these modeling studies facilitate the understanding of experimental results, the potential pitfalls in the modeling methods need to be considered. First, due the limitation of current computational power, AIMD simulation is restricted within a small supercell and thus it is not the most suitable method to model the long range mass transport process. Second, current semi-empirical potentials for multi-component concentrated alloys may not be able to compute reasonably accurate defect properties. Zhao[54] computed defect formation energies of two binary alloys based on *ab initio* methods and three semi-empirical potentials. Interstitial dumbbell formation energies computed from these two methods are plotted in Figure 1.7. The comparison shows that empirical potentials generally over-predict interstitial dumbbell formation energies. Besides, while *ab initio* method shows that dumbbell formation energies in $Ni_{80}Fe_{20}$ are always larger than those in NiFe, Bonny 2011 and Bonny 2013 potential predicts that the formation energies for these two alloys are basically the same. Since the reliability of MD results critically rely on the accuracy of semi-empirical potential, interpretation of MD results of the above binary alloys need to be evaluated with great care.

Overall, the research on radiation effects of high entropy alloy is still at a nascent stage. While a number of ion and electron irradiation studies have shown that HEAs have superior resistance to void swelling and elemental segregation, more detailed experimental work is needed to understand the temperature and dose dependence of these important degradation phenomena. Besides, although ion and electron irradiation can reproduce certain fundamental radiation effects in HEAs, structural materials are ultimately irradiated by neutrons in nuclear reactors. Thus, neutron irradiation effects are more critical for engineering application. However, due to neutron activation induced by large Co content, almost all of the HEAs studied in the above ion and electron irradiation are not desirable for neutron irradiation tests. A reduced-activation version of HEA, such as the Co-free HEA studied by Wu[55] and Kumar[46], needs to be designed to more

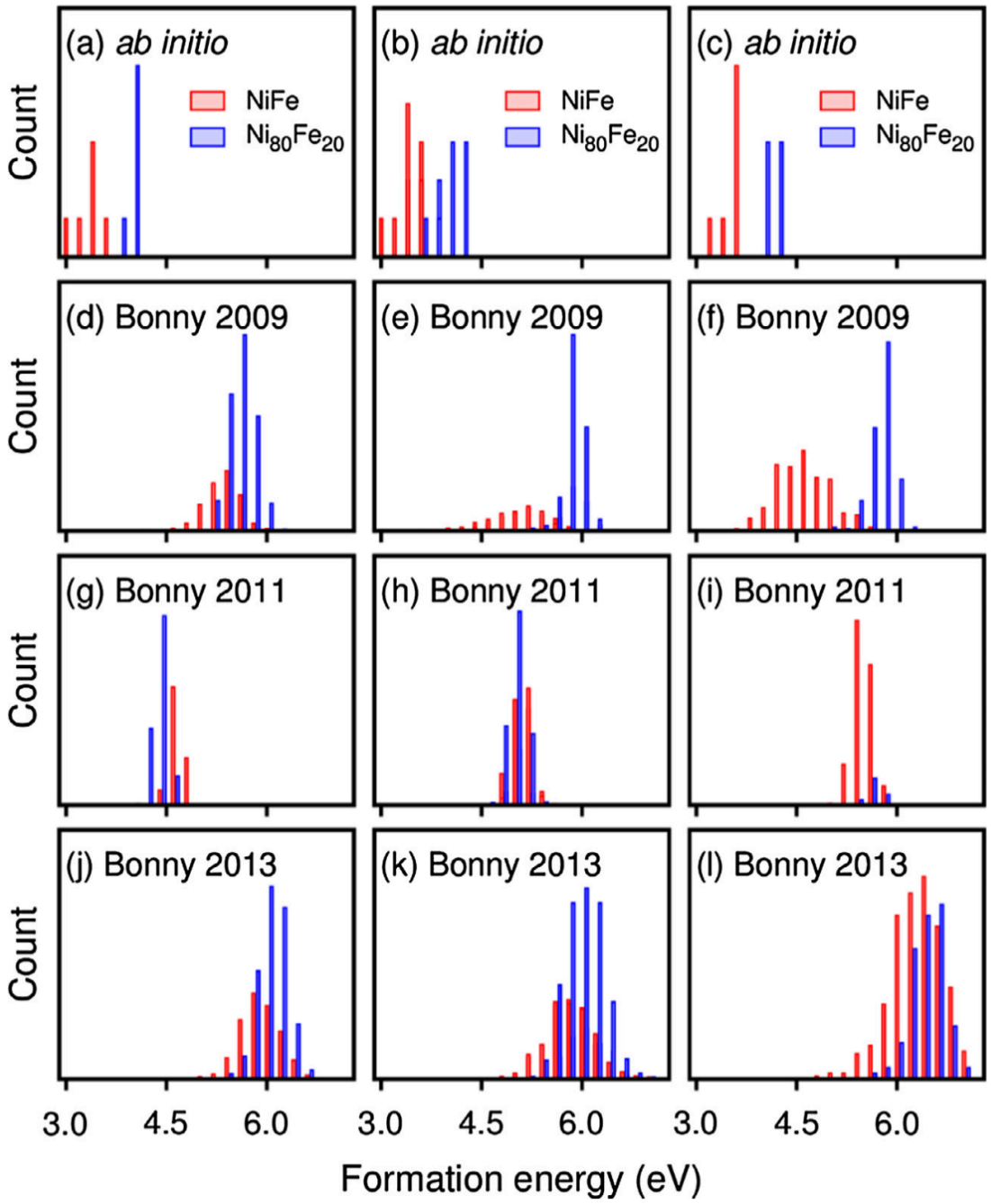

Figure 1.7 Cross comparison of interstitial dumbbell formation energy (left column: Ni-Ni, middle column: Ni-Fe, right column: Fe-Fe) based on ab initio method and three different semi-empirical potentials, as reproduced from Ref [56]. Note that the statistical distribution from MD can be very different from ab initio calculation for certain EAM potentials, such as Bonny 2009.

economically investigate neutron irradiation effects. On the modeling side, while binary and ternary concentrated alloys have been studied, four-component alloys have not yet been explored. Further, for all these concentrated alloy systems, more detailed fundamental modeling work is needed to correctly identify the unique physics in HEAs and build a solid foundation for higher level modeling techniques, such as MD.

1.4 Integrated approach to evaluate radiation effects in a Co-free HEA

As mentioned in the previous section, many of the single-phase high entropy alloys have Co, which is not desirable for nuclear energy application due to high-induced radioactivity. Thus, a novel 27%Fe-27%Mn-28%Ni-18%Cr (in wt%) high entropy alloy has been synthesized[55] for this study. Preliminary mechanical testing shows that it is a promising model alloy for engineering applications because it exhibits good strength and ductility over a wide range of temperatures (Figure 1.8). The ingot was prepared by arc-melting and dry-casting. To approach thermodynamic equilibrium, the ingot bar was homogenized at 1200 ˚C for 24 hrs and then quenched into cold water. After that, the ingot was cold rolled and cut into pieces as specified by experiment requirement. Finally, these sample pieces were annealed at 900 ˚C for 4 hrs at vacuum to reach a fully recrystallized microstructure with grain size ~ 35 microns.

Since the radiation effects of this model HEA has not been studied, an integrated research approach has been proposed to investigate radiation effects in accordance with Ref [[57]]. As is shown in Figure 1.9, this integrated approach of combining multi-scale modeling and comprehensive experimental characterization has been applied to understand radiation effects in pure metal and dilute alloys in the past two decades. On one hand, for modeling, the information flow between different modeling techniques can bridge the gap in time-scale and length-scale of each individual technique. Observations from different experimental techniques can investigate the same phenomena from different angles and provide increased confidence regarding basic radiation effects. For example, both TEM and positron annihilation technique can characterize vacancy clusters. While TEM can detect large vacancy clusters above nm scale, positron is sensitive to small clusters formed by several to tens of vacancies. Combining these two techniques can thus provide a full picture of void size and density inside the irradiated material. On the other hand, experimental and modeling studies can facilitate each other. Experimental data is crucial for validating models, and the models can in turn help design experiments.

While this integrated approach has been developed for a long time, past knowledge and experience may not be applied for HEAs due to their unique physics. Thus, for the modeling part, the research detailed in this thesis focuses on ab initio electronic structure calculations to establish a solid foundation for the multi-scale modeling of NiFeMnCr HEA. This foundation may also be applicable for modeling other types of HEAs. In parallel, both ion and neutron irradiation experiments have been conducted. A series of

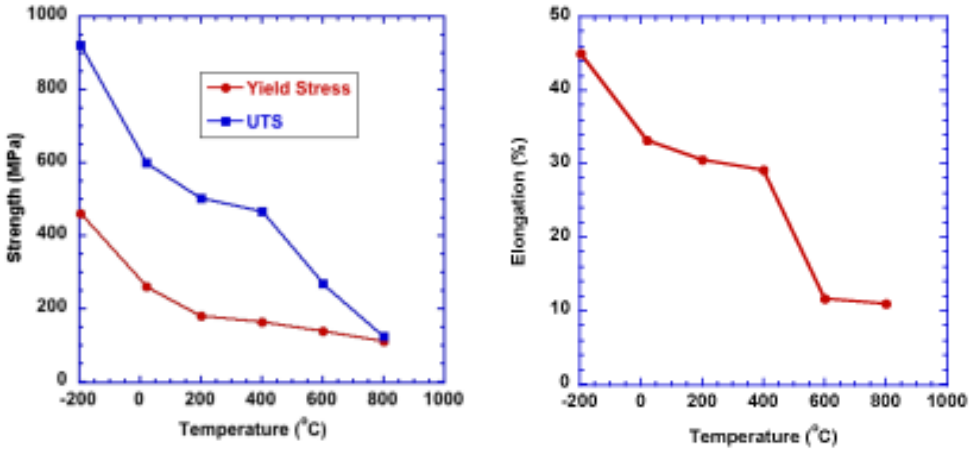

Figure 1.8 Strength and ductility of NiFeMnCr high entropy alloy at different temperatures, as reproduced from Ref [46]

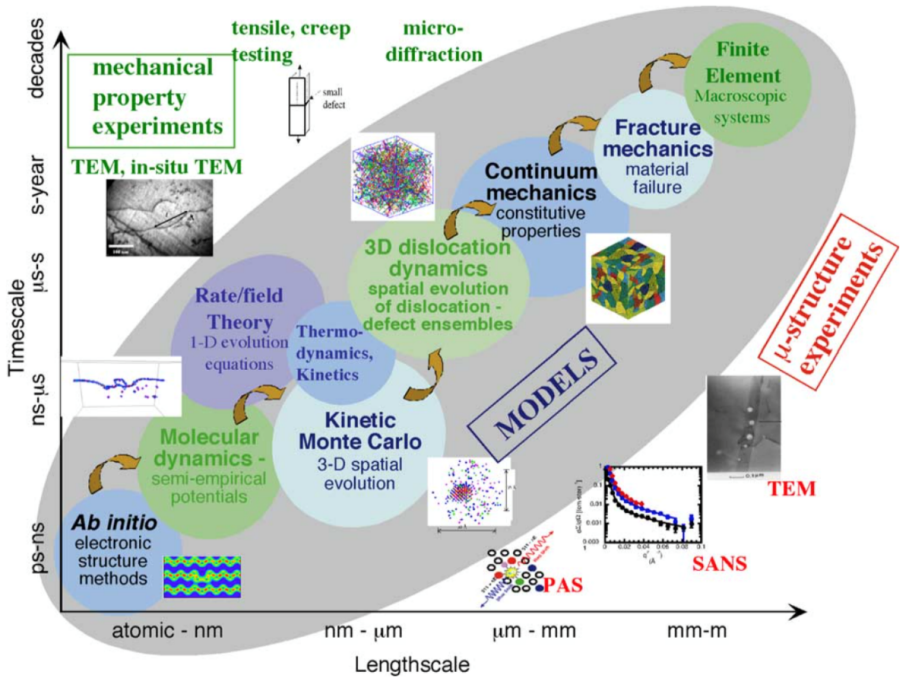

Figure 1.9 Integrated approach for studying radiation effects in materials. Modeling techniques at different time- and length-scale build up on each other through the inter-connecting information flow (yellow arrows), as reproduced from Ref [57]. Experimental characterizations reveal the microstructure stability and mechanical performance under irradiation, and also validate the theoretical model. This comprehensive approach enables understanding and prediction of properties of irradiated materials.

room temperature and high temperature ion irradiation experiments were performed to carefully examine the effects of temperature on irradiated microstructure. Low temperature, low dose neutron irradiation was conducted to test the fundamental microstructure and mechanical stability of this model HEA. For the post-irradiation examination of neutron and ion irradiated samples, a comprehensive set of experimental characterization techniques, such as TEM, nano-indentation, X-ray Diffraction, were performed to investigate HEA's radiation effects from different perspectives. The integrated understanding of experimental and modeling results from this work will provide many new insights on the radiation effects of this Co-free HEA as well as other HEAs.

CHAPTER TWO

ION IRRADIATION AND POST-IRRADIATION EXAMINATION

2.1 Introduction

Heavy ion irradiations were conducted by a linear accelerator to study radiation effects in a NiFeMnCr high entropy alloy at room versus elevated temperature. Compared with neutron irradiation in a test reactor, ion irradiation provides faster damage rate and zero induced radioactivity. Thus, this technique largely shortens the time of irradiation experiments and reduces radiation contamination hazards from sample transfer and handling. As mentioned in Chapter 1, advanced nuclear power reactors require materials to operate at much higher dose of radiation damage. The high damage rates achievable with ion irradiation makes it convenient for researchers to explore material performance and microstructure stability at ~100 dpa dose level, and thus provide an efficient pathway to validate structural materials for engineering application in advanced reactor technology[58, 59].

However, to correctly utilize the merits of ion irradiation, one also needs to recognize the limitations and potential pitfalls of ion irradiations. While neutron irradiation produces a uniform damage profile due to uniform displacement cross section with respect to particle penetrating depth, the depth-dependent damage profile for ion irradiation is determined by ion type and energy, and has a typical penetrating depth from several to tens of microns (Figure 2.1)[30]. Thus, conventional bulk test methods, such as electrical resistivity, tensile test, creep and fracture toughness, are not applicable for ion-irradiated samples. While microstructure change is depth independent for neutron irradiation, microstructure changes can be strongly depth-dependent for ion irradiation. One needs to carefully choose the depth for analyzing the irradiated microstructure at a certain dose. Also, this depth should not be close to surface sink region or regions with high concentration of implanted ions (near the peak dose region)[60, 61] because these regions introduce artifacts that are not present in bulk material irradiated by neutrons in actual reactors.

In addition to the limited experimental techniques and the relatively small, micron-scale analysis volume, one needs to avoid some common pitfalls when interpreting the results from ion irradiations. First, ion beam experimental conditions are critical. Ion irradiations in modern accelerators are typically conducted by either raster beam or defocused beam techniques. Raster beams lead to very uniform fluence profiles over centimeter-scale areas, whereas defocused beams produce typical Gaussian beam profiles. However, since raster beams can lead to pulsed beam artifacts, the characterization results from the two beam techniques at the same ion fluence and exposure temperature can be very

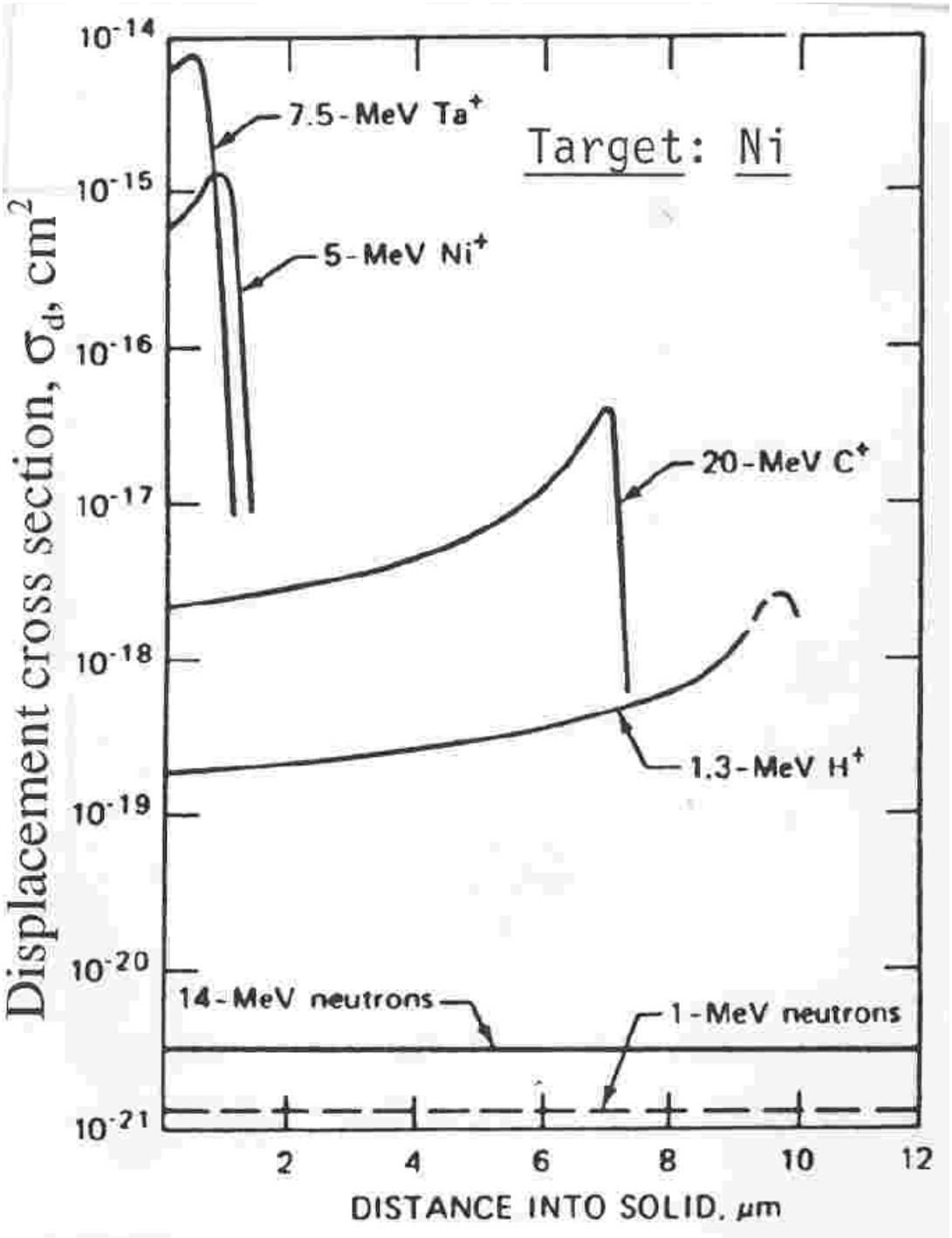

Figure 2.1 Comparison of displacement cross section between neutrons and ions of different energy and of different type, as reproduced from Ref [30].

different[30]. The steady-state defocused beam is more representative of the conditions for steady state nuclear reactor operations. Second, higher dose rate is a double-edged sword. While the fast dose rate of ion irradiation facilitates the exploration of radiation damage at large dose, the results cannot be directly used to simulate neutron irradiation at the same dose and temperature due to the difference in dose rate. While some studies tried to utilize a temperature shift model[62] to make closer connection between neutron and ion-irradiated microstructure at the same dose, just changing temperature does not reconcile all the different features in microstructure. Figure 2.2 shows the void microstructure of Ni irradiated by neutrons and Ni self-ion[63]. In this experiment, the temperature shift model takes into account the change in peak swelling temperature caused by 3000 times difference in dose rate. However, the resulting void microstructure is still different, where neutron irradiated sample has smaller voids at higher density for the same overall void swelling value.

In summary, ion irradiation is a useful and efficient tool to investigate fundamental radiation effects, such as void swelling, elemental segregation, phase stability, at various temperature and dose conditions. However, careful consideration needs to be given to its drawbacks such as limited volume for sample analysis and dose rate effects, along with near surface denuded zone and possible peak void swelling effects as well as implanted ion artifacts (suppressed void swelling and reduced precipitation) near the peak damage region. Implanted ion artifact can cause suppressed swelling. The distribution of the implanted ion is sensitive to ion energy, damage dose and irradiation temperature, and

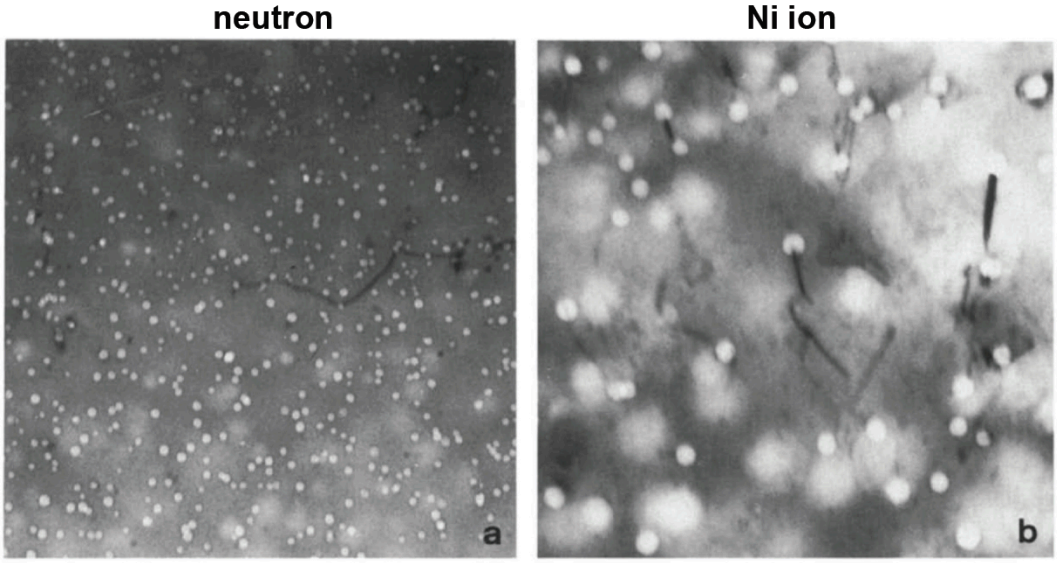

Figure 2.2 Comparison of void microstructure between neutron and ion irradiated Ni under TEM, as reproduced from Ref [63].

Ref [61] provide a general recommendation to estimate the implanted ion distribution and avoid this artifacts. There is still a long way to go to simulate neutron irradiation phenomena in actual nuclear reactor by ion irradiation. Both ion and neutron irradiations are valuable to both understand fundamental radiation effects in this novel NiFeMnCr HEA and examine its feasibility for structural applications in advanced fission and fusion reactors.

2.2 Ion Irradiation and Experimental Methods

Radiation damage was estimated by the SRIM software[64], which is a widely used software in the ion-material interaction community to calculate ion range and damage profile. Defocused beam, instead of raster beam, was used for the ion irradiation to eliminate the artificial annealing effects from raster beam[65, 66]. 3 and 5.8 MeV Ni ion irradiations were performed at the conditions listed in the Table 2.1. Note that the listed dose values in Table 2.1 are all midrange doses. Ion irradiation doses were computed by SRIM following the recommendations of Stoller[64] (40 eV displacement energy, quick Kinchin-Pease option), and the SRIM computation results are shown in Figure 2.3. All the microstructure characterization was performed at the midrange-dose region to avoid the surface sink effect and injected self-interstitial effect[60]. The 3 MeV irradiation was performed at the Ion Beam Material Lab (IBML) at the University of Tennessee, Knoxville, while the 5.8 MeV Ni irradiation was performed at Texas A&M University.

A comprehensive set of experimental facilities was used for post irradiation characterization. A conventional X-ray diffraction (XRD) instrument was used to investigate phase stability. Grazing incident XRD was conducted by a PANanalytical Xpert Diffractometer with the incident beam fixed at 2˚ to the sample surface, which gives a maximum penetration depth of 2 micron. Nano-indentation was used to probe the hardness change in the near surface region, using an MTS XP nano-indentation system equipped with a Berkovich indentor. Philips CM200 FEG (field emission gun) Transmission electron microscope (TEM)/scanning transmission electron microscope (STEM) was used to examine the microstructure to determine the presence, size and density of second phase particles, voids and defect clusters. To examine radiation induced solute segregation (RIS), a Talos F200X STEM equipped with a super-X EDS system was used to reach finer resolution (<1% local chemistry change). Cross-section TEM specimens from the irradiated samples were prepared using a focus ion beam (FIB). Low voltage argon ion polishing was used to remove the near-surface damage caused by FIB milling.

Table 2.1 Summary of ion irradiation conditions for the high entropy alloy. The listed damage doses are computed at midrange region, which is at ~0.5 for 3MeV Ni ion irradiation, and ~1.0 for 5.8MeV Ni ion irradiation.

3 MeV Ni ions	5.8 MeV Ni ions
0.03 dpa at Room temp.	10 dpa at 400 °C
0.3 dpa at Room temp.	10 dpa at 500°C
0.3 dpa at 500°C	10 dpa at 600°C
3 dpa at 500°C	10 dpa at 700°C

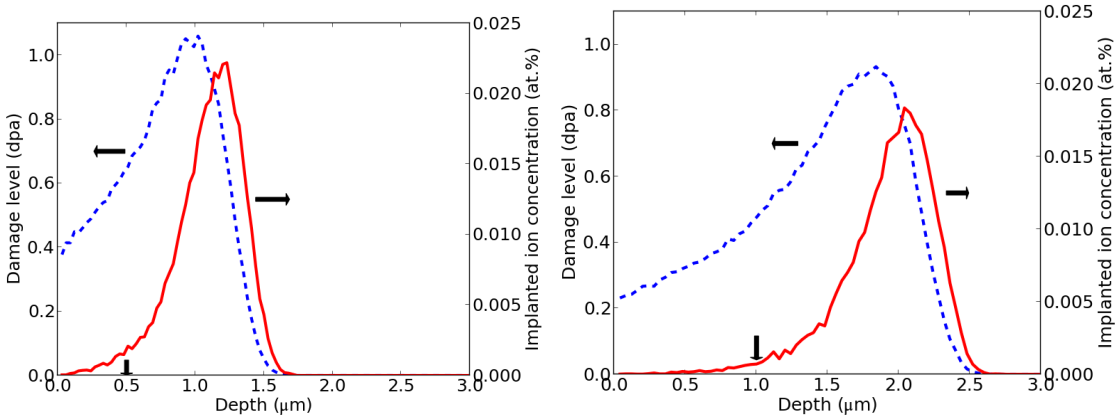

Figure 2.3 SRIM plots showing the calculated damage profiles of 3 MeV (left) and 5.8 MeV (right) Ni ions in 27%Fe-28%Ni-27%Mn-18%Cr. Y-axis represents the damage and implanted ion concentration per 10^{15} ions/cm^2. The arrows at X-axis indicate where the midrange dose is evaluated.

2.3 Phase change characterization from X-ray diffraction (XRD) and electron diffraction

XRD is an efficient tool to examine phase stability and lattice distortion in materials. The phase volume defection limit of the instrument used for this study is 3 wt%. For the un-irradiated control sample, the diffraction pattern showed pure f.c.c phase with no second phase present. XRD was also performed on four samples irradiated by 3MeV Ni ions as shown in Figure 2.4. For all the irradiation conditions, only peaks corresponding to f.c.c phase were observed; no second phase is detected. The moderate change in peak intensity between the different samples is probably caused by moderate texture of the sample.

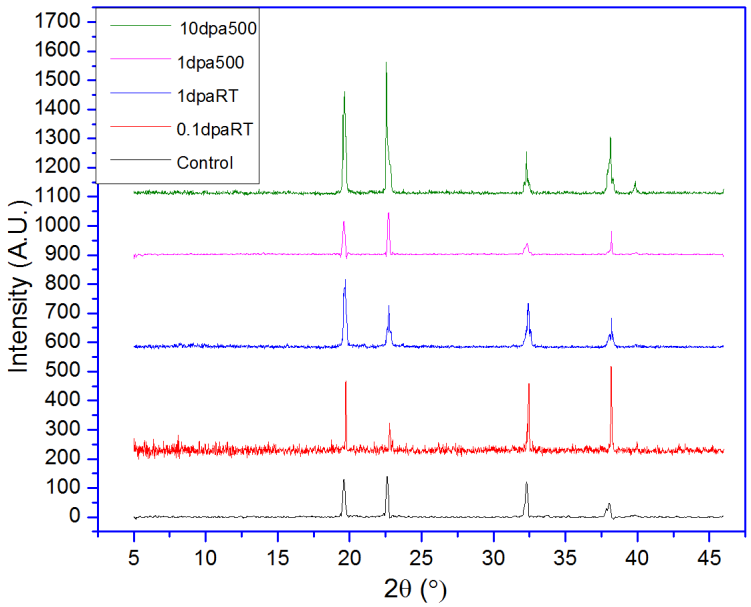

Figure 2.4 XRD patterns of the HEAs under different conditions.

Electron scattering technique was utilized to survey any local, fine-scale second phase particle that cannot be detected by XRD. In the control sample, only a few precipitates were found during scanning electron microscope (SEM) analysis and they were confirmed to be Cr- and Mn-rich oxides by electron dispersive spectroscopy (EDS). Similarly, only a few scattered Cr- and Mn-rich oxides were observed under transmission electron microscopy (TEM) and EDS for all irradiated samples.

In summary, X-ray and electron scattering techniques show that the f.c.c phase was stable upon ion irradiation up to 10 dpa from room temperature to 700 ˚C.

2.4 Void, Dislocation and Radiation Induced Segregation characterized by electron diffraction

Void swelling is a commonly seen degradation phenomenon in irradiated alloys at intermediate temperature. The combination of over- and under-focused mode in TEM is one of the best techniques to examine the formation of voids. In conventional Fe-Cr-Ni alloys, voids are generally detected above 1-10dpa between 450 and 600 ˚C. On the other hand, for this novel NiFeMnCr HEA, no voids were observed up to 10 dpa at 400 – 700 ˚C (Figure 2.5).

Weak beam dark field imaging technique was used to quantify the number density of fine scale dislocation loops. To best eliminate the defect cluster artifacts formed by ion milling during the sample preparation process, volumetric density was evaluated by

calculating the slope of the areal defect cluster density vs. specimen thickness. Figure 2.6 compares the dislocation density of irradiated NiFeMnCr HEA with similar studies on conventional Fe-Cr-Ni alloys as a function of temperature[46]. At temperatures below 400 ˚C, the loop density in the HEA is on the same order of magnitude with conventional alloys. As irradiation temperature increases, enhanced defect diffusion should promote the annihilation of defects and thus decrease the defect cluster (dislocation loop) number density. This decreasing trend, however, is less significant for HEA. At 700 ˚C, the dislocation loop density in the HEA is 100 times larger than conventional alloys.

Similar to dislocation loop density, RIS is also a temperature dependent phenomenon. The segregation of solutes to defect sinks such as grain boundaries or dislocation loops is determined by the preferential coupling of certain solute species with the point defect fluxes. For typical f.c.c alloys, the segregation magnitude is largest at intermediate temperature. Low temperature decreases the diffusivity of point defects while high temperature promotes point defect recombination. Both factors decrease the point defect-coupled solute flux to the grain boundary and thus reduce segregation[30, 67, 68]. In this study, several low angle grain boundaries of the 5.8 MeV Ni ion irradiated samples were chosen for the characterization of RIS. The results show that NiFeMnCr HEA also exhibit similar trend of temperature dependence as conventional alloys (Figure 2.7). Maximum Ni, Cr and Fe segregation occurs at an intermediate temperature of 600 ˚C, and 500 ˚C for Mn. Segregation is less pronounced at higher or lower temperature. On the other hand, typical ion irradiated f.c.c Fe-Cr-Ni alloy shows maximum segregation at 300 - 500 ˚C[30, 68] .

In addition to temperature dependence, the elemental dependence of RIS was also investigated for the ion irradiated NiFeMnCr HEA. In alloys with similar sized solute atoms, substitutional diffusion via inverse Kirkendall processes are typically dominant[69]. For conventional f.c.c alloys, Cr and Mn usually deplete because they are undersized relatively fast diffusing substitutional species, while Ni usually enriches because it is the opposite. For the HEA, all three elements show the same qualitative trends, but the relative magnitude of the solute segregation is smaller than conventional alloys. Figure 2.8 shows the comparison of compositional change of Ni and Cr between HEA and SS316 ion irradiated at the same dose[70]. The segregation magnitude for both elements is both more than doubled in SS316, which is a commonly used material for nuclear structural components.

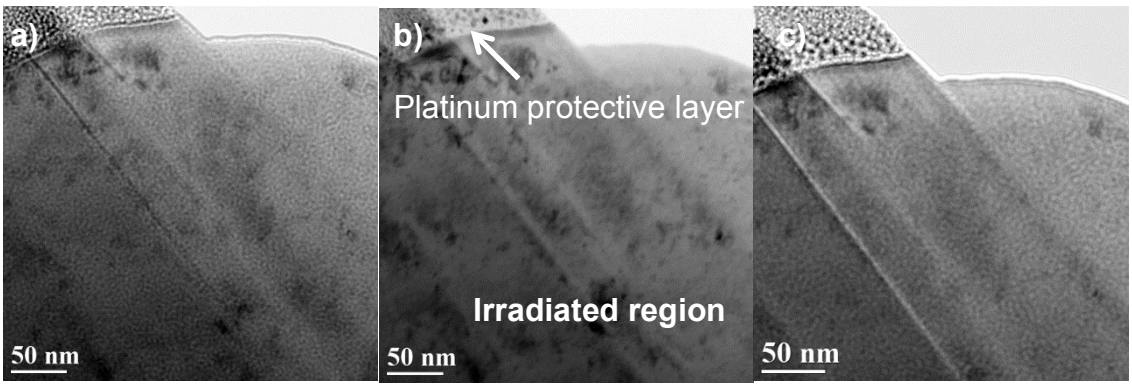

Figure 2.5 Bright field TEM image series of NiFeMnCr irradiated to 10 dpa at 700 ˚C. a) focus b) under-focus c) over-focus. The original irradiated surface is located near the top of these images.

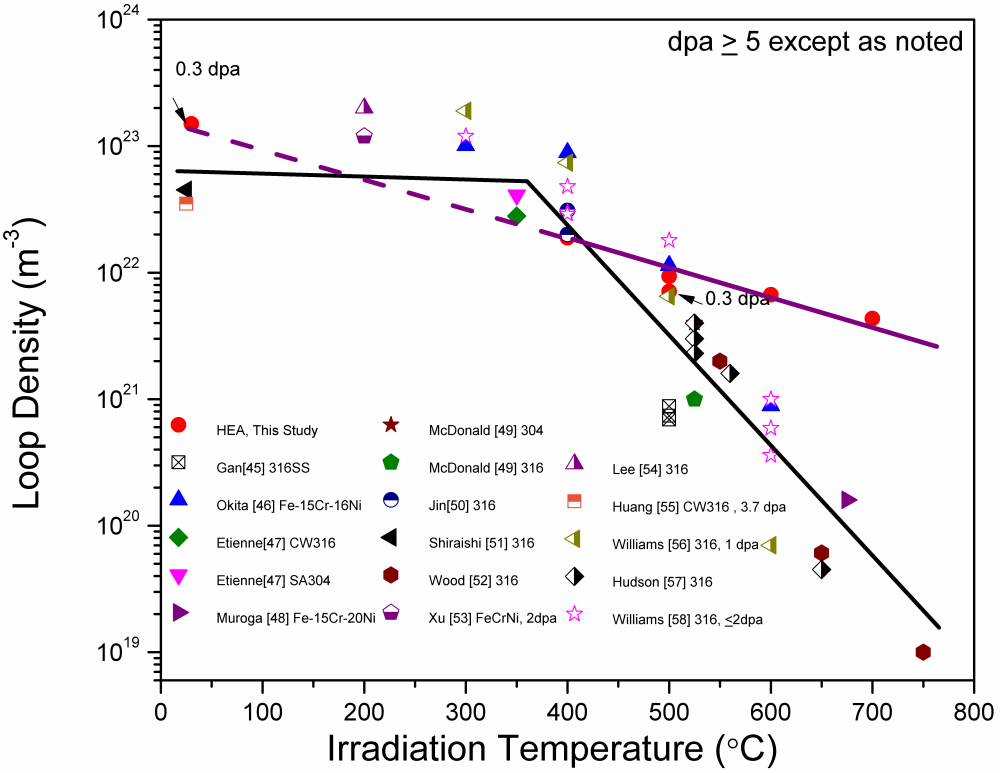

Figure 2.6 Effect of ion irradiation temperature on dislocation loop density for Fe-Ni-Mn-Cr HEA compared to conventional Fe-Cr-Ni austenitic alloys.

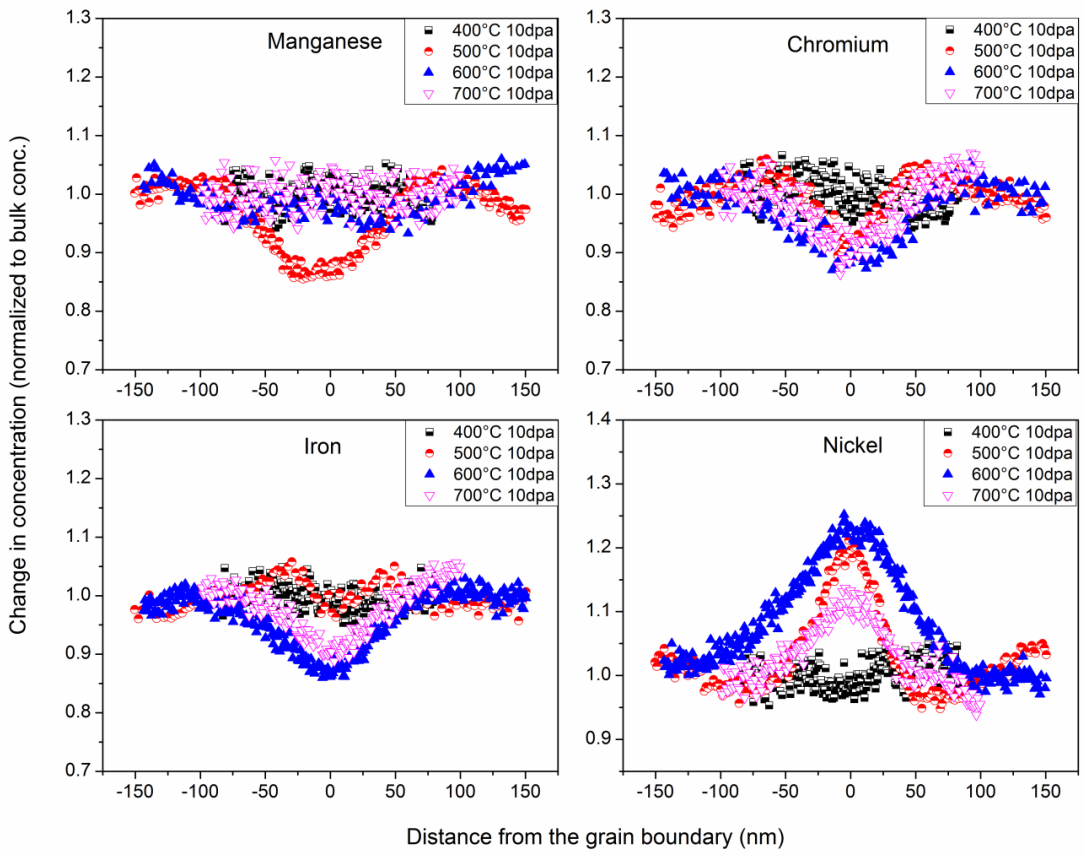

Figure 2.7 Concentration profile at grain boundary for Cr, Mn, Fe and Ni at 400 – 700 ˚C.

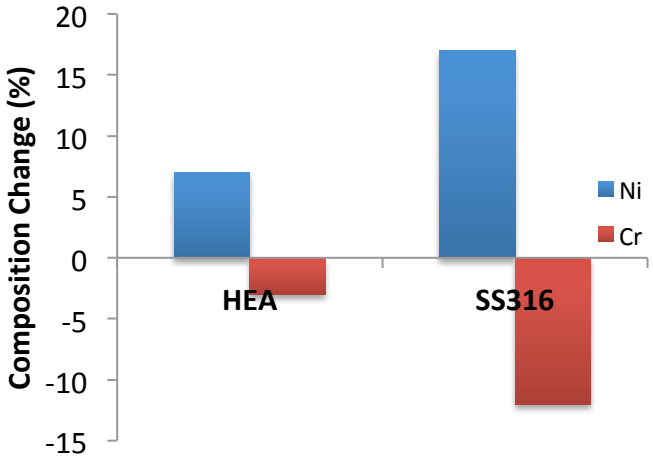

Figure 2.8 Comparison of Cr and Ni's composition change at grain boundary between the studied HEA and SS316 after heavy ion irradiation.

To summarize, TEM and analytical electron microscopy characterization has revealed three interesting results: First, under all intermediate-dose (10 dpa) irradiation conditions from 400 to 700 ˚C, no voids can be detected. In contrast, void density of 10^{20}-10^{21} m^{-3} has been found for conventional stainless steel under similar ion irradiation conditions. Second, dislocation loop microstructure after ion irradiation exhibits a less pronounced dependence upon temperature for the HEA. Finally, the HEA shows a qualitatively similar trend of segregation (Ni enrichment and Cr depletion) at the examined grain boundaries. However, the magnitude of solute segregation is much smaller, and the condition for maximum solute segregation takes place at higher temperature compared to conventional austenitic Fe-Cr-Ni or Fe-Cr-Mn alloys.

2.5 Irradiation hardening characterized by nano-indentation and electron microscopy

Since the ion irradiated region in this study is only several microns in thickness, nano-indentation is a powerful technique to investigate irradiation hardening because it is sensitive to property changes in nm scale. Due to surface contamination on the 5.8 MeV ion irradiated samples that were irradiated at the TAMU facility, nano-hardness was performed only on the control and IBML 3 MeV ion irradiated samples. For each sample, 20 indents were made and the average was taken as the final results. Figure 2.9 shows the normalized hardness of the irradiated samples with respect to the control. Before interpretation of the nano-hardness result, one important thing to note is that the plastic zone generated by the indenter can extend up to 10 times the indentation depth[71, 72], and the indenter is probing all microstructural features within the plastic zone. Thus, the "effective" ion irradiated region probed at an indenter depth of 150 to 200 nm can extend to the 1.5μm maximum irradiated depth for the 3MeV ion irradiated samples. One needs to first experimentally determine this effective depth and eliminate data generated by indents greater than this depth to avoid effects contributed by un-irradiated regions. The Nix-Gao method is a well-tested model[73] to analyze the depth-dependent hardness and can be used to determine the effective ion irradiated depth (particularly if the radiation induced hardness values do not vary significantly within the irradiated region). A representative fit for an HEA sample irradiated at 0.03 dpa, room temperature condition is shown on Figure 2.10. The red line is the fit only using data at relatively large indent depths (~350 – 1000 nm) that predominantly probe the unirradiated substrate region. The uniform slope of the Nix-Gao fit indicates uniform hardness, and thus the divergence between the raw data (blue dots) and fit (red line) is the indicator of the irradiated/un-irradiated interface sensed by the indenter. Based on this model, 350 nm is the smallest effective depth that is predominantly probing only the ion-irradiated region for all four irradiation conditions. Also, to minimize statistical errors from surface artifacts and irregularity/surface roughness, data below 200nm indent depths is not used. Thus, only the data from 200 to 350 nm is used for the following quantitative analysis.

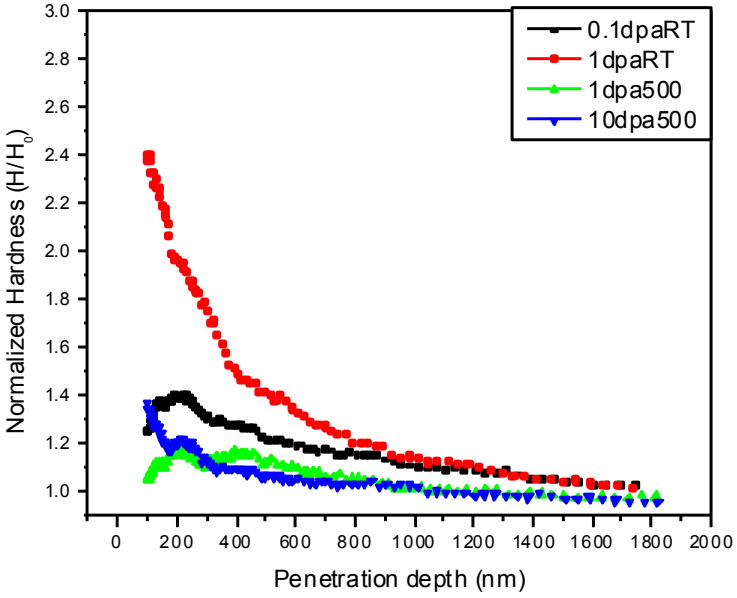

Figure 2.9 Nano-indentation hardness as a function of indentation depth for the 3MeV Ni ion irradiated samples.

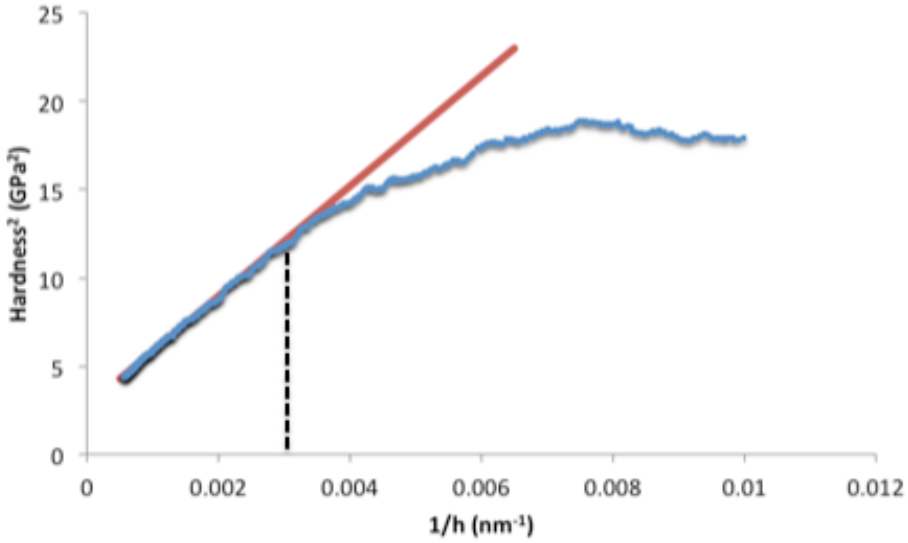

Figure 2.10 Representative Nix-Gao fit of the irradiated samples to determine the transition between irradiated and un-irradiated region sensed by the indenter tip.

Higgy and Hammed[74] and other researchers[75] have determined a linear relationship exists between change in yield strength and hardness ΔH.

$$\Delta H = K\Delta\sigma_y \quad \text{(Eq. 2.1)}$$

Therefore, the nanoindentation hardness increases summarized in Table 2.2 can be converted to an approximate increase in tensile strength. From Ref. [74, 76], K~3 for neutron-irradiated austenitic stainless steel and is used to obtain a qualitative estimate of change in yield strength for this ion-irradiated HEA. The estimated yield strength changes by ~300MPa and ~700MPa after 0.03dpa and 0.3dpa irradiation at room temperature. The estimated increase in yield strength is only ~100MPa when the irradiation temperature increases to 500 ˚C for the 0.3dpa sample.

According to radiation hardening theory developed by Orowan and Seeger[77, 78], defect clusters, such as dislocation loops, generated by radiation can act as obstacles to the glide of dislocation. The dispersed barrier-hardening model linearly relates change in yield strength $\Delta\sigma_y$ with the square root of defect cluster density N:

$$\Delta\sigma_y = M\alpha\mu b\sqrt{Nd}, \quad \text{(Eq. 2.2)}$$

where M is the Taylor factor (3.06 for equiaxed b.c.c and f.c.c metals), α is the barrier strength factor, μ is the shear modulus, b is the Burgers vector for gliding dislocations and d is the diameter of the clusters.

Based on this equation and the dislocation loop density quantified by TEM analysis in Section 2.4, it is possible to analyze the contribution of dislocation loops to radiation hardening at different irradiation condition. Table 2.2 shows the comparison of the experimental and calculated change in hardness. First, as expected, the low temperature higher dose sample shows the largest change in hardness. Second, the hardening increase after 0.3 dpa irradiation is reduced by ~7x for an irradiation temperature of 500 ˚C compared to room temperature. The calculated change in hardness generally agrees with experimental findings, suggesting that dislocation loops are the major contributor to the hardening of NiFeMnCr HEA.

Table 2.2 Comparison of nano-hardness results with calculated change of hardness based on measured dislocation density.

Irradiation Temperature (°C)	Dose (dpa)	Experimental change in hardness, ΔH_e (GPa)	Calculated change in hardness, ΔH_p (GPa)
RT	0.03	0.92	1.06
RT	0.3	2.31	1.59
500	0.3	0.33	0.39
500	3	0.47	0.46

2.6 Conclusions

Heavy ion irradiation has been conducted on NiFeMnCr HEA from room temperature to 700 ˚C. Changes in microstructure and mechanical properties have been characterized by X-ray diffraction, SEM, TEM and nano-indentation. Compared with conventional Fe-Ni-Cr austenitic alloys, this HEA shows similar behavior in the following aspects:

(1) Retain good phase stability after room temperature and elevated temperature (400 – 700 ˚C) ion irradiation.

(2) Cr depletes and Ni enriches at grain boundaries. Magnitude of elemental segregation shows a bell-shaped curve with respect to temperature, where segregation magnitude maximizes at intermediate temperature.

(3) Hardness increases as irradiation dose increases.

On the other hand, this HEA also reveals better radiation resistance behavior than conventional alloys after high temperature (400 – 700 ˚C) radiation up to 10 dpa:

(1) Suppressed temperature dependence of dislocation growth

(2) No observable voids within TEM detection limit

(3) Suppressed solute segregation for Cr and Ni at grain boundaries

(4) Higher peak segregation temperature for Cr and Ni

CHAPTER THREE
NEUTRON IRRADIATION AND POST-IRRADIATION EXAMINATION

3.1 Introduction

As discussed in Chapter 2, while ion irradiation can explore fundamental radiation effects in materials including HEAs, it cannot directly simulate the neutron irradiation conditions that structural materials experience in actual nuclear reactors. Also, due to the limited ion-irradiated volume available for characterization, many experimental techniques developed for bulk materials do not apply for ion-irradiated samples. Thus, neutron irradiation is of critical importance to validate material performance in actual nuclear reactor environment as well as to complement ion irradiation studies to provide a more comprehensive understanding of radiation effects in HEA.

While numerous previous studies have used transmission electron microscopy (TEM) alone to characterize voids, positron annihilation spectroscopy (PAS) was also utilized in the present study to explore small vacancy-type defects that are below TEM resolution limits[79-81]. In addition, PAS can also provide information on the chemical environment near positron annihilation sites, i.e., near vacancies and dislocations[82, 83], which can provide critical information on the short-range chemical order of HEAs after irradiation. Room temperature hardness, tensile properties and electrical resistivity were also measured. The temperature-dependent evolution of these microscopic and macroscopic properties was also investigated by post-irradiation annealing. The ultimate goal of the post-irradiation examination (PIE) is two-fold. From the aspect of engineering evaluation, the fundamental stability of an HEA in an extreme neutron irradiation environment is empirically tested to examine the feasibility of HEAs as nuclear structural components. From the aspect of scientific understanding, experimental characterization after irradiation and isochronal annealing can provide a comprehensive overview on neutron radiation effects of HEA and the kinetic evolution of these effects over a wide range of temperature.

.

3.2 Neutron irradiation and sample preparation

For this neutron irradiation study, six SS3 miniature sheet tensile specimens (overall length 25 mm, thickness 0.76mm, gage length 7.6 mm and gage width 1.5 mm) and two 3mm diameter x 0.4 mm thickness TEM disks were prepared for each irradiation condition. One control sample of each geometry was prepared for comparison. After machining, these specimens were annealed at 900 ˚C for 4hrs at vacuum to reach a fully recrystallized microstructure with grain size of ~ 35 microns.

Neutron irradiation was conducted in the High Flux Isotope Reactor (HFIR) at Oak Ridge National Laboratory (ORNL). Specimens were wrapped in thin aluminum foil and placed in a perforated capsule in the reactor core to allow maximum cooling from the flowing water coolant while preventing direct coolant contact with samples. Specimens were irradiated at ~60 ˚C to doses of either 0.1 or 1 dpa. The low dose samples were irradiated for 32.4 hrs at neutron flux of 8.57×10^{14} n/cm²·s, and the high dose samples were irradiated for 311.4 hrs at neutron flux of 8.9×10^{14} n/cm²·s.

3.3 PIE at room temperature

All PIE was conducted in the Low Activation Materials Development and Analysis (LAMDA) laboratory in ORNL. After neutron irradiation, electrical resistivity, tensile properties, micro-hardness, and nano-hardness were measured at room temperature. Electrical resistivity was measured by a four-point probe technique on the sheet tensile specimen. A 0.1A current was applied through the outer contacts near the tab region of the specimen, and the voltage drop between two inner contacts on the gage section is measured. The electrical resistivity was the calculated from the measured voltage drop by:

$$\rho = \frac{V \times A}{I \times L}, \qquad \text{(Eq. 3.1)}$$

where V is the measured voltage drop, A is the cross sectional area of the gage section, I is the applied current (0.1 A) and L is the distance between the inner electrodes. All the dimensions were measured by micrometer with 0.001mm precision. Possible orientation or surface effects are considered by repeating measurement after rotating or flipping the sample. The electrical resistivity of all twelve irradiated samples was measured and the average was calculated for each irradiation condition.

Following the resistivity measurement, tensile testing was performed on three SS3 sheet tensile specimens (one control specimen, one 0.1 dpa and one 1 dpa) on a screw-driven mechanical test frame, with a nominal strain rate of $0.0003 s^{-1}$. Anomalous strain in the load vs. crosshead displacement data due to machine compliance effects was corrected to derive the stress-strain relationship. The tensile elongation correction was performed by measuring plastic strain relative to the elastic loading curve (including test frame and specimen grip compliance) for each specimen.

Bulk hardness was measured by a hardness indenter equipped with a Vickers indenter tip. The load and dwell time were set at 500 grams and 10 s. Five indents were made on two TEM disks irradiated to 0.1 dpa and 1 dpa, respectively. Nano-hardness was also measured on the same two TEM disks (after light mechanical polishing of the surfaces with 1 micron diamond lapping film) using a Nano Indenter G200, manufactured by Agilent Technologies, with a Berkovich diamond indenter. All nanoindentation tests were performed in continuous stiffness measurement mode with a constant load rate $\dot{P}/P = 0.05 s^{-1}$. Nanohardness was measured as a function of depth from the point of contact to a depth of about 1000nm. Hardness data below a depth of ~ 300nm from the surface was

discarded due to large data scatter associated with surface roughness. 25 indents were made for each specimen to obtain sufficient statistics for the evaluation of average and error.

TEM characterization was performed on the as-irradiated 0.1 and 1 dpa samples with a 200 keV JEOL 2100F microscope. TEM samples were prepared from the irradiated 3mm TEM disks using focused ion beam (FIB) lift-out methods in a FEI Quanta 3D 200i Dual Beam workstation. The as-prepared TEM samples were further thinned using a low voltage argon ion (900 eV and 90 pA) polishing system (Fischione NanoMill-model 1040) to remove the unwanted FIB surface damage caused by Ga^+ ions.

3.4 Isochronal annealing and post-annealing examination

Isochronal annealing was conducted in a high vacuum (< $5x10^{-5}$ torr) furnace from 100 to 700 ˚C, with a step size of 50 ˚C. Temperature was measured by a type-K thermocouple about 5cm above the sample. During annealing, samples were wrapped in Ta foil in order to minimize oxidation and surface contamination, and for ease of specimen labeling. Also, samples were placed in the same position in the furnace to make sure the experiment condition is repeatable. To minimize temperature overshoot during heating up, several heating programs (Table 3.1) were used for different target temperatures. The sample was annealed at the target temperature for 20min, and the fluctuation in annealing temperature was smaller than 1˚C (except for at 100 ˚C, which was around 10˚C). Finally, samples were cooled to ~30 ˚C by natural furnace cooling (initial cooling rate ~ 10 ˚C/min).

Bulk hardness, electrical resistivity and PAS were measured following each isochronal annealing step. To maximize the use of material, the samples for PAS and electrical resistivity measurement were made from the tested SS3J tensile specimen, whose geometry is shown in Figure 3.1. Two cuts were made (indicated by the red dash lines). Tensile tab A and B were used for PAS, and the longer part of the broken tensile gage was used for electrical resistivity measurement. To separate the effect of tensile deformation and high temperature annealing, electrical resistivity was also measured on an untested SS3 sample before and after 18% uniform elongation. Bulk hardness was measured on the TEM disks. Due to relatively high residual radioactivity of the 1 dpa sample that interfered with measurement of the positron annihilation gamma rays, the PAS experiment was only conducted for 0.1 dpa sample whereas the hardness and electrical resistivity were performed at both doses.

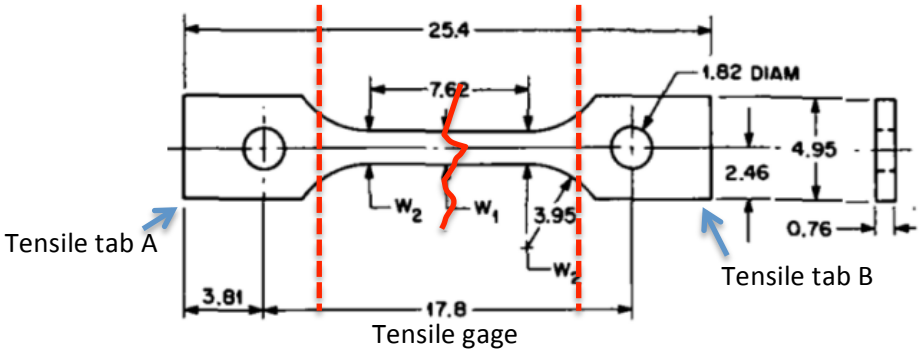

Figure 3.1 Sample geometry for PAS and electrical resistivity measurement.

Table 3.1 Heating programs for isochronal annealing and the resulting temperature overshoot.

Target Temperature (˚C)	Heating program	Overshoot (˚C)
100 - 200	5 ˚C/min to start, 2.5 ˚C/min for the last 20 ˚C	< 10
250 - 350	10 ˚C/min to start, 5 ˚C/min for the last 50 ˚C	< 2
400 - 700	20 ˚C/min to start, 10 ˚C/min for the last 50 ˚C	< 1

For PAS measurement, ^{22}NaCl solution was used as the positron source. A 20uL solution (~ $3.7x10^5$ Bq) was directly deposited onto the surface of tensile tab A and, after the water evaporated, tab A was then covered by the other tensile tab B to make a conventional sample-source-sample geometry. This "sandwich" sample was then wrapped in 10 um thick aluminum foil and placed in a fixed position between the detectors in the PAS system. The system simultaneously measures the time and energy of the incident and annihilation gamma rays to enable both positron annihilation lifetime spectroscopy (PALS) and coincidence Doppler broadening (CDB) analysis. All measurements were performed at room temperature. PALS measurements operate in a double-stop mode and have a calculated system time resolution of ~ 160 ps. Each recorded lifetime spectrum contained a total of 0.8 to $1x10^6$ counts and was analyzed by fitting the exponential decay of two lifetime components, after de-convolution of the experimental resolution function, which we approximated as a weighted sum of three Gaussians. The energies of the two annihilation gamma rays used for CDB analysis were measured by two HPGe detectors facing the sample-source-sample assembly. 10 million annihilation events were collected for the Doppler-broadening spectra. The experimental setup of CDB measurement had a data/background ratio of $5x10^4$. More details on the system can be found in Ref [84].

Bulk hardness and electrical resistivity were also measured after annealing. Since the sample geometry of the broken tensile specimen was different from the unbroken tensile

specimen, the measurement method for electrical resistivity had to be modified. The four electrodes in the four-point probe device were adjusted to fit the length of broken (shorter) tensile gage. The gage region of the sample was placed at a fixed position relative to the four electrodes to make sure that measurements from different annealing temperature were consistent. Voltage drop was still measured under the same applied current, but absolute electrical resistivity was not calculated. Instead, the relative change of resistivity for the broken tensile specimen (constant specimen geometry) was calculated by:

$$\Delta = \frac{V_A - V_0}{V_0} \times 100\% \,, \qquad \text{(Eq. 3.2)}$$

where V_A is the voltage drop after annealing at certain temperature and V_0 is the voltage drop before any annealing.

XRD was performed on 700 ˚C annealed (furnace cooled) and as-irradiated 3mm TEM disks to investigate phase stability due to irradiation and post irradiation annealing. An internal standard (Si SRM640d National Institute of Standard and Technology) was applied on top of the TEM disks to correct the error from sample displacement. The TEM disks were then sealed by Teflon tape to prevent radiation contamination. XRD was conducted on a D2 Phaser benchtop X-ray diffractometer (Bruker INc., Billerica, MA) using Cu Kα radiation (30kV, 10mA). The XRD scan was performed over 10 – 110˚ 2Theta with a step size of 0.004 ˚C and scan time of 11hrs. Diffraction pattern was also collected on a separate bulk, unirradiated control with a scan time of 2hrs.

3.5 Micro-hardness and nano-hardness

Figure 3.2 shows the micro-hardness evolution of the 0.1 and 1 dpa samples as a function of isochronal annealing temperature. The un-irradiated control hardness (indicated by the black dashed line on Figure 3.2) is 128 HV. For the as-irradiated condition, irradiation to 0.1 dpa produced a nearly 60% increase in hardness compared to the un-irradiated sample, and irradiation to 1 dpa exhibited a further increase to approximately double the un-irradiated hardness. The hardness values remained unchanged for both irradiated samples upon post irradiation annealing to temperatures of 100 to 300 ˚C. However, the hardness of the specimen irradiated to 0.1 dpa begins to decrease for annealing temperatures above 300 ˚C, while the hardness decrease of the specimen irradiated to 1dpa does not begin to decrease until around 400 ˚C. The hardness recovery at elevated temperatures for the 1dpa sample is much steeper than that of 0.1dpa. Since annealing of hardness is related to the recovery of radiation induced defects (which are obstacles to dislocation motion), it is possible that the different annealing trends may suggest different defect microstructures in the samples irradiated to 0.1 versus 1 dpa[85]. As will be described in Section 3.9, microstructure characterization of the as-irradiated samples found larger defect clusters in the 1 dpa sample, which would be consistent with higher thermal stability. The hardness of both samples approached the un-irradiated value following the 650 ˚C anneal.

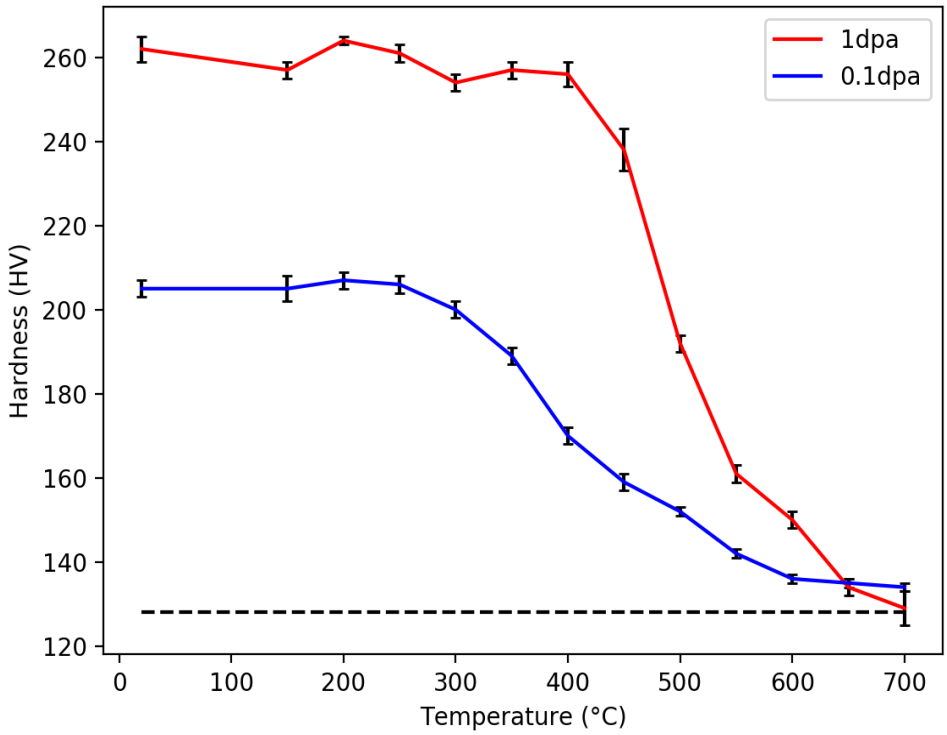

Figure 3.2 Micro-hardness evolution after isochronal annealing. The dashed horizontal line corresponds to the un-irradiated hardness.

Figure 3.3 shows the corresponding depth-dependent nanohardness measurement data on the unirradiated and neutron irradiated samples (exhibiting the well-known indentation size effect)[73]. Figure 3.4 shows a linear fit of hardness squared as a function of the inverse indentation depth according to the Nix-Gao model[73] that was used to verify uniform hardness versus depth for the un-irradiated and neutron irradiated samples. The R-squared values are very close to 1 for all three fitting curves, verifying depth-independent hardness (as would be expected for unirradiated and room temperature neutron irradiated samples). The nanohardness measurement for neutron irradiated samples showed ~ 58% increase for the 0.1dpa sample and ~73% increase after 1dpa at an indent depth of ~800nm, which was roughly comparable to the bulk Vickers hardness measurement at an indentation depth of ~ 3 microns produced by 0.5 kg load. On the other hand, by extrapolation of the Nix-Gao fit in Figure 3.3, bulk hardness can be estimated from the intercepts of the curves. Fitting for data below a 500nm indentation depth results in a bulk hardness of the control, 0.1 and 1dpa samples of 1.20, 2.56 and 2.62 GPa, respectively. This indicates that irradiation has increased hardness by 113% from control to 0.1 dpa, but the hardness barely changes by about 5% from 0.1 to 1dpa, which is in moderate disagreement with the bulk Vickers hardness results discussed

earlier in this section. Figure 3.4 shows the Nix-Gao fit for data at all indentation depths. The fitted Nix-Gao bulk hardness values are 0.76, 2.63 and 2.84 GPa for the control, 0.1 and 1 dpa samples, respectively. Although the R-square values for all fits each exceed 0.99, indicating good fitting quality, it is worth noting that the error in hardness is between 0.07 – 0.44 GPa due to data scatter of extrapolating to the x-intercept from different indentation depth regions.

3.6 Tensile tests

Tensile testing was performed on the three SS3 specimens (one control specimen, one neutron irradiated to 0.1dpa and one to 1dpa) on a screw-driven mechanical test frame, with a nominal strain rate of 0.0003 s^{-1}. Anomalous strain in the load vs. crosshead displacement data due to machine compliance effects was corrected to obtain the relevant engineering stress-strain relationship. The correction involved measuring plastic strain relative to the elastic loading curve (including test frame and specimen grip compliance) for each specimen.

Figure 3.5 shows the representative engineering tensile stress/strain curves of the neutron irradiated high entropy alloy specimens. A pronounced increase in yield strength was observed after 0.1 dpa with an additional increase after 1 dpa. Conversely, the increase in the ultimate tensile stress was more modest in the irradiated specimens. A relatively small increase was observed in the specimen irradiated to 0.1 dpa, with a slight decrease in UTS between 0.1 and 1 dpa. An initial yield drop is observed for both irradiated HEA specimens. It can be seen from Fig. 3.5 that the magnitude of work hardening is decreased by the neutron irradiation, although HEA specimens irradiated to both doses retain moderate work hardening capacity after the initial yield drop. This general behavior of reduced work hardening capacity with increasing neutron dose for irradiation near room temperature is commonly observed in austenitic steels as well as numerous other f.c.c. metals and alloys[86-88]. The uniform and total elongation decreased slightly after 0.1 dpa irradiation, with a pronounced decrease observed after 1 dpa. However, several percent uniform elongation is still observed in the 1 dpa HEA specimen and there is no sign of prompt plastic instability.

Table 3.2 compares the change of yield strength and uniform elongation between HEA in this study and SS316 after similar neutron irradiation condition[87]. Note that uniform elongation is defined by strain to necking[88] in this study (strain to necking measures the plastic elongation after any yield drop up to the post-yield ultimate tensile stress). For both HEA and SS316, yield strength increases by ~150% at 0.1 dpa and ~180% at ~1 dpa. As for uniform elongation, HEA decreases by 14% at 0.1dpa and 77% at 1 dpa. For comparison, SS316 decreases by 38% at 0.1 dpa and 50% at 0.76 dpa.

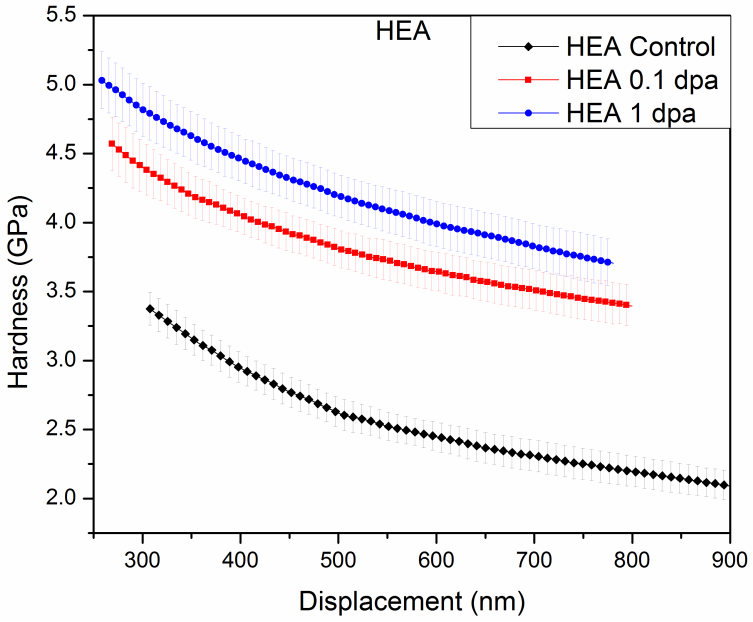

Figure 3.3 Nanoindentation hardness as a function of depth for samples irradiated by neutrons at 70°C from 0.1 dpa to 1 dpa.

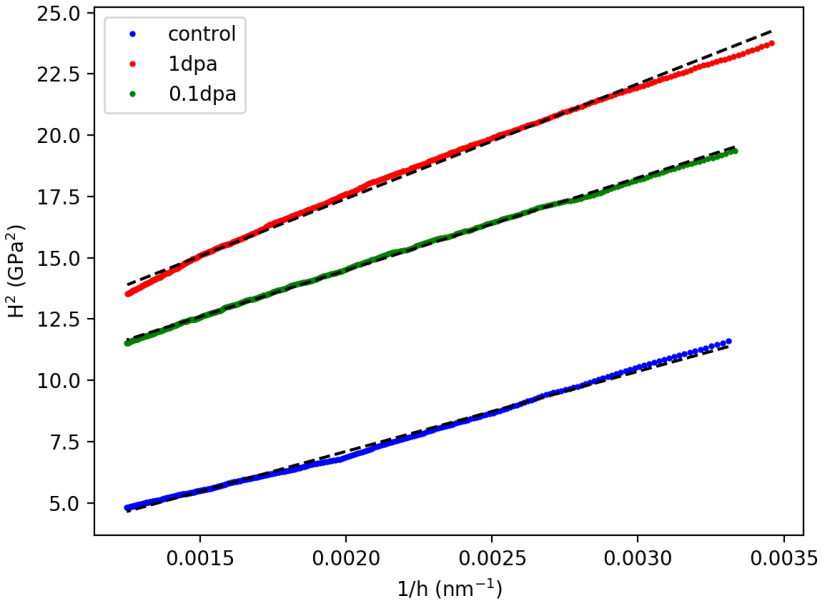

Figure 3.4 Nix-Gao fit of the nanohardness data. R-square value of all three fits are bigger than 0.99, indicating good fitting quality.

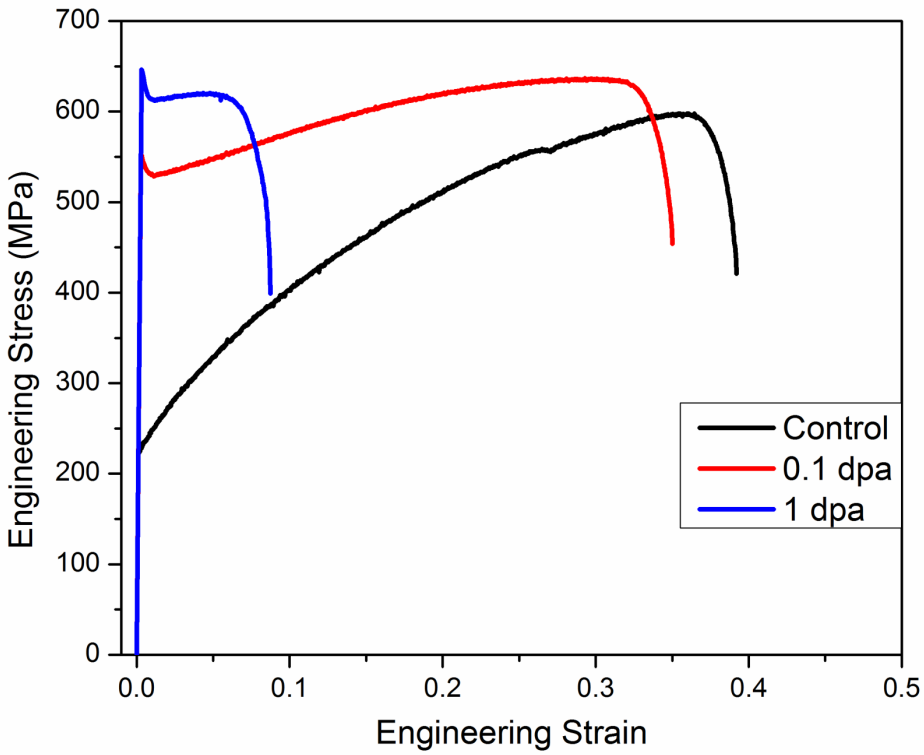

Figure 3.5 Stress-strain behavior of neutron irradiated tensile samples at different doses.

Table 3.2 Comparison of change in tensile properties between HEA in this study and SS316 after neutron irradiation. (a) yield strength (Unit: MPa), (b) uniform elongation.

(a)	**HEA**	**SS316[87]**
Control	220	230
0.1dpa	540	575
1dpa **(0.76dpa for SS316)**	620	660

(b)	**HEA**	**SS316[87]**
Control	0.35	0.60
0.1dpa	0.30	0.37
1dpa **(0.76dpa for SS316)**	0.08	0.30

Both irradiated samples exhibited yield drops, and the magnitude of the yield drop increased with dose. The magnitude of yield drop, however, seems to be larger than that of a typical stainless steel. For HEA, the yield drop was ~24 MPa at 0.1 dpa and ~34 MPa at 1 dpa. For 316 stainless steel, the reported yield drop is ~4 MPa at 0.1 dpa and ~16 MPa at 0.78 dpa[87].

Both HEA and conventional austenitic alloys exhibit a reduction of strain hardening with increasing dose, which indicates that neutron irradiation alters the work hardening behavior. However, the magnitude of the reduction for HEA is more significant. At 1 dpa, the work hardening regime is almost flat, and the difference between ultimate tensile strength and lower yield point is only ~8 MPa. The upper yield point is even higher than ultimate tensile strength. This is somewhat atypical for austenitic Fe-based alloy (304, 316 and 347) because moderate work hardening can still be observed at relatively high dose up to 5 to 10 dpa[74, 87-89]. On the other hand, for pure Ni, work hardening capacity disappears after 0.11 dpa room temperature neutron irradiation[89]. Thus, the observed change in work hardening for this HEA falls between pure Ni and austenitic stainless steel. Since plastic deformation is characterized by the interaction of dislocations and pre-existing solute/radiation induced defects (in the case of austenitic steels, microtwinning is also involved), the moderate differences in yield drop and work hardening magnitude suggest slightly different defect microstructures, or different interaction mode after irradiation. In summary, the difference in tensile properties after neutron irradiation are not pronounced between HEA and SS316.

Since both yield strength (YS) and Vickers hardness (VHN) are controlled by the same deformation mechanism (dislocation pinning), the change in yield strength should roughly correlate with that of hardness, i.e. YS=K*VHN where K is the correlation factor[90]. Previous experimental studies have shown an approximately linear correlation between Vickers hardness and yield strength and this correlation is roughly independent of material composition[76]. In this study, the increasing trend of yield strength and hardness also shows good qualitative agreement. Yield strength rapidly increases by 320 MPa from 0 to 0.1 dpa, but the increasing trend slows down and only increases by 400 MPa from 0 to 1 dpa. On the other hand, bulk hardness increases by 80HV for 0.1dpa and 130HV for 1dpa sample. While more data is needed to obtain a reliable fit for the correlation factor between yield strength and Vickers hardness (See Eq 2.2 in Section 2.5), these two sets of data points at 0.1 and 1 dpa suggests that the correlation factor for this HEA (K) is between 3 and 4. This is generally consistent with the correlation factor used for austenitic stainless steel such as SS316, SS304 and SS347[74, 76].

3.7 Positron annihilation spectroscopy

Since no theoretical positron lifetime calculation has been conducted so far on this type of high entropy alloy, the lifetime data from iron was used as a reference[91]. Iron is chosen as the reference instead of other pure metals because the lifetime of defect clusters in iron

has been extensively studied, and a relatively small difference has been found between vacancy lifetime in bcc Fe and fcc metals. On the other hand, as will be discussed in Chapter 5, theoretical positron annihilation lifetime computation is also conducted for the NiFeMnCr HEA. The computed lifetime will be compared with pure metals to verify if it is reasonable to use Fe as the reference for this HEA. Figure 3.6 shows selected positron lifetime spectra obtained directly from the raw PALS measurements on the HEA specimens. Since positrons are sensitive to free volume in the material, the change in the slope of the decay curves provides information predominantly on the evolution of irradiation induced vacancy-type defects. It is apparent that the long lifetime part is significantly enhanced for the sample following neutron irradiation in comparison with the un-irradiated sample. This indicates that neutron irradiation produced vacancy-type defects. The subsequent isochronal annealing initially promotes the growth and evolution of vacancy defects contained within the sample. The post irradiation anneal at 200°C has little impact on the measured positron lifetime spectrum, implying limited evolution of vacancy defects. A significant recovery of the positron lifetime was observed after the 350°C annealing and continues for the 500°C annealing. The final 700°C annealing (not plotted in Fig. 3.6) did not produce full recovery of the irradiation defects but resulte in an enhanced long lifetime that may be consistent with possible vacancy cluster coarsening.

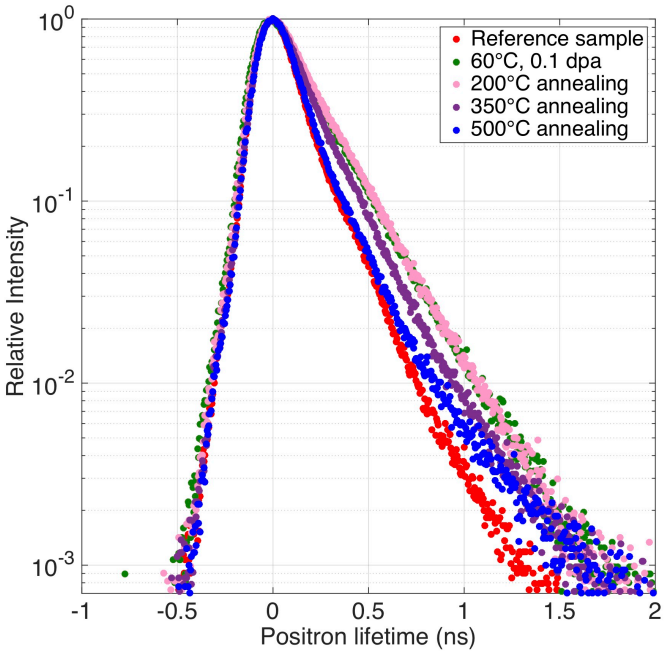

Figure 3.6 Positron lifetime spectra of reference (unirradiated) and neutron-irradiated HEA (as-irradiated and following different annealing conditions).

Depending on the range of defect cluster size and concentration, the experimental positron lifetime spectra can be fit with two or three lifetime components to quantitatively analyze defect density and size evolution[81, 83, 92]. Fitting the measured positron lifetime spectra with two components provided a sufficient fit to the experimental data, which is consistent with a single type of dominant positron trap (vacancy defect). Therefore, the measured PALS spectra were decomposed into two lifetime components after first subtracting the background. The short lifetime, τ_1, known as the reduced bulk lifetime, and the long lifetime, τ_2, representing the positron lifetime in vacancy defects, are extracted together with the associated intensity of each component. The average positron lifetime $< \tau >$ is simply calculated from $< \tau > = \tau_1 I_1 + \tau_2 I_2$, where $I_1+I_2=1$. The positron lifetime contains the information of size and type of the vacancy defects. The vacancy defect concentration can be derived based on the two-state trapping model. The positron lifetimes obtained by fitting the measured lifetime spectra are expressed as

$$\tau_1 = \frac{1}{\tau_B^{-1} + \kappa} \quad \text{(Eq 3.3)}$$

$$\tau_2 = \tau_V \ , \quad \text{(Eq 3.4)}$$

where τ_B is the positron lifetime in the bulk, which is assumed to be 97 ps based on DFT calculations; τ_V is the positron lifetime in vacancy-type defects; and κ is the net positron trapping rate of the defects:

$$\kappa = \frac{I_2}{I_1}(\tau_B^{-1} - \tau_2^{-1}) \quad \text{(Eq 3.5)}$$

The trapping rate is usually assumed to be proportional to the defect concentration (C_V),

$$\kappa = \mu C_V \ , \quad \text{(Eq 3.6)}$$

where μ is the specific positron trapping coefficient for each defect, and is a function of defect type, charge state, and size. Since μ is not available for this Co-free HEA, only the trapping rate will be shown to represent the defect concentration.

The PALS analysis results are shown in Figure 3.7. The diagram on the top of the figure shows the average lifetime as well as the short (τ_1) and long (τ_2) lifetimes of the 0.1 dpa sample following each annealing stage, while the diagram on the bottom shows the intensity of the long lifetime component (with the intensity of the short lifetime component equal to 100% - I of the long lifetime component). Figure 3.8 shows the trapping rate evolution as a function of annealing temperature. Several observations can be made from these two curves. First, in comparison to the lifetime data of pure iron, τ_2 should predominantly represent small vacancy clusters composed of 2 to 5 single vacancies. As will be discussed in Chapter 5, positron lifetimes of small vacancy clusters are also computed to identify the size of clusters in the PALS analysis and to verify if Fe is a proper reference for positron lifetime. Note that τ_2 is a collective result based on the

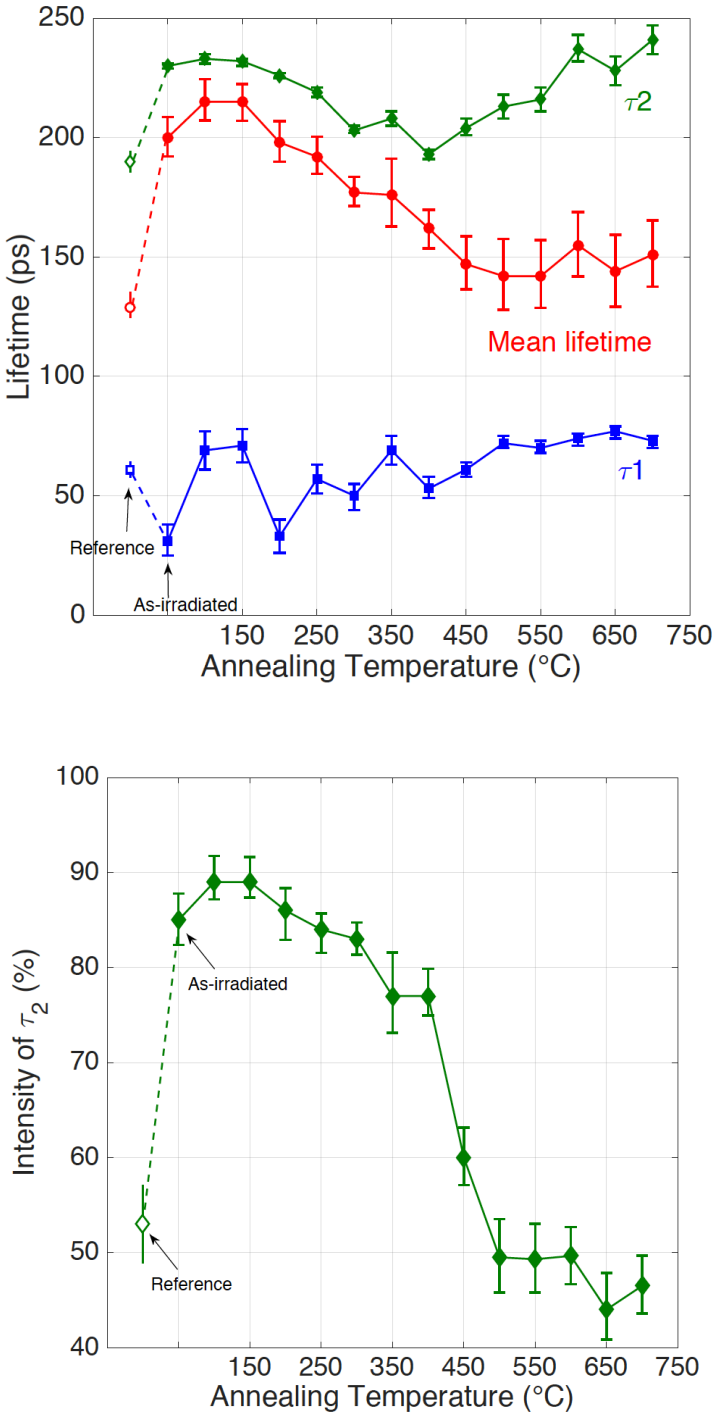

Figure 3.7 Lifetime (top) and intensity (bottom) evolution after isochronal annealing at 100 – 700 ˚C.

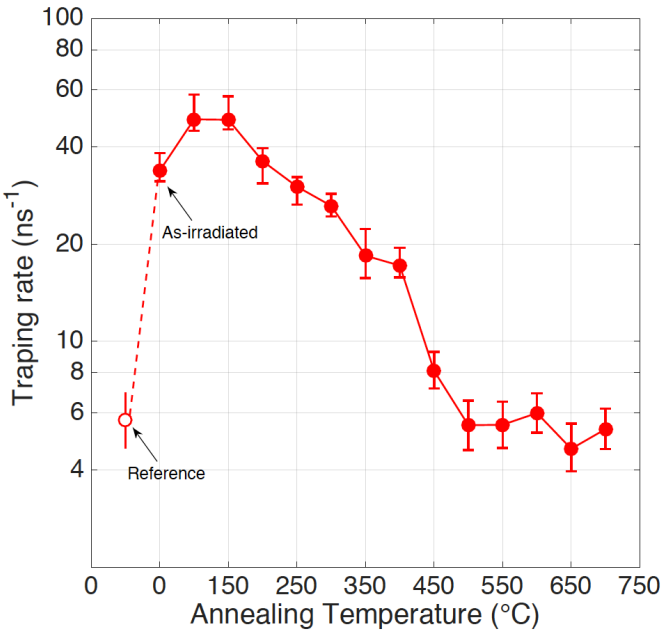

Figure 3.8 Trapping rate evolution after isochronal annealing at 100 – 700 ˚C.

weighted (by the specific positron trapping coefficient) positron lifetimes in all present vacancy defects in the sample. A larger $\tau 2$ refers to the presence of larger vacancy defects while the presence of smaller vacancy defects leads to the measurement of smaller τ_2. Second, τ_2 initially slowly decreases for annealing temperatures from 200 to 400 ˚C, and then slowly increases from 400 to 700 ˚C. The decrease of the long positron lifetime in the low temperature annealing regime is consistent with an increase of the local electron density of the positron trapping sites, which may stem from the shrinkage of vacancy clusters by thermal annealing (emission of vacancies), absorption of self interstitial defects or interstitial clusters, or from the absorption of gaseous species like transmutant helium. Meanwhile, the intensity of τ_2 has a general decreasing trend while a sharp decrease was observed in the temperature regime from 400 to 500°C. This transition point, 400 ˚C, may suggest the initialization of the so-called stage V recovery process, which represents the thermal dissociation of vacancy clusters[32, 93]. The rapid drop of defect concentration, indicated by the nearly 3 times decrease of trapping rate, also suggests the start of this major recovery stage. Third, the average lifetime continuously decreases from 100 to 500 ˚C, and then fluctuates around 140 – 150 ps from 500 to 700 ˚C, having a very similar trend as the trapping rate. Note the mean lifetime of the irradiated sample after 700 ˚C anneal is still significantly higher than the unirradiated control value of 129ps. Finally, the trapping rate generally decreases as temperature increases, suggesting the continuous decrease of defect density with increasing annealing temperature. It approaches that of the reference sample level at about 500 ˚C. While the trapping rate shows the defect cluster density drops back to the unirradiated reference level after 700 ˚C anneal, both the mean lifetime and τ_2 indicate the existence of a small number of relatively large vacancy clusters that are thermally stable at 700 ˚C.

While PALS measures the lifetime of the positrons within the sample between implantation and annihilation, CDB measures the energy difference between the two annihilation gamma rays. This energy difference is caused by the Doppler shift that is correlated with the momentum of the annihilation electron[83]. The positron CDB measurement examines the interaction probability of positrons with core or valence electrons. Figure 3.9 shows several representative momentum distribution curves from the CDB measurement. The low momentum part represents positron annihilation with valence electrons while the high momentum part represents annihilation with core electrons. Compared with the reference sample, the irradiated samples exhibit lower intensity in the high momentum regime. This indicates that positrons are more likely to interact with valence electrons in irradiated samples, which is consistent with the presence of free volume containing radiation-induced defects inside the material.

The parameters S and W are commonly used to assess the balance of positron annihilations between the valence and core electrons, respectively, and can also provide a chemical signature of the positron annihilation sites. S represents the fraction of low-momentum annihilation (defined by $P_L<0.382$ a.u.), and W represents the fraction of high-momentum annihilation (defined by $1.0<P_L<4.0$ a.u.) By plotting the ratio of high

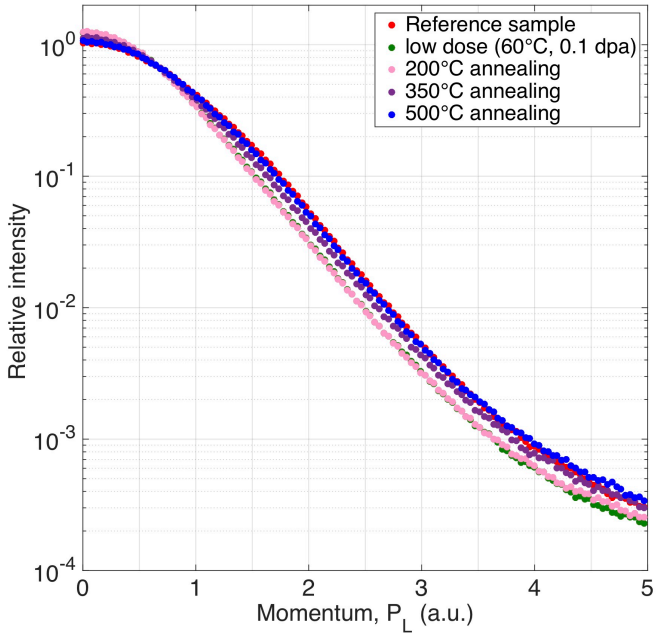

Figure 3.9 Raw data from CDB measurement.

momentum region (W) vs low momentum region (S), which defines the S-W plot shown in Figure 3.10, the slope of the curve can provide information on the defect type in the material. Two observations can be made from Figure 3.10. First, all the data points fall along a single line with a common slope suggesting that as annealing temperature increases, there is no significant change of the chemical environment of the positron annihilation sites. This indicates that the nature of the vacancy defects is consistent following all annealing stages. Second, the data points generally move upward as annealing temperature increases. This is consistent with a continuously decreasing defect density with increased annealing temperature. Specifically, while a small change in the relative S-W data point position is observed from 100 to 200 ˚C and from 600 to 700 ˚C, a much larger relative change in S-W position is observed from 250 to 550 ˚C. This CDB S-W data analysis is generally consistent with the rapid drop of mean lifetime and trapping rate between 200 to 500 ˚C.

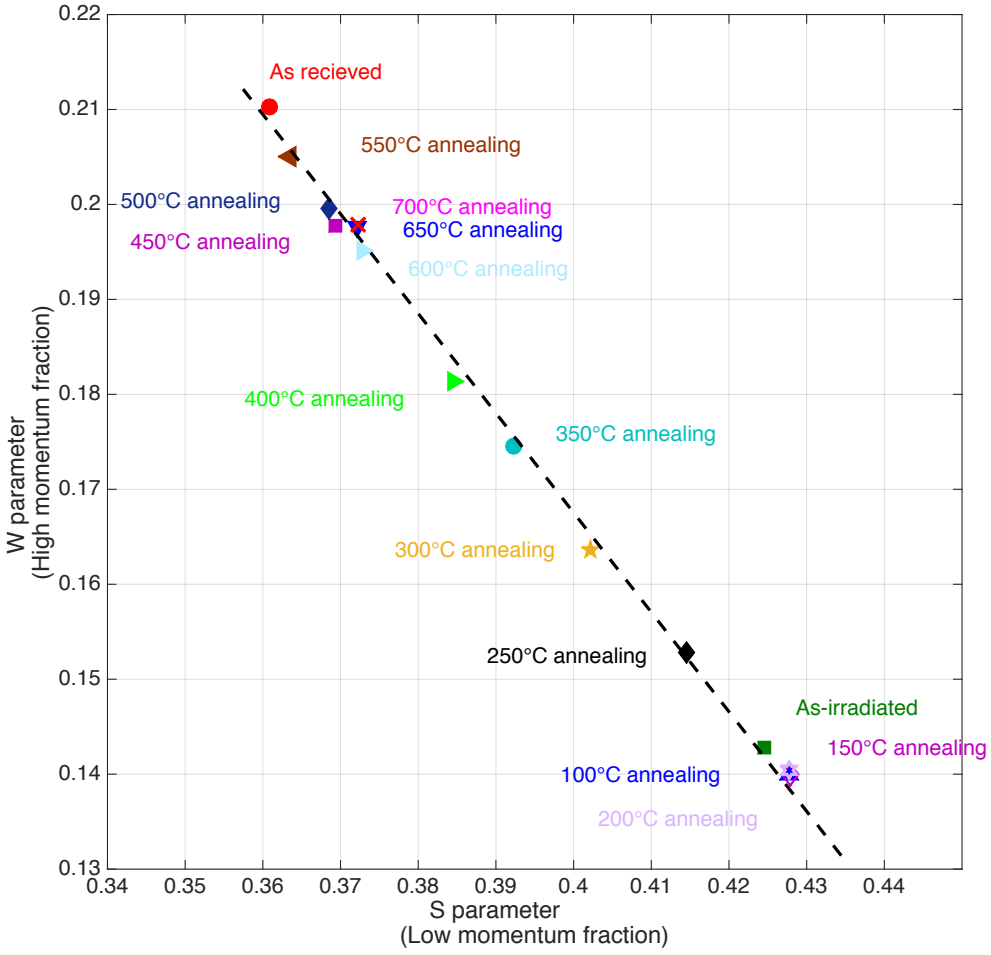

Figure 3.10 S-W plot from CDB measurement.

3.8 Electrical resistivity

At room temperature, the un-irradiated control electrical resistivity is 112.7±1.2 μΩ·cm. For the as-irradiated specimens, the relative change in electrical resistivity due to irradiation is 15.6% (130.2±0.4 μΩ·cm) for the sample irradiated to 0.1 dpa, and 17.0% (131.8±0.6 μΩ·cm) for the 1 dpa sample. The change of electrical resistivity with respect to annealing temperature is shown in Figure 3.11. Though the irregular shape of the broken tensile sample caused relatively large uncertainties in the measurement, some qualitative trends can still be observed from the curves. After annealing, the electrical resistivity of the unirradiated control shows a moderate decreasing trend, which could possibly be associated with a short-range rearrangement of solute atoms[94]. Conversely, there is no consistent annealing trend for the 0.1 and 1 dpa irradiated samples up to 700 ˚C. Electrical resistivity measurements on a control HEA sample before and after 18% engineering strain showed that the dislocations produced by tensile deformation produces a negligible increase in resistivity: the measured change in resistivity was less than ~1%. Thus, the radiation-induced feature(s) responsible for the large resistivity increase after neutron irradiation to 0.1 and 1 dpa at ~60 ˚C appear to be stable upon tensile deformation or annealing to temperature as high as 700 ˚C. As discussed later in Section 3.10.2, it is possible that the resistivity increase is dominated by a short-range rearrangement of solute atoms.

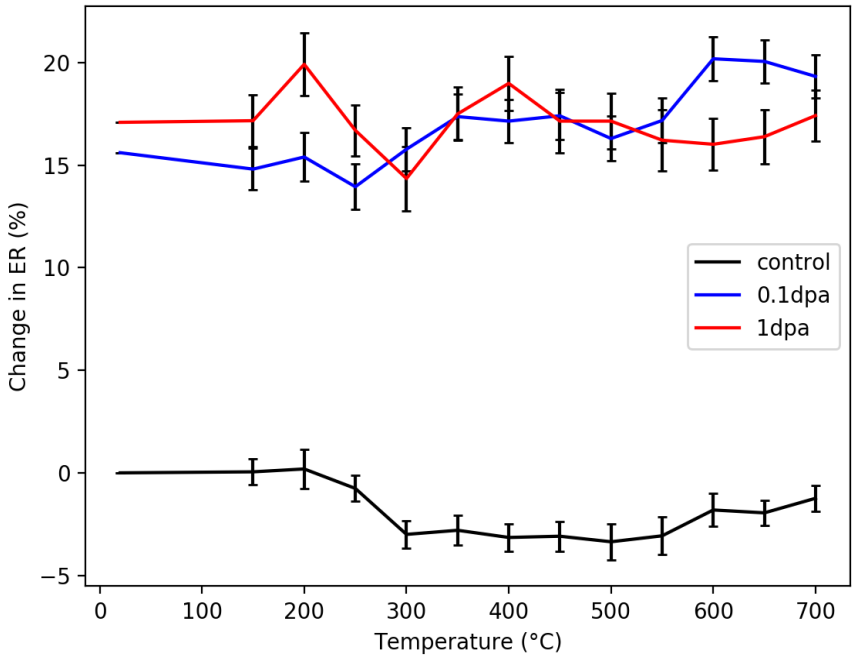

Figure 3.11 Change in electrical resistivity after isochronal annealing.

3.9 Phase stability from XRD and TEM

Figure 3.12 shows the XRD patterns measured from the unirradiated control and irradiated samples at different conditions. Data is shown just for 40 – 100˚ diffraction angles for the purpose of eliminating the high background intensity induced by the Teflon tape. No evidence of amorphization, or any other phase change, was observed in the irradiated samples. For all irradiated samples, other than the indexed FCC peaks from HEA, the only peaks present can be attributed to the Si standard. Thus, neutron irradiation up to 1dpa and post-irradiation annealing up to 700 ˚C did not produce any detectable phase change (< 3 wt%) in this HEA.

Figure 3.13 exhibits the bright field (BF) TEM images and corresponding selected area electron diffraction (SAED) patterns of NiFeMnCr HEA irradiated at (a) 0.1 dpa and (b) 1 dpa. It can be observed from the SAED pattern that the NiFeMnCr HEA still retains a single phase fcc structure after neutron irradiation, which is consistent with the XRD results. Numerous irradiation-induced defects are present in the BF images. At 0.1 dpa, irradiation-induced defects appear as discrete "black dots", which are interpreted to be tiny dislocation loops with most defects having a diameter smaller than 10 nm (Fig.13 (a)). As the dose increased to 1 dpa, the size of the dislocation loops is dramatically increased. This observation of larger defect clusters at 1 dpa compared to 0.1 dpa (with comparable defect cluster densities) is consistent with the slight enhancement in radiation hardening at 1 dpa vs. 0.1 dpa and also with higher resistance to thermal annealing of radiation hardening due to anticipated higher thermal stability of larger dislocation loops[95].

3.10 Discussion of results from neutron irradiation study

3.10.1 Interpretation of nano-hardness and micro-hardness results

Indentation hardness measurements have been extensively used to characterize the mechanical properties of irradiated material. Semi-empirical correlations[75, 76] have been proposed to estimate the tensile strength from micro-hardness measurements of neutron irradiated austenitic and martensitic steels. On the other hand, nano-indentation experiment can be performed using much smaller sample volumes and smaller indentation depths than traditional micro-hardness testing. Thus, nano-indentation is a particularly desirable technique to evaluate mechanical properties for ion-irradiated samples, where the effective ion damaged region is ~1-5 μm for medium energy (~3 – 9 MeV) heavy ion irradiation. However, the linear correlation between micro-hardness and tensile strength does not apply for nano-hardness and tensile strength due to so-called indentation size effects (ISEs) at the nanoscale associated with geometrically necessary dislocations and other physics processes[73, 96]. A reasonable correlation between micro-hardness and nano-hardness is thus of critical importance for the prediction of tensile properties changes for ion-irradiated alloys.

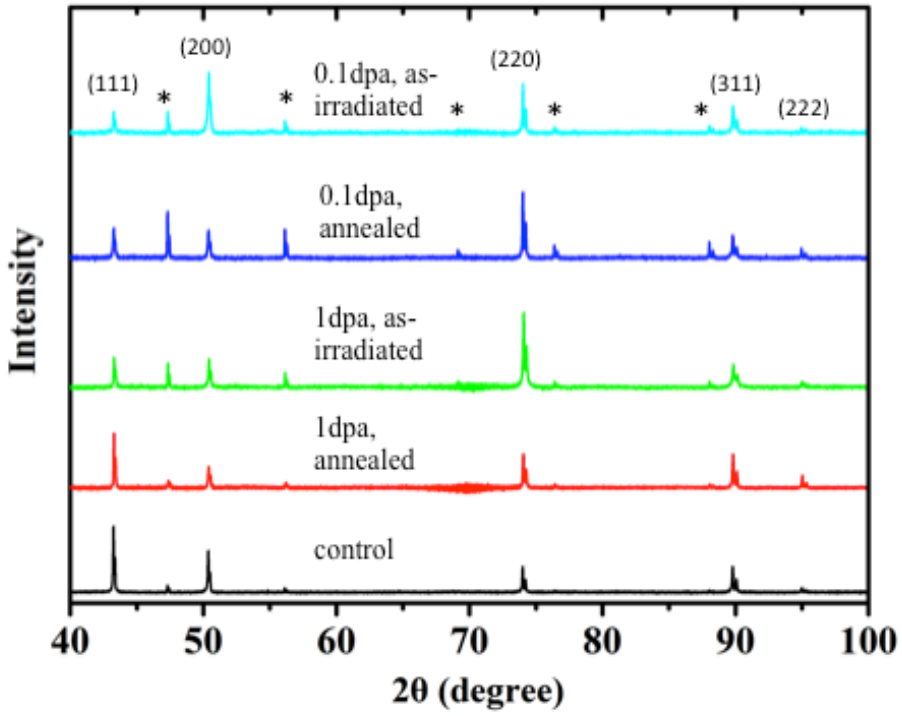

Figure 3.12 XRD patterns of irradiated and un-irradiated control HEAs. Asterisks mark peak positions of Si standard.

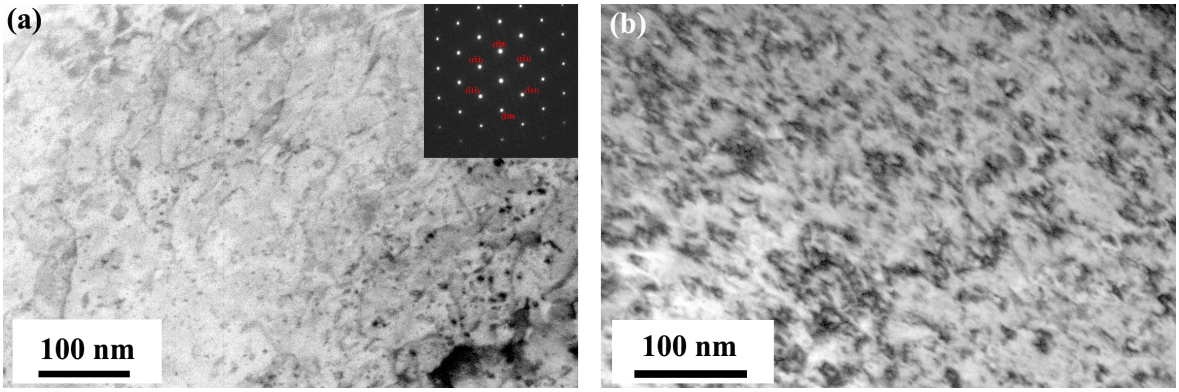

Figure 3.13 BF TEM images and corresponding SAED patterns (along [110] zone axis) of NiFeMnCr HEA irradiated at (a) 0.1 dpa and (b) 1 dpa.

In this study, H_0 is computed from nano-hardness data based on Nix-Gao model (Eq. 3.7), and is used to correlate with micro-hardness measurement results, as:

$$\frac{H}{H_0} = \sqrt{1 + \frac{h^*}{h}}, \qquad \text{(Eq. 3.7)}$$

where H is the indentation hardness at indentation depth h, and h^* is a characteristic length. In Section 3.5, data for indentation depths >500nm was used to compute H_0 and correlate with micro-hardness. It is worth pointing out that this correlation is sensitive to the choice of fitting range for indentation depth (despite very good R-square values in this study). For example, if the whole 300-900 nm indentation depth data set is used to compute H_0, the results would show 240% increase in nano-hardness from control to 0.1dpa, and 270% increase in nano-hardness from control to 1dpa. Fitting based on >500nm indentation depth versus whole indentation depth would thus result in different correlation between micro-hardness and nano-hardness.

Table 3.3 summarizes the change in indentation hardness and tensile strength for HEA in this study. Except for nano-hardness computed from 300 – 900 nm indentation depth, the strength increases from the hardness tests fall in between the yield stress and ultimate tensile stress values measured from tensile testing. This is qualitatively understandable since indentation hardness tests typically involve a wide range of plastic deformation levels under the indenter ranging from plastic yielding (~0.1% deformation) at the elastic-plastic boundary far from the indenter to >10% deformation adjacent to the indenter. While semi-empirical linear correlations[75, 76, 97] have been proposed between nano-hardness and micro-hardness, and between micro-hardness and tensile strength, these simple linear correlations do not work well for the neutron irradiated HEA in this study. It is apparent that any correlation factors computed from the data in Table 3.3 would have large uncertainty and cannot provide accurate estimate of tensile stress from microhardness, or microhardness from nanohardness.

The large quantitative uncertainties in these semi-empirical correlations have several implications: While tip geometry differences between Vickers indentor in microhardness and Berkovich indenter in nanohardness will result in slightly different hardness, this effect is relatively small and cannot fully account for the discrepancy in the measurement. ISEs[73], which describe the strong inverse relationship between hardness and size of the indent, are expected to be the dominant factor that causes this discrepancy. While the Nix-Gao model is a well-tested law to model ISE for nanoindentation and provide relatively accurate fitting for control and neutron irradiated samples in this study, it may not be practical to extrapolate this model from indentation sizes in nanohardness testing to microhardness testing. This is because the material conditions sensed by the nanoindenter and microindenter can be very different due to the large difference in their length scale. This is particularly significant for indentation tests on samples with dislocation spacing between the length scale of the nanoindenter and microindenter[96]. In this case, while the microindenter senses dislocations, nanoindenter senses a dislocation-free zone. Thus, the microindenter can initiate plastic deformation by dislocation motion, but a high stress comparable to the ideal strength is required for the nanoindentor to

Table 3.3 Comparison of room temperature hardening changes (relative to un-irradiated sample) in neutron irradiated HEA from indentation and tensile testing.

	0.1 dpa	1 dpa
Nanoindentation, 300-900nm	240%	270%
Nanoindentation, >500 nm	113%	118%
Vickers hardness (500g)	60%	105%
Tensile yield stress	145%	182%
Ultimate tensile stress	8%	4%

nucleate new dislocations and overcome the "dislocation starved" condition[98, 99]. Therefore, the underlying deformation mechanisms would be very different for these two cases. Thus, extrapolation of the Nix-Gao theory, which is based on geometrically necessary dislocations and does not consider "dislocation starved" conditions, from the nanohardness length scale to the microhardness length scale may not provide a quantitatively accurate comparison due to different volumes being probed. Finally, the average plastic deformation induced even by relatively macroscopic Vickers indentation can vary under the same indenter force for materials with different microstructures (different work hardening capacities). Thus, the yield strength correlation with Vickers hardness can have large uncertainty due to the variation in average microindentation plastic strain. In summary, correlative relations between micro-hardness, nano-hardness and tensile strength are still far from perfect to provide accurate prediction of tensile strength from indentation hardness.

3.10.2 Change in electrical resistivity after irradiation and after annealing

Radiation-induced change in electrical resistivity has been studied on pure metals and a series of concentrated Cr-Fe-Ni alloys after neutron[100-103] and electron irradiation[104, 105] at low temperature. While change in electrical resistivity can be induced by local ordering/disordering for alloys, this effect does not exist for pure metals; in pure metals, the resistivity increase is dominated by scattering from radiation induced defect clusters. Based on the defect production model, these prior studies calculated the "saturation resistivity", which estimates the maximum increase in electrical resistivity solely from radiation-produced defects. Also, since these prior irradiations were performed at cryogenic temperatures, point defect recombination by long-range migration was prohibited. Thus, this "saturation resistivity" is basically an upper bound for change in electrical resistivity caused by point defects and defect clusters at any irradiation temperature or dose (ignoring potential contributions due to changes in short range order of solute atoms). Table 3.4 listed the pre-irradiation resistivity and saturation resistivity increase $\Delta\rho_s$ for Ni, Fe and single f.c.c phase Fe-Ni-Cr alloys. $\Delta\rho_s$ ranges from 1 μΩ·cm for Ni to 4.4 μΩ·cm for Fe-16Cr-25Ni. Note that since up to 80 – 90 % of defects present during 4 K irradiation would recombine via thermal recombination above stage I recovery temperatures (typically < 100K for metals)[106, 107], the saturation resistivity

Table 3.4 Resistivity before irradiation (measured at 4K) and saturation resistivity ($\Delta\rho_s$) for pure metals[101, 102, 108] and austenitic Fe-Ni-Cr alloys[104]. Metals are irradiated by neutrons at 5K and alloys are irradiated by electrons at 20K (Units: μΩ·cm).

	Resistivity before irradiation	Saturation resistivity, $\Delta\rho_s$
Ni	0.00865	1
Fe	0.135	4
Fe-16Cr-20Ni	55.2	4.2
Fe-16Cr-25Ni	64.4	4.4
Fe-16Cr-45Ni	95.6	1.6

increase caused by radiation defects at >300K neutron irradiation would be much smaller than 1 – 4.4 μΩ·cm. However, the measured change in electrical resistivity of as-irradiated NiFeMnCr is 17±1.3 μΩ·cm at 0.1dpa and 19±1.3 μΩ·cm at 1dpa, both of which are significantly larger than these $\Delta\rho_s$ values. Unless there is major (>10x) fundamental difference in the Frenkel pair production process or defect cluster properties between NiFeMnCr HEA and Cr-Fe-Ni alloys, other critical radiation-induced processes must take place to account for the observed large increase in electrical resistivity in the neutron irradiated HEA specimens.

In solid solution alloys including austenitic Fe-Cr-Ni alloys, changes in short range order (SRO) or local ordering/disordering effects can produce pronounced changes in electrical resistivity that typically dwarf the changes associated with radiation-induced defect formation. Radiation mixing and diffusion can both induce changes in SRO. While the former physical process does not necessarily involve thermally activated defect migration, the latter one does. Thus, in some circumstances, sufficiently high temperature is needed to activate the migration of interstitials or vacancies, change the SRO and produce the resulting change in electrical resistivity. For example, Dimitrov et al[103] performed neutron irradiation at 24K and 401K for Fe-16Cr-25Ni alloy. Since defect recombination is largely enhanced at 401K, the rate of electrical resistivity increase due to radiation defects should be smaller for samples irradiated at 401K than that at 24K. However, their experiment results showed that the initial resistivity increased at a rate 10 times larger for 401K than for 24K irradiation, suggesting that SRO was the dominant contributor to the observed changes in the resistivity (much more pronounced than radiation induced defects contribution at this elevated temperature).

In addition to the as-irradiated condition, electrical resistivity changes due to SRO (or disordering) can also be monitored through thermal annealing before or after irradiation in conventional alloys. Table 3.5 lists the resistivity before irradiation and the change of resistivity after annealing for a number of single phase f.c.c Fe-Cr-Ni alloys. Due to the absence of pre-existing defects such as dislocations, the resistivity change during annealing before irradiation, $\Delta\rho_b$, should be solely caused by changes in SRO. Depending on solute type and concentration, $\Delta\rho_b$ ranged from -0.3 to -1.0 μΩ·cm in these conventional Fe-Cr-Ni alloys. Regarding the resistivity change after post-irradiation

annealing, $\Delta\rho_a$, both radiation defect annihilation and changes in SRO could potentially have an effect. The decrease of resistivity due to reduction of defect concentration, $\Delta\rho_1$, mainly occurs at low temperature and ranges from -0.2 to -0.5 μΩ·cm. On the other hand, the increase of resistivity due to change in SRO, $\Delta\rho_2$, mainly take place at high temperature and ranges from 0.3 to 2.0 μΩ·cm in these conventional Fe-Cr-Ni alloys. Since the absolute value of $\Delta\rho_2$ is consistently larger than $\Delta\rho_1$, SRO is a more important controlling factor for electrical resistivity than defects concentration for all of the listed Fe-Cr-Ni alloys. As well, for Fe-Cr-Ni alloys with fixed Cr concentration (Fe-16Cr-20Ni, Fe-16Cr-25Ni and Fe-16Cr-45Ni), increasing Ni solute concentration produced an increase in the SRO component $\Delta\rho_2$. This trend also applies for the alloys with fixed Ni, but increasing Cr concentration. Thus, as chemical complexity increases, change in SRO can induce larger electrical resistivity change for Fe-Cr-Ni alloys. Since the chemical compositions of these concentrated Fe-Cr-Ni alloys are similar to the NiFeMnCr HEA in this study, SRO may also be crucial for the observed change of electrical resistivity for NiFeMnCr HEA. Finally, since the chemical complexity within this NiFeMnCr HEA is higher than any of the listed Fe-Cr-Ni alloys, it is possible that SRO change in NiFeMnCr can potentially induce even larger electrical resistivity changes than conventional Fe-Cr-Ni alloys. It is notable that the overall scale of the measured change (> 10 μΩ·cm) in neutron irradiated NiFeMnCr is much larger than any of the $\Delta\rho_2$ values listed in Table 3.5.

Regarding resistivity evolution during annealing of conventional Fe-Cr-Ni alloys, it is worth noting that this process takes place below 1000K for annealing before irradiation, and below 600K for post-irradiation annealing for all of the Fe-Cr-Ni alloys in Table 3.5. However, for the NiFeMnCr HEA in this study, the electrical resistivity does not show any sign of change up to the annealing temperature of 973K. Although further characterization is needed to confirm the physical cause of this behavior, the pronounced radiation-induced resistivity increase and the lack of an annealing effect on electrical

Table 3.5 Resistivity before irradiation (measured at 4K) and change of resistivity due to annealing before ($\Delta\rho_b$) and after 20K electron irradiation ($\Delta\rho_a$) for austenitic Fe-Ni-Cr alloys[104, 105]. $\Delta\rho_a$ is composed of resistivity change due to defects annealing ($\Delta\rho_1$) and change in SRO ($\Delta\rho_2$). The listed temperature ranges indicate the annealing temperatures to initiate the resistivity change (Units: μΩ·cm).

	Resistivity before irradiation	$\Delta\rho_b$, anneal before irradiation (800 – 1000K)	$\Delta\rho_a$, anneal after irradiation	
			$\Delta\rho_1$ (20 – 200K)	$\Delta\rho_2$ (200 – 600 K)
Fe-16Cr-20Ni	55.2	-0.4	-0.5	0.6
Fe-16Cr-25Ni	64.4	-0.4	-0.5	0.75
Fe-16Cr-45Ni	95.6	-1.0	-0.5	2.0
Fe-8Cr-25Ni	59	-0.3	-0.2	0.3
Fe-10Cr-25Ni	61.3	-0.3	-0.2	0.4
Fe-13Cr-25Ni	63.2	-0.3	-0.2	0.6
Fe-16Cr-25Ni	64.4	-0.4	-0.2	0.7

resistivity of the irradiated HEA samples suggests the possibility that the resistivity increase is associated with irradiation-induced changes in solute SRO that do not thermally anneal up to 700 ˚C. This unique thermally stable feature of HEA will be further discussed in Section 3.10.4.

3.10.3 PALS measurements: comparison between HEA and conventional f.c.c metal

The PALS measured from the NiFeMnCr HEA shows similar behavior to typical fcc metals below stage III (vacancy migration) temperature. First, for the as-irradiated microstructure, small vacancy clusters composing of several vacancies appear to be present. Second, a rapid decrease in trapping rate and τ_2 intensity occurs at an intermediate annealing temperature (cf. Fig. 3.14 for the behavior in Cu[81]). This temperature is usually referred to as the Stage V recovery temperature, corresponding to thermal evaporation of vacancies from vacancy clusters initially produced directly in displacement cascades. Third, before and near stage V recovery temperature, the variation in τ_2 is generally small.

On the other hand, the measured PALS data within this study also shows some different features from conventional fcc metals. Figure 3.14 shows the evolution of lifetime and trapping rate for neutron irradiated Cu at similar dose and temperature[81]. First, it is important to note that the trapping rate in irradiated and post-irradiation annealed Cu remains constant up to the stage V temperature, whereas the trapping rate of the annealed HEA gradually decreases with increasing temperature below the apparent Stage V temperature. The annealing of vacancy clusters at low temperature, which is not present in Cu, is possibly caused by recombination with mobile interstitial clusters. Second, above the stage V recovery temperature, the evolution of vacancy clusters in HEA is different from typical fcc metals. While τ_2 slightly increases from 193ps at 400 ˚C to 216ps at 550 ˚C for HEA, it increases dramatically in irradiated Cu from 200ps at 400 ˚C to ~400ps at 550 ˚C. This indicates that the growth of vacancy clusters (small cavities) in HEA is much less dependent upon temperature than pure copper, but it must be recognized that there is a difference in the melting temperature between Cu and the HEA. The slower growth rate of vacancy clusters in HEA may be consistent with sluggish diffusion[21, 52, 109], one of the key proposed unique phenomena for high entropy alloys.

In addition, the trapping rate in typical f.c.c. metals such as Cu continuously decreases as $\tau 2$ increases. In the HEA, however, the trapping rate initially decreases at 400 – 500 ˚C and then plateaus at ~5 ns^{-1}. In copper, the trapping rate evolution is consistent with This the coarsening of small vacancy clusters into microvoids through an Oswald ripening process as temperature increases. On the other hand, in the HEA, change in defect size and density slows down above 500 ˚C. The decreased rate of the coarsening process could be related to the presence of transmutant He produced during neutron irradiation.

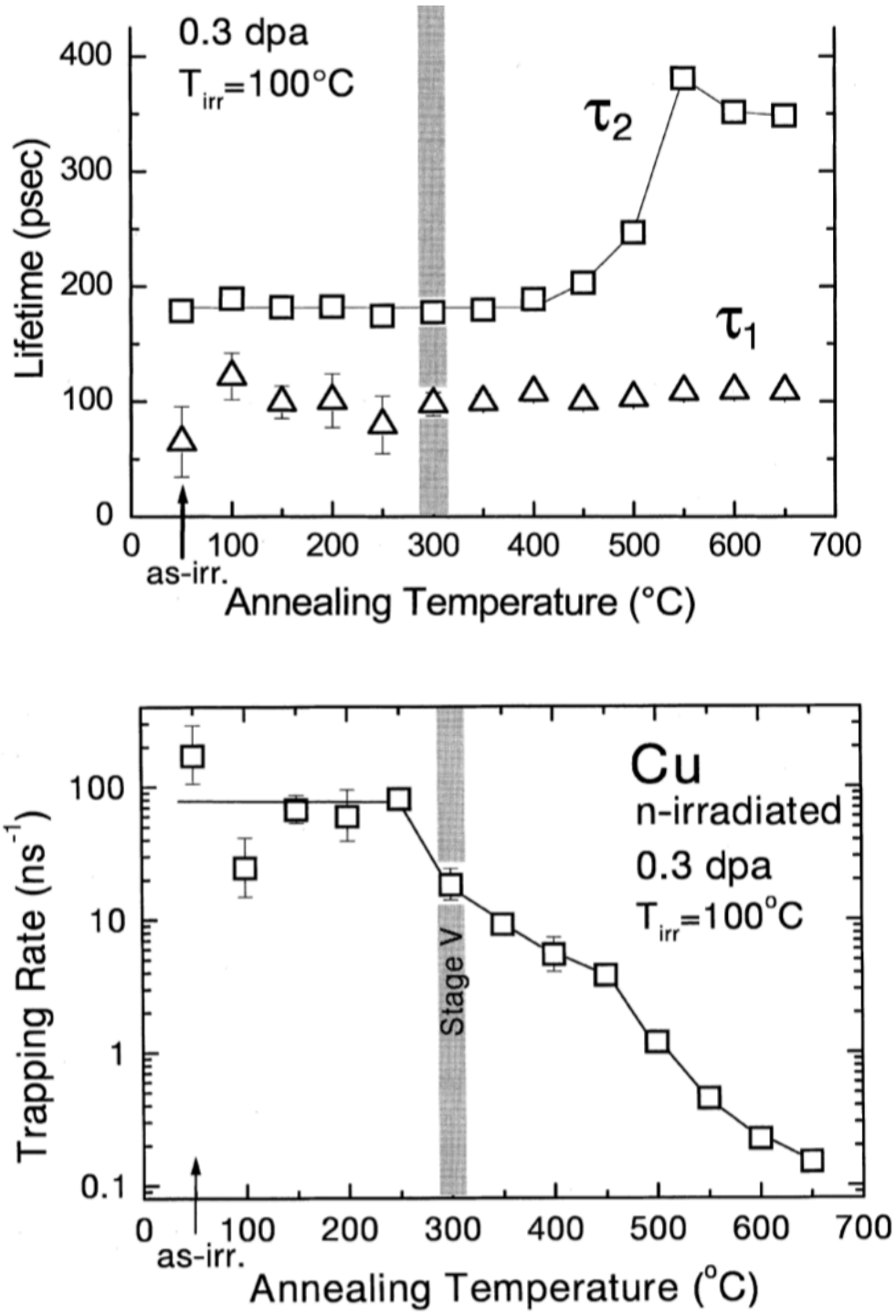

Figure 3.14 Lifetime and trapping rate evolution of neutron irradiated Cu, as reproduced from Ref [81].

He can stabilize small vacancy clusters by equilibrating the internal cavity pressure with the surface tension. During the low dose neutron irradiation experiment, a relatively small amount (< 1 appm) of He is generated by the transmutation reaction between Ni and neutrons. Due to the low He concentration, its stabilization effect will only be significant if the vacancy cluster density is relatively small. On the other hand, it is possible that a change in the local chemical environment, which is unique for HEA, may alter the binding energy of vacancies to vacancy clusters and thus change the stability of vacancy clusters. *Ab initio* modeling of vacancy energetics is needed to understand the nucleation and growth of vacancy clusters in NiFeMnCr HEA.

Utilizing the vacancy cluster size and density estimated from the PALS measurements, we can also investigate the effect of small vacancy clusters on the radiation hardening of HEA. The dispersed barrier hardening (DBH) model, which is widely used in modeling radiation hardening in typical bcc and fcc alloys, states that[77]:

$$\Delta\sigma \propto \sqrt{Nd}$$

In the equation, $\Delta\sigma$ is the change in hardness due to certain type of defects created by irradiation, N is defect density and d is the defect diameter. Based on this relationship, we can compare the isochronal annealing trend of hardness (from microhardness measurements) and that from the DBH model prediction based on vacancy cluster density and size derived from the PALS data.

Figure 3.15 shows the two thermal annealing trend lines from the hardness measurement and model prediction based on $(Nd)^{1/2}$. There is roughly a 100 ˚C difference in the annealing behavior for the microhardness data and DBH predictions derived from analysis of the PALS annealing data. Since the DBH model is mostly suitable for strong obstacles to dislocation motions[77], the moderate quantitative discrepancy between the two trend lines suggests that small vacancy clusters in the HEA (i.e., those predominantly monitored by the PALS measurements) act as relatively weak dislocation barriers. The analysis summarized in Fig. 3.15 also suggests the possible presence of an as-yet unidentified contributor to more sluggish thermal annealing of radiation-induced dislocation barriers in the NiFeMnCr HEA compared to the small vacancy clusters monitored by the PALS tests. Note that though we refer to the positron lifetime data of pure iron to assess the vacancy cluster size in the irradiated and annealed HEA alloy in this study, this should not alter the general behavior of the DBH trend line due to the small variation of positron lifetime over all annealing temperatures.

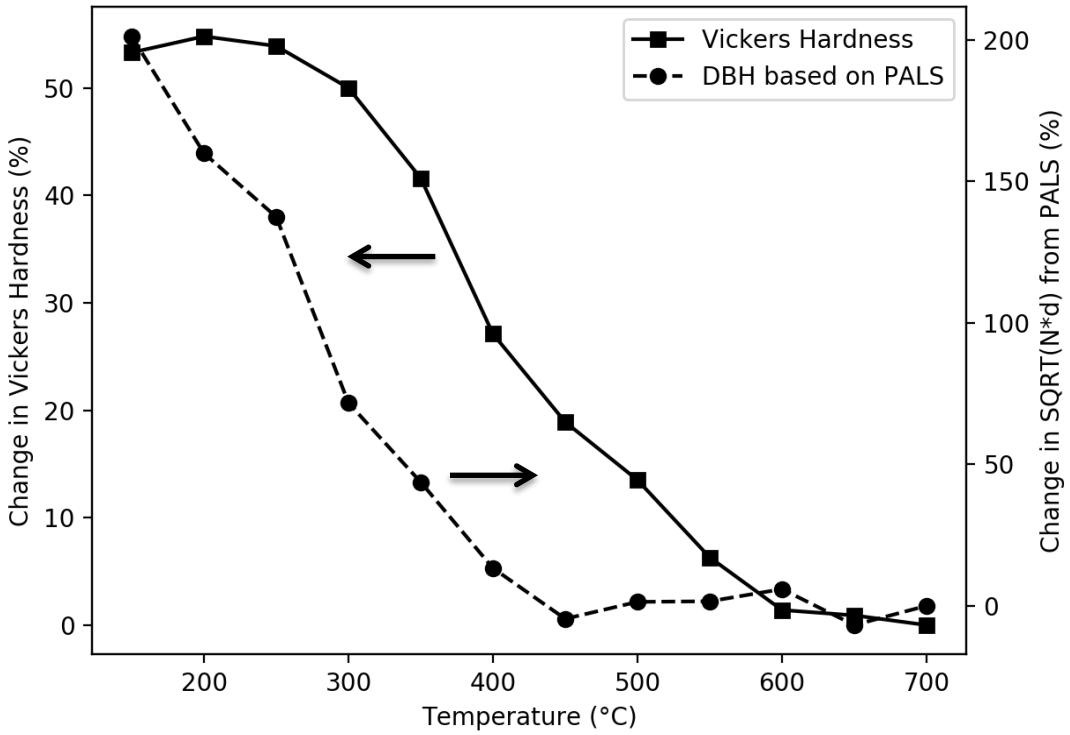

Figure 3.15 Hardness annealing trends between microhardness measurement (solid line) and DBH model based on vacancy clusters derived from PALS analysis (dashed line).

3.10.4 Preferred atomic arrangements in HEA

The neutron irradiated NiFeMnCr HEA, along with the annealing behavior of the radiation-induced microstructure and mechanical properties changes, was studied through a variety of experiments, including PAS, bulk hardness, electrical resistivity and XRD. The micro-hardness data indicated an annealing temperature of the radiation-induced hardening is 300 – 650 ˚C for NiFeMnCr HEA, which generally agrees with irradiated conventional Fe-Ni-Cr austenitic alloys where the hardness introduced by neutron irradiation at temperatures of 50 to 100 ˚C anneals at 500 to 700 ˚C[85, 110]. The PAS lifetime measurements indicate a decreasing trapping rate trend for annealing temperatures between 400 and 500°C, which is generally comparable to observations of neutron irradiated pure f.c.c. Cu after annealing from 300 – 650 ˚C[81]. Finally, similar to Fe-Ni-Cr austenitic alloys, no amorphization or second phase particles were detected by TEM or XRD after low dose, low temperature radiation or after high temperature annealing. These experimental results indicate that the HEA phase stability and defect cluster annealing behavior are qualitatively consistent with conventional alloys.

The consistency in the characteristic temperature range for phase stability and defect cluster annealing between NiFeMnCr and conventional f.c.c metals and alloys further contrast the unique annealing trend of the electrical resistivity of the NiFeMnCr HEA discussed in Section 3.10.2. Unlike Fe-Cr-Ni austenitic alloys, where a change of electrical resistivity is observed for thermal annealing between 20 – 1000K depending on the detailed irradiation condtions[94, 111], the electrical resistivity increase induced by neutron radiation in the present study shows no sign of change up to an annealing temperature of 973K. This thermally stable feature that caused a large electrical resistivity change (>10% from control sample) cannot be explained by the reduction of electron mean free path due to radiation-induced defects, second phase particles or amorphization because the maximum annealing temperature, 700˚C, is above the characteristic annealing temperature for vacancy-type defects (400 – 500˚C from PAS) and defect clusters as dislocation motion barriers (300 – 650 ˚C from microhardness), and no amorphization/second phase particles are detected as mentioned in the previous paragraph. Besides, as will be discussed in Chapter 4, though this HEA is composed of magnetic 3d elements that potentially have strong magnetic interactions, both experimental measurement and ab initio electronic structure calculations indicate that this HEA material is paramagnetic with only weak, disordered Fe moments at all temperatures. As a result, it is believed that a magnetic phase transition cannot account for the anomalously large radiation induced change in electrical resistivity. Finally, resistivity measurements before and after straining test shows that deformation up to a plastic strain of ~18% induced less than a 2% change in electrical resistivity. Thus, any mechanical deformation effects associated with using the tensile test deformed HEA sample should not significantly contribute to the observed >10% electrical resistivity increase.

Thus, it is conceivable that a change in local atomic arrangements, or SRO, may be the major contributor of the radiation induced electrical resistivity change. As discussed in Section 3.10.2, the effect of local atomic re-arrangement on electrical resistivity has been studied in a number of Fe-Cr-Ni solid solution f.c.c. alloys after neutron irradiation, electron irradiation or heat treatment[94, 100, 103-105, 111]. Depending on the physical process involved, such as clustering or local ordering/disordering, the electrical resistivity can either decrease or increase. Though the scale of change observed in Fe-Ni-Cr alloys (< 2.0 μΩ·cm) is much smaller than was measured in this NiFeMnCr HEA (17-19 μΩ·cm), increasing chemical complexity of Fe-Ni-Cr alloy does lead to larger electrical resistivity change in Fe-Ni-Cr alloys. For this HEA, the near-equimolar system significantly increases the variety of local atomic arrangements from conventional Fe-Ni-Cr alloys, and thus potentially enhances the capability of atomic re-arrangements for altering electrical resistivity. While atomic configurations in HEA were assumed to be totally random to reach maximum configuration entropy (i.e., random long range order), SRO may still exist in HEAs. In particular, for HEAs composed of multiple 3d transition metals with different preferences for magnetic spin alignment, ab initio modeling[112, 113] has found that magnetic frustration can disrupt the random arrangement of atoms and

lead to local ordering. Local ordering has also been observed experimentally in NiCoCr through X-ray scattering[114].

Preferred atomic arrangements under irradiation conditions may be related with defect properties and thus radiation effects of HEA. Since SRO determines the chemical environment near defects, characterizing SRO can be critical in understanding defect properties in HEAs. Zhao and Piochaud[115] performed a modeling study that demonstrated that the formation and migration energy of point defects in concentrated binary and ternary alloys can be strongly affected by the configuration of nearest neighboring atoms. *Ab initio* modeling work on this NiFeMnCr HEA (described in Chapter 4) demonstrates that the variation of vacancy formation and migration energy is larger than in conventional binary or ternary systems due to a larger number of possible local chemical configurations near vacancies. The structures in the above three modeling studies, however, are all constructed under the assumption of perfectly random atomic arrangements. Emergence of local ordering can change the energy landscape near defects and result in different defect energies. Knowledge of the precise SRO configuration can lead to more accurate prediction of defect formation and migration energies, which is the basis for modeling the evolution of defects and understanding radiation effect in HEAs. In addition to the formation and migration energies, the vacancy binding energy in radiation-induced vacancy clusters (dislocation loops, etc.) can also be affected by the state of SRO. As will be shown in Chapter 4, a large spread of vacancy formation and migration energy has been predicted by ab initio modeling, and thus, it is also likely that vacancy binding energy will exhibit a large spread due to the vast variety of local chemical environments. Thus, at the extremes of the binding energy statistical distribution, there may be a small number of chemical environments in this FeNiMnCr HEA that lead to unstable vacancy clusters due to low binding energy in addition to very stable vacancy clusters due to high binding energy. The small number of "chemical domains" with high vacancy binding energy might be consistent with the low number density of vacancy clusters measured by PAS after 700 ˚C annealing, as described in Section 3.10.3. Since the stability of small vacancy clusters influence the void nucleation and growth processes, the "chemical domains" with anomalously high or low vacancy binding energy may be important in understanding the suppressed void swelling of NiFeMnCr described in Chapter 2.

3.11 Conclusions

Low temperature (~60 ˚C), low dose neutron irradiation has been performed on NiFeMnCr HEA. PIE at room temperature and after isochronal annealing find out:

(1) NiFeMnCr HEA still retains fundamental stability. First, tensile test shows comparable change in strength and ductility as commercial SS after neutron irradiation up to 1dpa. Significant increase in yield strength and decrease in work hardening are observed after 0.1 and 1dpa irradiation. Large reduction of ductility is also observed, but

the alloy still >5% of uniform elongation after 1dpa irradiation. Change in hardness qualitatively matches the change in tensile strength. Second, XRD and TEM show that NiFeMnCr remains single phase after neutron irradiation up to 1dpa

(2) PIE results after isochronal annealing shows similarity with conventional f.c.c materials. First, the annealing temperature of bulk hardness is 300 – 650 ˚C for HEA and 500 – 700 ˚C for austenitic Fe-Cr-Ni alloys. Second, the annealing temperature of vacancy type of defects is 400 – 500 ˚C and 300 – 650 ˚C for f.c.c Cu. Third, stage V temperature is observed for this HEA (400 ˚C) from the evolution of PALS.
(3) On the other hand, PIE results also reveals some unique behavior in HEA different from conventional f.c.c materials. First, overall scale of change in positron lifetime after stage V temperature is much smaller than typical pure f.c.c metal. Second, large change in electrical resistivity is observed (>10 μΩ·cm for HEA in comparison with 0.2 – 4 μΩ·cm for conventional material), and the change does not anneal out up to 700 ˚C

(4) Preferred atomic arrangements may be closely related with radiation effects in NiFeMnCr HEA. Since bulk hardness and PALS showed that radiation induced defects almost all annealed out after 700 ˚C, the correlation between radiation-induced change in electrical resistivity and possible radiation-induced change in SRO can be critical in understanding radiation effects in HEA.

CHAPTER FOUR

AB INITIO MODELING OF VACANCY DEFECT ENERGETICS IN HEA

4.1 Introduction

Theoretical modeling on metals and alloys has shed light on many radiation-induced material problems, such as the RIS trend in irradiated bcc versus fcc alloys[116], formation mechanism of defect clusters[117], and effect of alloying[118] on defect production in displacement cascades. Modeling work not only helps understand experimental observations, but also to guide future experimental work. For example, the thermodynamic modeling of phase diagrams has facilitated the design of precipitation hardened Cu alloys for fusion reactors[119]. The fruitful simulation work provides huge motivation for the modeling of high entropy alloys.

However, most of the modeling advances have occurred in relatively dilute alloy systems, and there is not a well established modeling method to treat concentrated multi-component alloys. Molecular dynamics (MD)[53] and *ab initio* modeling[54] are the two most common approaches used to study defect thermodynamics and kinetics in materials. To best simulate entropy and include as many atomic configurations as possible, large-scale MD modeling of thousands of atoms, along with many different simulations, is desirable. However, since high entropy alloys are usually composed of 4 or more elements, the formulation of many-body potentials can be much more complex than in dilute binary and ternary alloy. Describing atomic interactions in HEA by conventional formulation of empirical potential for dilute alloys can be highly risky and may lead to wrong physics, such as defect cluster configuration[109]. On the other hand, while *ab initio* modeling does not need to make such approximations, there are other limitations inherent to the DFT approach.

There are generally two distinctive pathways to incorporate chemical disordering into *ab initio* calculations: direct computation of configurationally averaged single site properties, or producing a multi-site supercell and computing properties from the site averages. The former method is based on coherent potential approximation (CPA), which is an effective medium theory within the context of density functional theory (DFT). The key notion of the theory is to replace the calculation of the real disordered system with an equivalent, ordered system that is selected to have the configurationally averaged properties of the real system. Because the implementation is closely related to the Korringa-Kohn-Rostoker (KKR) band structure method[120-122], it is commonly referred to as KKR-CPA. However, it is challenging for the implementation to consider lattice displacement or local structural distortion, which are believed to be crucial for defect

properties in HEA. The latter method uses standard DFT electronic codes to compute large supercells with minimized short-range order based on special quasi-random structures[123, 124]. Structural relaxation is allowed, but to include sufficient chemical disordering, a huge supercell of hundreds of atoms is needed and it can be computationally demanding. As a result the typical applications are limited to <250 atoms and more typically less than 100 atoms, which then requires care in the interpretation of results.

Beyond issues of properly accounting for semi-empirical potential formulation and configurational averaging, some additional basic condensed matter concepts in metals and conventional dilute alloys do not apply to the study of a concentrated multicomponent alloy[125]. In conventional dilute alloy systems and pure metals, there is essentially a single vacancy formation energy. However, in HEA numerous local atomic arrangements produce many different local environmental configurations around defects. Thus the vacancy formation energy can no longer be described by several discrete values, but instead encompasses a statistical distribution. Similar statistical analysis also applies for vacancy migration, interstitial formation and other defect energetic thermodynamic and kinetic properties in a HEA. Thus, a considerable amount of computational time is needed just to sample a relatively straightforward defect system such as calculating the vacancy formation energy. Recent *ab initio* work on concentrated binary and ternary alloy confirms that there is a non-negligible spread of defect formation and migration energy[54, 115] in concentrated alloys, and the values can depend on the chemical identity of the defect as well as the local environment around the defect. For HEA containing more components, defect energetics can be even more complex.

Finally, there is a unique challenge for the NiFeMnCr HEA, namely magnetic frustration. All four constituents in this particular HEA are 3d elements in the periodic table and exhibit magnetic behavior. The spin-coupling behavior of these four elements is also different; Fe and Ni prefer a ferromagnetic (FM) alignment, Cr prefers anti-ferromagnetic (AFM) alignment, and Mn exhibits a very complex magnetic structure in its stable elemental phase[126] and cannot be simply described by either FM or AFM. A random, near-equimolar mix of these four species can make it hard for the electrons associated with some atoms to find a stable spin orientation which results in local magnetic frustration. A previous *ab initio* study on a Ni-Fe-Cr-Co HEA system indicated that magnetic interactions could potentially affect the chemical disordering of the alloy[112, 113]. Since Mn exhibits much more complex magnetic behavior than Co, replacing the Co in such HEAs for nuclear applications will likely magnify the effect of magnetic interactions, and its impact on defect physics needs to be carefully treated.

In this study, the respective strength of CPA- and supercell-based *ab initio* methods are combined within an initial computational modeling study to tackle the theoretical defect physics grand challenges presented above. While CPA is used to compute configurational-averaged magnetic properties below and above the magnetic ordering temperature, the supercell method is used to investigate local moment changes. Large

supercells are created and optimized to incorporate sufficient chemical disorder. For computing vacancy energetics, many vacancy sites and migration pathways are sampled in an attempt to obtain sufficient statistics for studying the correlation between chemical disordering and defects.

4.2 Modeling Methods

All supercell calculations were performed using the Vienna *Ab initio* Simulation Package (VASP)[127]. Potentials based on projector augmented wave (PAW) method[128] and GGA-PBE[129] functionals were used, with 3p electrons also included as valence electrons in order to ensure proper treatment of this novel multicomponent system. While the energy cutoff was fixed at 400 eV for all calculations, the k-point mesh was varied depending on supercell size and desired computational accuracy. The calculation stopped when the total free energy change is smaller than 10^{-6} eV and all forces between atoms were smaller than 0.01eV/ Å.

The KKR-CPA calculation was implemented using the same exchange-correlation functional. To investigate the magnetic behavior of the alloy at finite temperature, a parallel tempering Monte Carlo algorithm[130] based on the Heisenberg model was used. In the classic Heisenberg model, the Hamiltonian of the magnetic system is described by:

$$\widehat{H} = -\sum_{i \neq j} J_{ij} S_i \cdot S_j \ , \qquad \text{(Eq. 4.1)}$$

where S_i and S_j represent the spin of the interacting atoms, J_{ij} is the effective Heisenberg exchange interaction coefficient between i and j, and can be obtained from *ab initio* electronic structure calculation. Thus, the partition function of the magnetic system can be defined:

$$Z = \sum e^{-\beta \widehat{H}} , \quad \beta = \frac{1}{k_b T} , \qquad \text{(Eq. 4.2)}$$

where k_b is the Boltzmann constant and T is the temperature. Thermodynamic properties, including magnetic susceptibility, can then be computed if the partition function can be properly evaluated. In this study, KKR-CPA was used to compute the necessary exchange interactions of the effective Heisenberg model, and Monte Carlo methods were used sample the partition function and calculate magnetic susceptibility.

Magnetic behavior was also measured experimentally for comparison. The magnetic measurements were performed using a commercial SQUID magnetometer from Quantum Design. The temperature dependent magnetic susceptibility measurements were performed using the field-cooled protocol, with the magnetic field applied at 300 K and the data taken on cooling. For the magnetization curves at 300 and 5 K, the maximum magnetic field (50 kOe) was applied first and the magnetization recorded as the magnetic field was reduced to 0.

Chemical disorder in the supercell was simulated by minimizing the correlation function between first-nearest neighbors (1nn). In other words, the atomic configuration in a truly

random HEA should not favor any type of nearest neighboring pairs. There should be equal number of X-X pairs (Cr-Cr, Mn-Mn, Fe-Fe, Ni-Ni) and X-Y pairs (Cr-Mn, Cr-Fe, Cr-Ni, Mn-Fe, Mn-Ni, Fe-Ni). The special quasi-random structure algorithm[124] provided by Alloy Theoretical Atomic Toolkit (ATAT) was utilized to perform this minimization. 32-atom and 108-atom supercells were generated to explore variation in local moments, while a 256-atom supercell was generated to compute chemical potential, vacancy formation and migration energies.

The vacancy formation energy was computed as follows:

$$E_v^f = -E_0 + E_D + \mu_X, \quad \text{(Eq. 4.3)}$$

where E_0 is the energy of the perfect supercell, E_D is the supercell energy with vacancy defect and μ_X is the chemical potential of the removed atom. While both the supercell volume and atomic coordinates were relaxed for the perfect supercell, only the atomic coordinates were relaxed for a supercell containing a vacancy. Since the chemical potential of a species is defined as the change of total free energy per atom of that species, this value is highly dependent upon the metallic bonding around that species. Therefore, chemical potentials of Cr, Mn, Fe and Ni in concentrated multicomponent alloy are expected to be very different from those in their pure reference state, and need to be calculated directly.

The classical Widom type substitution[131] technique was applied in previous *ab initio* simulation work on binary[54] and ternary[115, 132] concentrated alloys. The technique is based on calculation of substitution energy associated with switching one element to another on an atomic site. The substitution energy represents the chemical potential difference between the elements involved. In the four-component system, there will be three sets of substitution energies and the chemical potential at this particular atomic site can be solved. For example, for a Cr atom at site i, there will be:

$$\mu_{Cr}^i - \mu_{Mn}^i = \Delta E_{Cr\to Mn}, \quad \text{(Eq. 4.4a)}$$

$$\mu_{Cr}^i - \mu_{Fe}^i = \Delta E_{Cr\to Fe}, \quad \text{(Eq. 4.4b)}$$

$$\mu_{Cr}^i - \mu_{Ni}^i = \Delta E_{Cr\to Ni}. \quad \text{(Eq. 4.4c)}$$

As well, the total energy of the supercell is:

$$64\left(\mu_{Cr}^i + \mu_{Mn}^i + \mu_{Fe}^i + \mu_{Ni}^i\right) = E_{256}, \quad \text{(Eq. 4.4d)}$$

where, $\Delta E_{X\to Y}$ is the substitutional energy from element X to Y, E_{256} is the free energy of the 256-atom supercell and μ_X^i is the chemical potential of element X evaluated at atomic site i. Substitutional energies and free energy of the supercell can all be obtained from standard DFT calculation, so the chemical potential at site i for each element can be solved.

A thorough implementation of the Widom technique needs to consider every unique atomic site and compute the canonical average. On the other hand, there are too many possible atomic configurations, resulting in an enormous number of atomic sites to sample even for the simpler binary and ternary concentrated alloys. For practical application of the technique, representative atomic sites were selected as an

approximation in previous work for binary and ternary alloy system[54, 115]. A similar strategy was applied for the four-component system in this study.

Some simplifications and notations need to be introduced for the discussion of local chemical environment in this paper. First, the local chemical environment is simplified to describe just the twelve first nearest neighbor sites since immediate neighbors usually impose the strongest influence to any atom in the fcc structure. Second, we only focus on the number of neighboring atoms, but neglect the effect of atomic arrangements. Under this assumption, for a local environment composed of 3 atoms of each type, we regard all different kinds of atomic arrangements of these 12 atoms as being an essentially equivalent local environment. Third, a new notation is introduced to simplify the expression for the composition of the local environment. The notation involves writing the number of each species in the sequence of Cr, Mn, Fe and Ni. For example, 3 atoms of each species is written as (3,3,3,3), while 7 Cr, 2 Mn, 2 Fe and 1 Ni is written as (7,2,2,1). (3,3,3,3) is called "uniform" local environment, while all other composition are referred to as a "biased" environment.

The vacancy migration barrier was computed by the climbing-image nudged elastic band (NEB) method[133]. In this method, several images are interpolated between the starting and ending configuration of the vacancy. The atomic configuration of each image is optimized and the migration pathway is then approximated by connecting all intermediate images. NEB calculation stopped when the force on each image is smaller than 0.02eV/Å.

4.3 Bulk Material and HEA

The physical properties of the four elements of our HEA in their pure forms were first computed. For each metal, the most stable phase at ambient temperature and pressure was chosen; Fe is FM bcc phase, Ni is FM fcc phase, Cr is AFM bcc phase, and Mn is a paramagnetic cubic structure containing 58 atoms. An 8 8 8 gamma centered k-point mesh was used, which resulted in a calculational error smaller than 1meV/atom for total free energy. The computed lattice constants and formation enthalpy are listed in Table 4.1, and agree well with other published values.

Table 4.1 Lattice constants and formation enthalpies of pure metals, calculated in this work compared with literature and experimental references.

	Fe	Ni	Cr	Mn
Lattice constant (Å)	2.848	3.529	2.875	8.580
Literature (Å)	2.833[134], 2.85[135]	3.518[134]	2.849[136]	8.532[126]
Experimental (Å)	2.8665[137]	3.524[137]	2.8848[137]	8.865[138]
Formation enthalpy (eV/atom)	-8.46	-5.79	-9.64	-9.15

Supercells comprising 32, 108 and 256 atoms were then generated for the FeNiMnCr HEA. Rather than the low-Cr, near equimolar composition of the real alloy, each atomic species had the same number of atoms to simplify the initialization of the supercell. Atomic configurations were then optimized to obtain a non-biased nearest pair distribution. Table 4.2 shows the number of each type of first nearest pairs after optimization following the ATAT procedure[124]. The 32-atom supercell has a perfectly uniform pair distribution. For the larger 108- and 256-atom supercells, 1~2 atomic pairs require modification, but both structures have a fairly uniform pair distribution.

One key approximation in the supercell setup is to model the near-equimolar quaternary system as having an exact equimolar composition. To examine the error related with this approximation, the density of states, band structure and magnetic state for both equimolar and the real composition of the quaternary system were computed by KKR-CPA. The experimentally determined lattice parameter was used as the input for the KKR-CPA implementation.

Figure 4.1 shows the KKR-CPA density of states (DoS) and Bloch spectral functions (BSF), which is the equivalent of the band structure for disordered system. For the DoS, contributions from spin-up (green) and spin-down (blue) electrons were plotted separately on the left. The BSF plots are for the major high symmetry directions in the Brillouin zone. Different from the well-defined band structure in ordered system like pure Ni, the band structure of NiFeMnCr HEA is highly smeared out, in energy and wave-vector, throughout the full d-band between -2 to 2eV This observation is consistent with KKR-CPA calculation results of HEAs of similar chemical compositions, such as NiCoFeCr, NiCoCr and NiFeCo performed by Zhang and co-workers[139]. Smearing in the band structure is related to the electron mean free path: No smearing in band structure lead to infinite electron mean free path, while smearing of bands lead to shorter mean free path. Note that little difference can be observed between the DoS and BSF computed for the two different alloy compositions, indicating the electronic structures are very similar. The results shown in Figure 4.1 thus justify our assumption to use an equiatomic composition for modeling this NiFeMnCr HEA.

The component-wise and total magnetic moments were also computed based on KKR-CPA electronic structures. Both the total magnetic moments and component-wise magnetic moments are very close for the NiFeMnCr at two different compositions, as shown in Table 4.3. Thus, electronic structure calculations by KKR-CPA provide strong indications that the composition approximation should not lead to loss of essential physics.

Table 4.2 First nearest neighbor pair distributions in the three different supercell sizes after ATAT optimization.

	Cr-Cr	Mn-Mn	Fe-Fe	Ni-Ni	Cr-Mn	Cr-Fe	Cr-Ni	Mn-Fe	Mn-Ni	Fe-Ni
32-atom	12	12	12	12	24	24	24	24	24	24
108-atom	41	40	40	41	81	81	80	82	81	81
256-atom	95	95	94	96	192	194	192	194	192	192

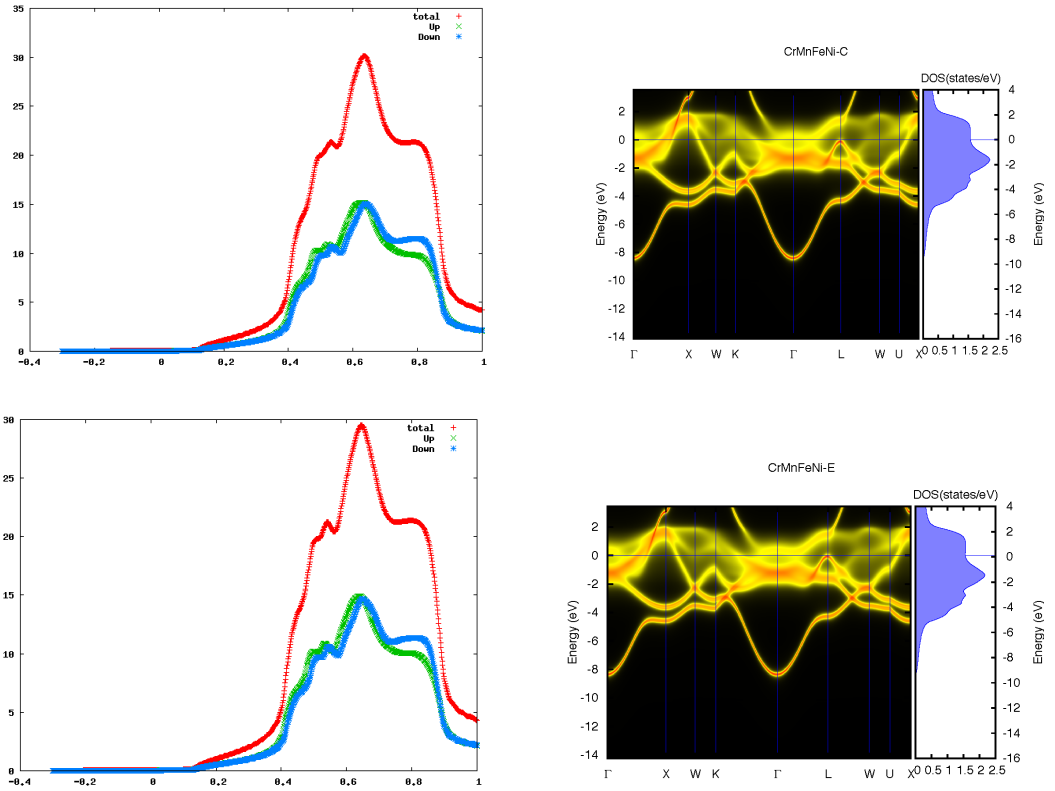

Figure 4.1 Density of states (left) and Bloch spectral functions (right) of CrMnFeNi in actual (top) and equimolar (bottom) compositions.

Table 4.3 Component-wise and total magnetic moments from KKR-CPA for FeNiMnCr at two compositions (with a unit of Bohr magneton).

	Equimolar	Real
Total	0.188	0.194
Cr	-0.12	-0.10
Mn	-0.73	-1.00
Fe	1.54	1.69
Ni	0.07	0.09

4.4 Exploratory study of magnetic frustration at zero temperature

To explore the effect of magnetic frustration, a single vacancy was introduced in the 32-atom and 108-atom supercell by removing one atom. For supercells of both sizes, the experimental lattice parameter was used to initialize the starting volume, and both volume and internal coordinates were relaxed for the perfect supercell. After the vacancy was created, only the internal atomic coordinates were relaxed within the supercell, but not the volume. The 32-atom supercell used a 3 3 3 k-point mesh, while the 108-atom used a 2 2 2 k-point mesh. Both k-point meshes were gamma centered. Component-wise magnetic moments from KKR-CPA were used to initialize the moments in collinear spin-polarized VASP supercell calculation. In addition to the reference state provided by KKR-CPA, additional magnetic spin configurations were used to test the magnetic stability of the reference state.

Supercell modeling results confirmed the existence of magnetic frustration in NiFeCrMn HEA. First, different magnetic initializations can converge to different magnetic states, suggesting that the magnetic moments of some atoms in the supercell are unstable. Second, the magnetic instability significantly affects the local and total magnetic structure, but also the enthalpy of the supercell. Tables 4.4 and 4.5 provide the enthalpy and total magnetic moment calculated for a Ni vacancy introduced in either a 32-atom or 108-atom supercell, respectively. For the 32-atom case, "Mn AF" stands for initializing anti-ferromagnetic Mn spins, while "Mn F" stands for ferromagnetic Mn spins. These two schemes revealed two completely different states, with an energy difference of 0.4 eV and a total moment difference of 9 μ_b.

In the 108-atom supercell, "Mag1" stands for an initialization of the orientation (up/down) of the Ni, Fe, Cr, Mn moments according to the configurationally averaged moment obtained from the KKR-CPA calculation, while "Mag2" randomly switches half of the spins of Mn atoms' from up to down, relative to the "Mag1" initialization. The calculated results from the two schemes show very little difference in total moment, but indicate a 0.3 eV difference in total enthalpy. A closer look at the component-wise moments indicates that the spins of many Cr and Mn atoms and some Fe atoms have flipped spins or changed greatly in magnitude. Note that the 32-atom and 108-atom results presented in Tables 4.4 and 4.5 are just two of many vacancy calculations. Similar moment and energy instabilities also exist for a vacancy formed by other Ni atoms as well as the other atomic species.

Table 4.4 Enthalpy and magnetic moments of 32-atom supercell with a Ni-vacancy.

	Enthalpy (eV)	Total moment (μ_b)
Mn AF	-253.40	1.15
Mn F	-253.83	10.67

Table 4.5 Enthalpy and magnetic moments of 108-atom supercell with a Ni-vacancy.

	Enthalpy (eV)	Total moment (μ_b)
Mag1	-874.45	21.3
Mag2	-874.74	22.3

Several implications can be drawn from these supercell calculations of magnetic structures. First, differences in spin ordering can cause an enthalpy difference as large as 0.4 eV/cell and 0.01eV/atom. Thus, obtaining a reliable magnetic state is the prerequisite to obtaining reliable energy-related properties, such as defect formation energies for NiFeMnCr system. Second, there is not a straightforward magnetic reference state for each element within a given configuration. Each atom has a unique magnetic ordering preference depending on its local atomic configuration, and it is extremely challenging to find this "unique preference" for all types of possible configurations. Third, only this "unique" magnetic moment arrangement generates the appropriate ground state corresponding to the global minimum of the potential landscape of the NiFeMnCr material system. All other moment arrangements only reflect other local minima of the potential landscape and their corresponding energies are not useful for the determination of vacancy energetics.

Thus, sampling even one vacancy for the NiFeMnCr supercell has the potential to require massive computational resources. This requirement is further exacerbated by the large number of alloy configurations required to account for the statistics of the vacancy formation energies corresponding to the various local chemical environments. Consequently, modeling the effect of chemical disorder on defect properties at near zero Kelvin can be extremely challenging due to the presence of severe magnetic frustration. On the other hand, magnetic structure is strongly dependent upon temperature for 3d transition metals and their alloys. Magnetic spin interactions may not be as pronounced at elevated temperature, especially above the Curie temperature where spins become highly disordered. Thus, investigating the temperature dependence of magnetic frustration in this HEA can provide insights on the significance of magnetic interactions at temperatures relevant for actual nuclear power application, and assess whether paramagnetic calculations can avoid the challenge from severe magnetic frustration and solely focus on chemical disordering in HEA.

4.5 Magnetic frustration at finite temperature

Figure 4.2 shows the component-wise exchange interaction energies (J_{ij}) as a function of interaction distance, as computed by KKR-CPA. The red dashed line in each plot is an exponential decay curve to show the rapid decrease of the exchange interaction energy with respect to the interaction distance. Absolute magnitude of the energy indicates the strength of exchange interaction energy, and the sign of energy indicates the preferred

coupling between the spins. Positive means ferromagnetic coupling while negative means antiferromagnetic coupling. Several implications can be drawn from these calculations. First, the plots show that for all interaction pairs, the strength of interaction decays rapidly and suggests that magnetic frustration should be dependent upon the local chemical environment. Second, the signs of exchange interactions of almost all atomic pairs show oscillating behavior with increasing interaction distance. This indicates that the spins in NiFeMnCr system are highly disordered and simple collinear spin coupling may not be able to describe the ground state magnetic structure. In particular, many of the first nearest neighbor atomic pairs (the first interaction coefficient at ~2 Angstrom) prefer antiferromagnetic coupling. For f.c.c materials at (111) planes, this could lead to strong magnetic frustration and non-collinear spin configurations.

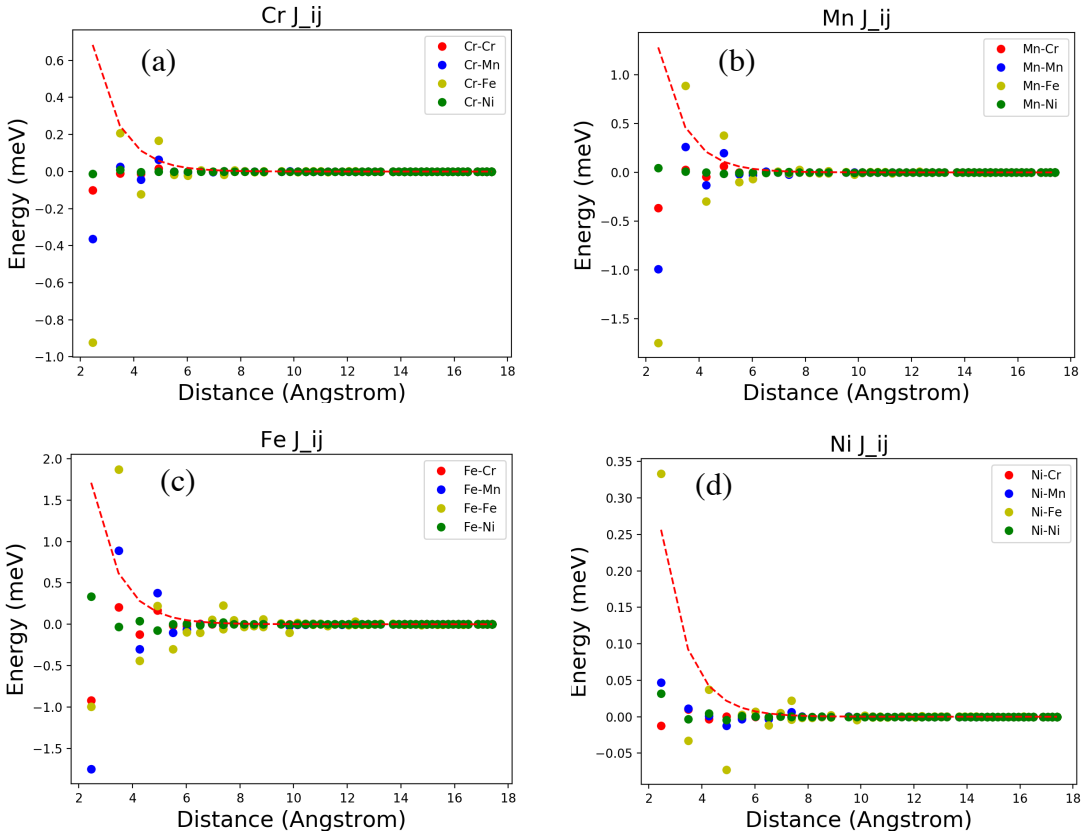

Figure 4.2 Exchange interaction coefficient for (a) Cr, (b) Mn, (c) Fe and (d) Ni as a function of interaction distance. The red dashed line is an exponential decay curve to show the decreasing trend of the exchange interaction with respect to distance. Note that the scale of y-axis is different for the four elements.

Based on the above interaction coefficients, a Monte Carlo simulation was performed to investigate the magnetic susceptibility as a function of temperature, and the results are plotted in Figure 4.3. Figure 4.4 shows the corresponding experimentally measured magnetic susceptibility of a NiFeMnCr HEA for comparison. The Monte Carlo simulation result shown in Fig. 4.3 was also fit to the Curie-Weiss Law to determine the Curie temperature for the NiFeMnCr HEA:

$$\chi = \frac{C}{T - T_c}, \quad \text{(Eq. 4.5)}$$

where χ is the magnetic susceptibility, C is the Curie constant and T_c is Curie temperature. In the classical Heisenberg model, where magnetization M is a unit-less quantity, the susceptibility with units meV^{-1} is defined by:

$$\chi = \frac{<M^2> - <M>^2}{kT}, \quad \text{(Eq. 4.6)}$$

where T is temperature and k is the Boltzmann constant. On the other hand, in experimental measurements, χ has historic units $cm^3\ mol^{-1}$ because magnetization involves a certain measure of magnetism per unit volume. Due to the difference in the definition and units of susceptibility in Monte Carlo modeling and experimental measurement, the absolute values in the results are not comparable between model and experiments, but only the relative scale of change is comparable.

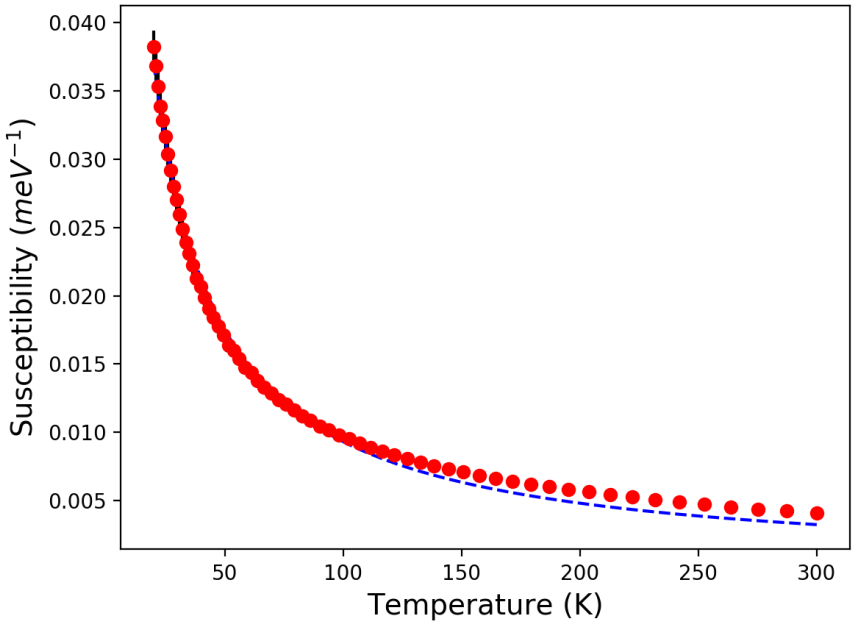

Figure 4.3 Monte Carlo simulation of the magnetic susceptibility as a function of temperature. The blue dash line is the corresponding Curie-Weiss Law fit to the simulation results, which indicates a Curie Temperature less than zero Kelvin.

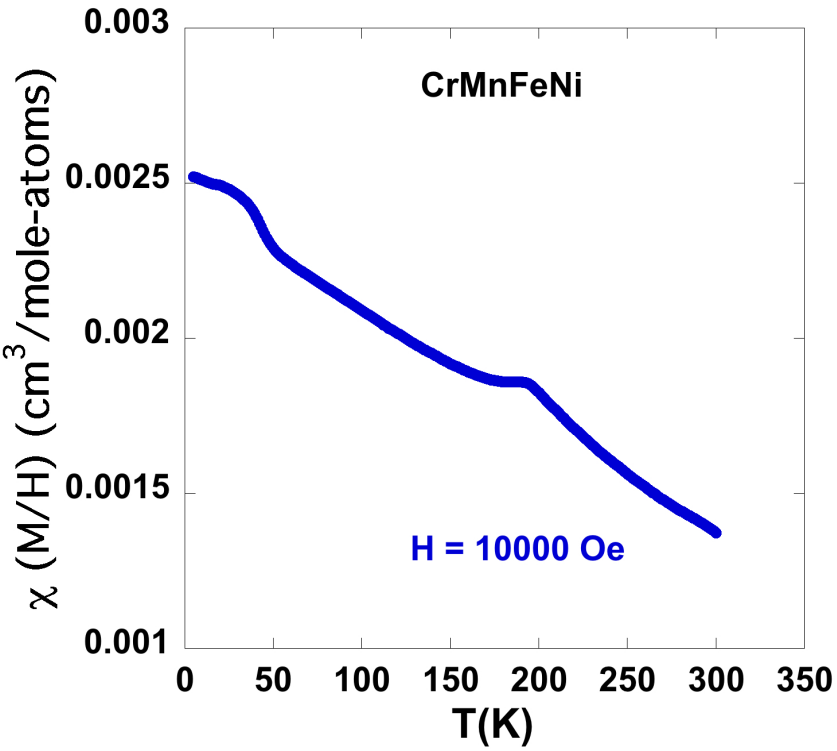

Figure 4.4 Experimentally measured magnetic susceptibility of NiFeMnCr HEA as a function of temperature with an applied external magnetic field of 10 kOe.

Experimental measurement shows that the magnetic susceptibility of this material generally decreases as temperature increases. Changes in the decreasing trend at 50K and 200K suggest complex magnetic behavior occurs at low temperature, but no magnetic phase transition temperature was observed over the entirety of the measured temperature range. Similarly, a Curie Weiss law fit of the Monte Carlo simulation results showed that the Curie temperature of this material is -7K, indicating no magnetic phase transition temperature. This indicates that at finite temperature, magnetic spins in the NiFeMnCr HEA system will be highly disordered and behave like a paramagnetic material.

On the other hand, a paramagnetic material can still have "local" moments despite near zero "overall" moment. One classical example is the comparison between Fe and Ni. Above the Curie temperature, both metals change from ferromagnetic to paramagnetic. While the Ni magnetic moment vanishes toward zero, the magnitude of the individual Fe moment is relatively unchanged. Rather, in Fe, the total moment is zero because the orientations of Fe moments are disordered, resulting in a zero vector sum[140, 141]. These disordered moments can potentially contribute to magnetic frustration locally, and produce the type of magnetic instability near defects that was observed in the supercell modeling results described in the previous section.

To further investigate the local magnetic structure above the magnetic disordering temperature, the disorder local moment (DLM) was implemented within KKR-CPA framework. DLM is a theory of the finite temperature paramagnetic state that is generally valid in systems that have robust moments like Fe[140]. Disordered moments are imposed by separating atoms of the same element into two groups. The moments in each group are given the same magnitude but opposite spins. Thus, for each element, the total moment will cancel out and approach zero as in a paramagnetic system. The component-wise magnetic moment calculated by KKR-CPA at zero Kelvin (Table 2) was used to initialize the spin configurations. Our KKR-CPA DLM calculations indicate that the Cr and Mn moments decrease to $10^{-5}\ \mu_b$, and the Ni moment decreases to $10^{-6}\ \mu_b$. Only Fe still has a sizable moment of $1.1\mu_b$. Additionally, we have calculated the exchange interaction energies predicted by the KKR-CPA DLM model in the same fashion as previously (Fig. 2), and these DLM predictions are shown in Figure 4.5. Since only Fe has a sizable moment, only the two groups associated with Fe atoms ("Fe_up and Fe_dn") show sizable interaction coefficients. All other exchange interaction energies decrease to near zero values. In addition to the rapid decrease of exchange interaction energy with increasing distance, these Fe pairs also shows oscillating preference of spin coupling and anti-ferromagnetic coupling for the first nearest neighbor. Thus, the DLM shows that for the surviving Fe moments, spins are highly disordered and frustrated.

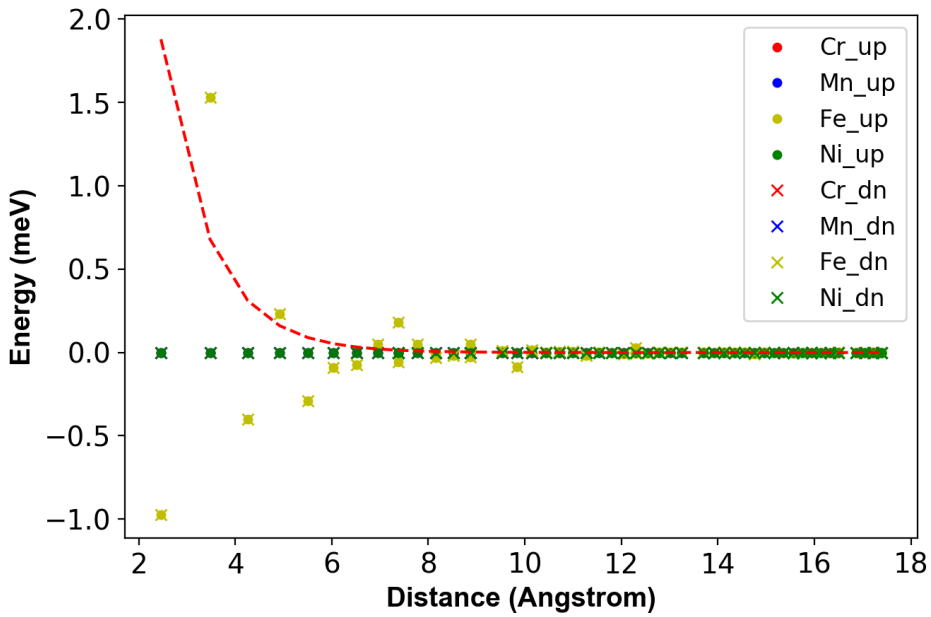

Figure 4.5 Exchange interaction energy for the four elements based on DLM theory. The red dash line is an exponential decay guideline to show the decreasing trend of magnetic interaction strength.

In summary, both modeling and experimental measurements of the magnetic behavior of NiFeCrMn conclusively indicate that the effect of magnetic frustration at elevated temperature is much less significant than that at zero Kelvin. While the NiFeMnCr alloy is not perfectly non-magnetic due to the existence of disordered Fe moments, it is evidently a very dilute magnetic system and the Fe magnetic moments in the NiFeMnCr alloy are much smaller than those in pure Fe above Curie temperature. We expect that the vanishing nature of the disordered Cr, Mn and Ni moments can greatly reduce the uncertainty of ground state energy caused by magnetic frustration. Thus, at temperatures of interest for nuclear energy systems, magnetic disorder should be less important then chemical disorder for determining thermodynamic properties, such as defect energetics, in the NiFeCrMn HEA. Thus in the following analysis to calculate the chemical potential and defect energetics, we have used a 256-atom supercell-based DFT simulations without spin polarization, thereby focusing exclusively on the impact of chemical disorder on defect properties.

4.6 Chemical Potentials in multicomponent concentrated alloy

Before computation of the chemical potential, a rigorous error analysis on k-point meshing was conducted to achieve the best combination of computational efficiency and accuracy. Gamma centered 4 4 4, 2 2 2 and single k-point meshing was applied for the perfect supercell. Both volume and atomic displacements were relaxed for the 4 4 4 case. For 2 2 2 and single k-point scenarios, the volume is fixed at the equilibrium volume obtained from the 4 4 4 k-point calculation and only the atomic displacements (internal coordinates) are relaxed. Results are shown in Table 4.6:

Based on the 1meV/atom error margin for typical electronic structure calculation, using 2 2 2 k-point meshing is deemed to be reasonable. However, 2 2 2 k-point meshing required more CPUs for parallelization and needed more computation time than the single point calculation. Also, the actual physical property we are interested in is vacancy energetics, not the total energy of the supercell.

Table 4.6 256-atom supercell ground state energy with different k-point meshing.

	Ground state energy (eV)	Energy difference to 4 4 4 k-point (meV/atom)
4 4 4 k-point	-2085.21	
2 2 2 k-point	-2085.40	0.82
Single k-point	-2086.13	3.6

Further analysis was directly conducted on two vacancy samples (one Cr, one Mn) to examine the difference between single k-point and 2 2 2 k-point meshing. Results are shown in Table 4.7. Similar to 256-atom supercell, the ground state energy of 255-atom supercell with a vacancy shows a large difference between the two k-point schemes. However, most of the error cancelled when taking the difference of 255-atom and 256-atom supercell energy. The resulting vacancy formation only shows a 0.1eV error, which is typical for *ab initio* calculation of defect energetics. Thus, single k-point scheme is chosen to achieve a combination of faster data acquisition rate and reasonable computation accuracy.

For the chemical potential calculation, atomic configurations in which each atom/element has a uniform environment were chosen as representative because this provides a local composition closest to the actual HEA. Out of the 256 atoms in the supercell arrangement, one Cr, one Mn, one Fe and three Ni atoms have uniform local environment. Six sets of chemical potentials were calculated from these sites, and are presented in Table 4.8 in terms of both the average and standard deviation, in comparison with chemical potential of these elements in pure substance reference.

The standard deviation of the chemical potential of each element is much smaller than 0.1 eV, which is the within the convergence error for *ab initio* defect calculations. This indicates that the average chemical potential is appropriate for computing defect energetics. Also, the small standard deviation indicates a relatively small spread of the calculated data, suggesting all six atomic sites are indeed representative of similar

Table 4.7 255-atom supercell ground state energy and vacancy formation energy from two different k-point scheme.

Cr vacancy sample		
	Ground state energy (eV)	Vacancy formation energy (eV)
2 2 2 k-point	-2074.14	1.62
Single k-point	-2074.97	1.52
Mn vacancy sample		
	Ground state energy (eV)	Vacancy formation energy (eV)
2 2 2 k-point	-2075.20	2.05
Single k-point	-2075.01	1.97

Table 4.8 Chemical potentials of the four elements in HEA and in pure substance.

	CrMnFeNi HEA (eV)	Pure substance (eV)
Cr	-9.39 ± 0.04	-9.64
Mn	-9.07 ± 0.01	-9.15
Fe	-8.34 ± 0.02	-8.46
Ni	-5.79 ± 0.04	-5.79

uniform chemical environments. This also justifies the previous assumption that chemical potentials are dominated by first nearest neighbor interactions. Since the definition of local chemical environment in this study does not consider the geometric configuration of the first nearest neighbors, it also appears that total number of specific elemental nearest neighbors is more important than the geometric configuration of the atoms for determining the chemical potential of species within the HEA. Finally, comparing with the pure substance values, only the Ni chemical potential is nearly the same in the HEA as in elemental form, while all other chemical potentials have higher values in the HEA.

To verify the hypothesis that chemical potential based on sites of "uniform" environment can approximate the ensemble average of all other possible sites, chemical potentials of a randomly chosen population of "biased" 1nn compositions, such as (7,1,2,2), (2,4,6,0) and (1,7,1,3), were calculated. Figure 4.6 shows the comparison of these results with those obtained using only "uniform" environment substitutions. As more samples from "biased" 1nn compositions are considered, the difference between the chemical potential values decreases. The convergence rate is rapid and the difference becomes less than 0.1 eV for elements when 6 or more sites of the deviated group are included. The fast convergence of "biased" chemical potential values relative to the "uniform" chemical potential provides strong evidence that it is valid to use chemical potential based on such a "uniform" group when calculating vacancy formation and migration energies, and provides a means for bounding the anticipated error or statistical spread in the vacancy formation energy. It is worth pointing out that this method provides a computationally efficient and physically reasonable pathway to approximate the chemical potential of multi-component concentrated alloys by sampling at several atomic sites with representative local atomic compositions.

4.7 Vacancy formation energy

To investigate the effect of chemical disorder on vacancy formation energy, a more detailed grouping of the local chemical environment needs to be introduced in this section. We first define an "operation" as starting from the uniform environment of (3,3,3,3), with subsequent switching of one kind of atom by another. For example, one "operation" could involve switching from (3,3,3,3) to (2,4,3,3), and two "operations" could involve switching from (3,3,3,3) to (1,5,3,3). As more "operations" are performed, the environment moves further away from the "uniform" environment. Based on this definition, a deviated group can be further divided into smaller groups: compositions generated by one operation, such as (2,4,3,3) and (2,3,4,4), are called group "Op1". Compositions generated by two operations, such as (1,5,3,3), (2,5,2,3), are called "Op2"… and so on. Finally, uniform composition is called "Op0".

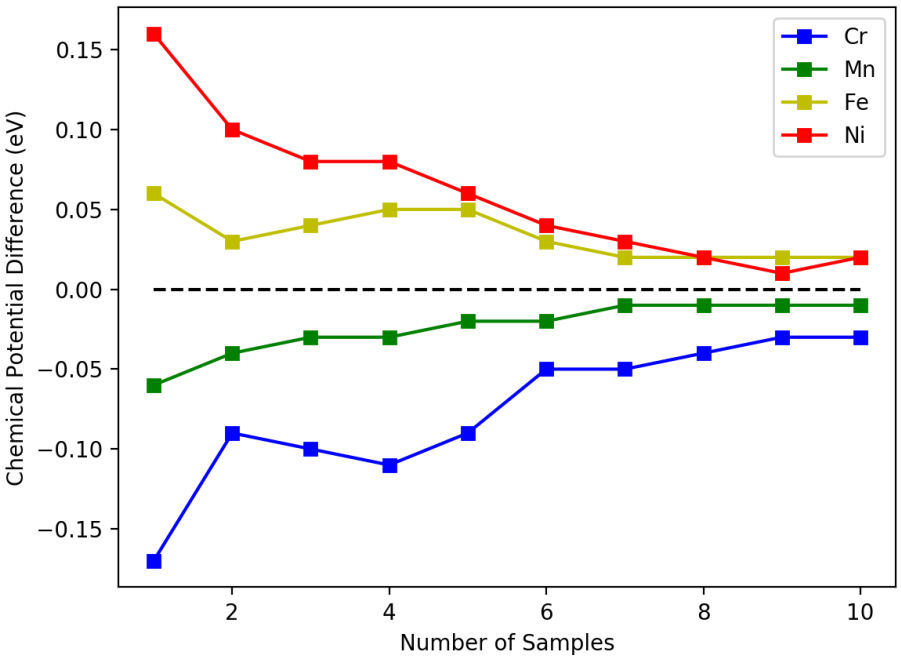

Figure 4.6 Chemical potential difference computed from uniform and "biased" local environment with respect to number of samples from "biased" composition.

All 256 atoms in the supercell were sampled in this way to generate the database for statistical analysis of the vacancy formation energy. Figure 4.7 plots the vacancy formation energy in three different ways. The top panel shows the total distribution of 256 samples together with a Gaussian fit (blue dash line) to illustrate the resulting, effectively normal distribution of vacancy formation energies. The average value of the vacancy formation energy is 1.96 eV and the spread within the distribution is 0.7 eV.

4.8 Vacancy migration energy

In order to perform calculations of the vacancy migration barrier, one limiting factor is the number of intermediate images used in the NEB implementation. Since the migration barrier height is the most important quantity and the specific migration pathway is of little significance for the study, it is worth testing if a single intermediate image computation is sufficient to accurately capture the barrier height.

Two migration pathways were chosen for this test. In the first case, NEB calculations were performed using a single image, 3 images and 5 images, respectively. For the

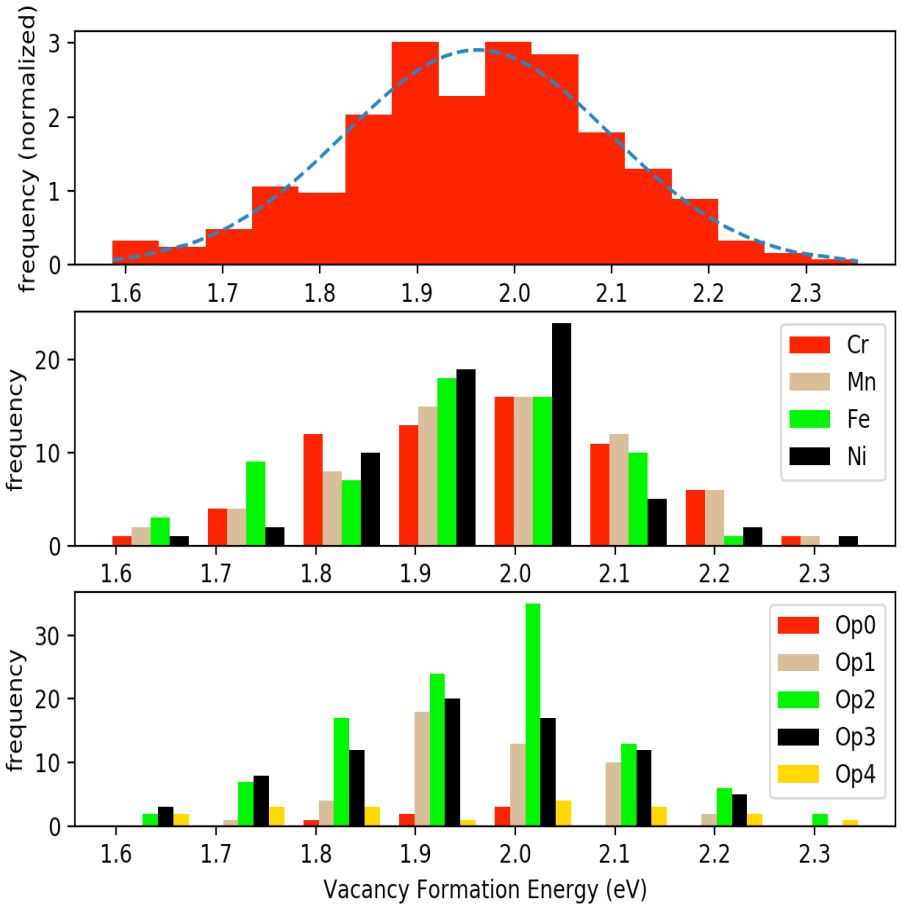

Figure 4.7 Vacancy formation energy distribution under different criteria: Total distribution of all 256 samples (top), distribution in terms of chemical species of the removed atom (middle) and distribution in terms of local environment (bottom).

second case, only a single image versus a 3-image calculation was performed. For both of these two samples, the barrier height computed from a single-image NEB implementation agreed within 0.01 eV compared to the value calculated using either a 3-image or 5-image NEB setup. Figure 4.8 shows a representative result for one vacancy migration pathway. Notice that although the shape of migration pathway changes as more intermediate images are included, the barrier height only varies between 1.434 and 1.435eV. Thus, the single-image NEB computation appears justified in being able to provide the most computationally efficient method for sampling the vacancy migration energy barrier.

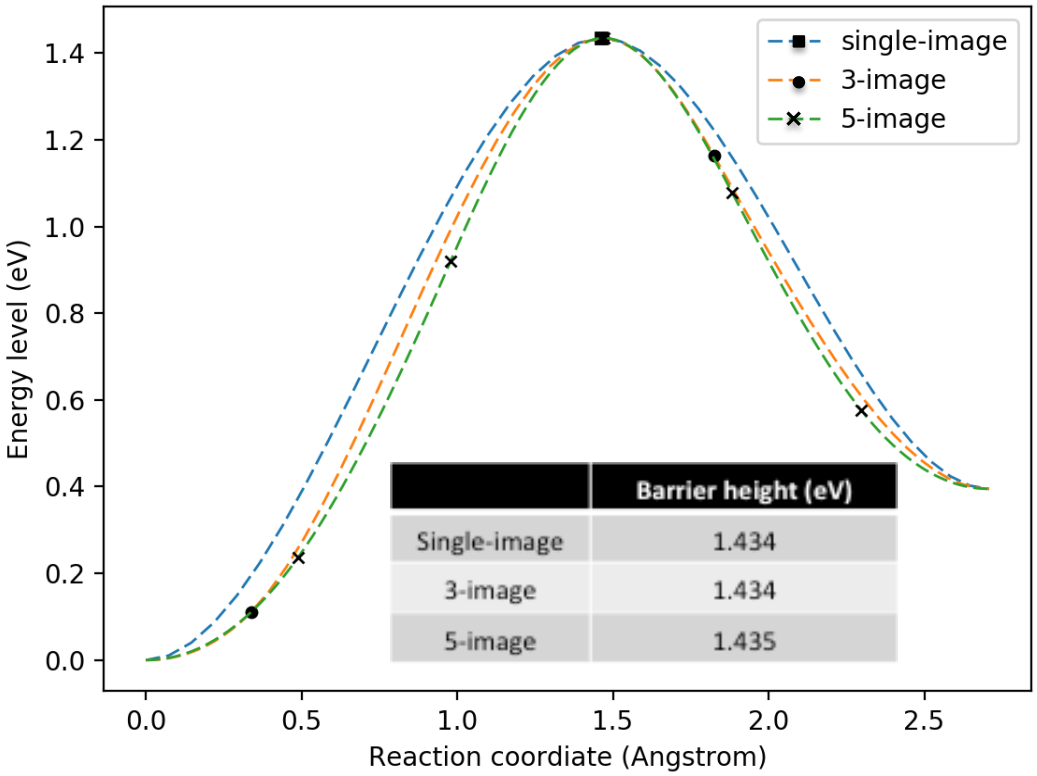

Figure 4.8 Representative NEB calculation of vacancy migration barrier based on different number of intermediate images in a 255-atom supercell. Note that while the shape of migration barrier curve is different, the barrier height only varies by 0.001eV.

22 vacancy migration barriers were calculated from different initial local environments, and the results are presented in Table 4.9. It is important to note that due to the non-equivalent energy of the vacant sites with different elements, a different energy barrier is obtained for the forward and backward migration jumps. Thus, the barrier in Table 9 is listed in the format of ($E_m^{forward}$, $E_m^{backword}$). The calculated migration energy values have a large spread, ranging from 0.55 to 1.68 eV. Notably, the migration barrier is found to be independent upon whether the local environment is uniform or biased around the diffusing vacancy. On the other hand, the magnitude of migration barriers seem to be dependent upon the element that hops into the vacancy. Figure 4.9 shows the scatter of migration barriers with respect to the element-vacancy exchange pairing. While there is considerable overlap between the spread of migration energies of each element, a trend of the spread can be observed that vacancy exchanges with an Fe atom have the largest migration barriers, while the lowest barriers are calculated for vacancy exchange with Cr or Mn.

Table 4.9 Forward and backward migration barrier height in HEA. Minimum and Maximum barrier height are highlighted in bold.

	Diffuse by Cr	Diffuse by Mn	Diffuse by Fe	Diffuse by Ni
Op0	(0.91, 0.88)	(0.98, 0.84)	(1.3, 1.18), (1.44, 1.29), (1.14, 1.14)	(0.96, 1.00)
Op1	(0.81, 0.72)	(0.78, 0.81)	(1.14, 1.11)	(1.20, 1.36)
Op2	(0.64, 0.62)	(1.31, 0.92)	(1.47, 1.19)	(1.13, 0.91)
Op3	(1.43, 1.04)	(**0.55**, 0.86)	(1.35, 0.98)	(1.28, 1.17)
Op4	(1.04, 1.07)	(0.74, 1.07)	(**1.68**, 1.42)	(1.19, 1.08)

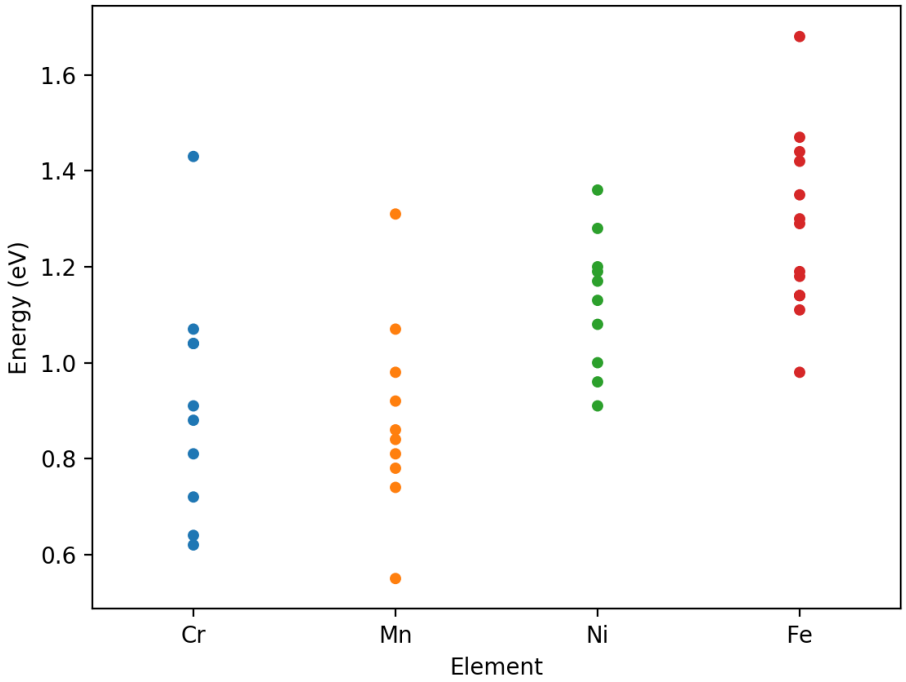

Figure 4.9 Spread of vacancy migration energies via exchanges with Cr, Mn, Ni and Fe. Notice that migration barriers are larger for vacancy exchange via Fe, while smaller for vacancy exchange via Cr or Mn.

4.9 Discussion

4.9.1 Defect modeling of HEA formed by 3d transition metals: magnetism, supercell size and chemical potential

Several recent DFT modeling efforts have studied magnetic structures of concentrated binary, ternary and quaternary alloys formed by 3d elements. Zhao and co-workers performed DFT calculations of binary systems[54] that indicate the magnetic structure is stable for Ni-Co and Ni-Fe binaries, where both constituents have the same preference for spin orientation. However, in the binary alloy formed by FM Ni and AFM Cr, the Cr exhibits magnetic frustration in which the Cr can have alternate spin directions. For a supercell of the same atomic configuration, this difference in magnetic ordering can result in a 0.27 eV difference in the enthalpy of the 108-atom supercell[54]. Piochaud[115] has performed DFT calculations of the ternary Fe-10Ni-20Cr alloy. While Cr moments also exhibit alternate spin directions, they are controlled consistently by the 1nn Fe moments and have been found to be quite insensitive to magnetic moment initialization. Equimolar FeNiCoCr has been studied as a concentrated quaternary system by Niu, Tamm and Zhao[112, 113, 142]. As in the binary Fe-Cr and ternary Fe-Ni-Cr, the Cr in FeNiCoCr was also calculated to exhibit alternate spin orientations in both small and large supercell simulations. However, for a given supercell of the same atomic configuration, no local minimum due to magnetic instability was reported.

In contrast, our calculations reveal magnetic frustration can lead to change in enthalpy as large as 0.3 eV for a 108-atom supercell, and the final magnetic structure is highly dependent upon the moment initialization. It is possible that the magnetic frustration exerts a smaller influence on the magnetic structure of the Fe-10Ni-20Cr alloy since the chemical and magnetic environment is dominated by FM iron. On the other hand, though neither NiFeMnCr nor FeNiCoCr HEA has a major elemental constituent that dominates the chemical or magnetic environment, the magnetic properties of these two HEAs can be drastically different. As noted previously, Ni, Co and Fe are all FM and represent 75% of the FeNiCoCr alloy. In our NiFeMnCr HEA, the magnetic behavior of Mn is very different from Co, and also different from that of the other elemental constituents, leading to a much less uniform magnetic environment in NiFeMnCr.

However, in a system with local magnetic frustration, for every interpolated image and the starting/ending configuration, local minima may exist between the starting state and the "real" optimized state. Failure to avoid even just one local minimum would give rise to an unphysical pathway. Figure 4.10 illustrates two vacancy migration pathways calculated for a 31-atom NiFeMnCr supercell calculated by VASP. In both calculations, a Cr vacancy is created and NEB is used to model its migration to another site occupied by Cr. The diagram on the left represents a normal Cr vacancy migration pathway. Adding more intermediate images in the calculation refines the migration pathway and saddle point location, but does not change the general shape of the curve, or the resulting activation energy barrier. On the other hand, for the abnormal one on the right, a local

minimum close to the starting atomic configuration is discovered when interpolating more images, indicating that the starting atomic configuration is not stable. After re-calculating the enthalpy of the starting configuration using several different initial magnetic moments, it was found that the starting configuration can relax to a similar configuration and energy as the local minimum identified in Fig. 4.10 (right).

Therefore, the initial starting configuration itself represents a metastable configuration and should be avoided as the reference state for defect modeling. The process of avoiding local minima, or metastable configurations, and identifying the physical migration pathway can even become more challenging when modeling more complex defect transport mechanisms, such as self-interstitial dumbbell migration. On the other hand, for FeNiMnCr, it is worth pointing out that at elevated temperature, these complex and strong magnetic interactions will not persist and chemical disorder effects should dominate the calculated enthalpies for this particular alloy.

In addition to magnetism, supercell size and chemical potential are also two critical aspects for accurately calculating the defect energetics in HEA formed by 3d transition metals. To study the unique chemical disordering effect in an HEA, a large number of alternate configurations, or arrangements of the local chemical environments is needed for establishing sufficient sampling statistics of the defect energy. This can be accomplished by establishing numerous small supercells (20 – 30 atoms)[143, 144]or one single large supercell (more than 100 atoms)[115, 132, 142]. While the latter approach is computationally more efficient, it is more difficult to capture the right defect physics due to several intrinsic deficiencies. A smaller supercell necessarily is calculating very large point defect concentrations due to the periodic boundary conditions. Supercell sizes below 100 atoms can only model vacancy concentration above 1%, which is at least an order of magnitude higher than thermal vacancy concentrations for typical alloys near the

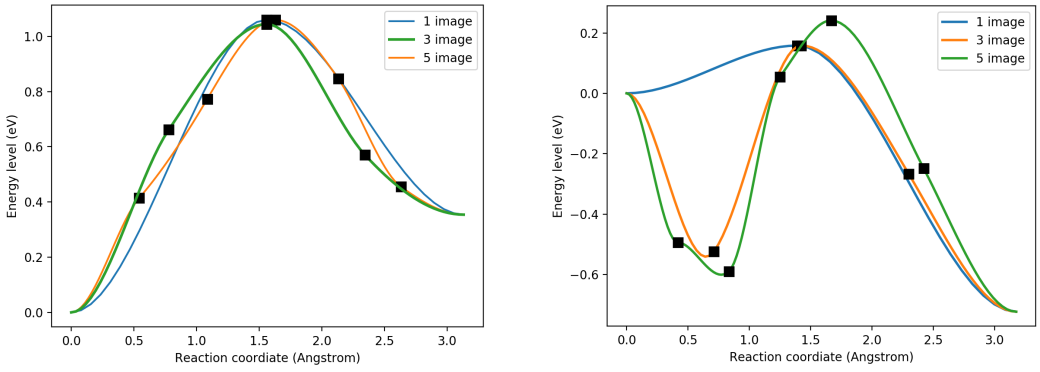

Figure 4.10 Normal (left) and unphysical (right) vacancy migration pathways found in for Cr vacancies in a 32-atom supercell.

melting temperature. Small supercells also give rise to larger periodic boundary effects. For modeling conventional metal and dilute alloys, periodic boundary effects can cause residual interactions between the vacancy and its periodic images. On the other hand, the periodic boundary conditions for a concentrated HEA will also result in "artificial" medium- or long-range chemical ordering due to repeating supercell images, which has not been observed in neutron or X-ray scattering[13]. While large supercells cannot ultimately eliminate these two artifacts, their impact is reduced relative to smaller supercells. Finally, while one large supercell leads to one reference ground state, smaller supercells, which are intended to study one material system, can potentially lead to multiple reference states. Although a previous *ab initio* calculation on FeNiCoCr has shown that free energy variation between different supercells is small[143], this may not be the case for NiFeMnCr, in which we have observed stronger and more complex magnetic interactions. Finally, as was discussed in Section 4.6, the chemical potential of the same element is different between NiFeMnCr and pure metals. This is also observed for the chemical potential calculation of binary[54], ternary[115, 132] and quaternary[142] concentrated alloys. Thus, when computing defect formation energies in HEAs, it is important to re-evaluate the chemical potential based on the actual alloy composition rather than using pure metal values as an approximation.

4.9.2 Statistical distribution of vacancy formation energy

We have compared the calculated vacancy formation results from this study with those from conventional dilute and concentrated austenitic Fe-Ni-Cr alloys[115, 145], as listed in Table 4.10. The distribution of the vacancy formation energy is 1.82 to 1.95eV for the dilute Fe-Ni-Cr alloy[145], 1.76 to 2.19eV in the Fe-10Ni-20Cr concentrated alloy[115] and 1.59 to 2.35eV for the studied NiFeMnCr HEA. From this limited comparison, it appears that the spread in the vacancy formation energy increases as the alloy composition becomes more concentrated and complex, presumably due to higher variability of local chemical environment. The mean vacancy formation energy obtained from our calculations of FeNiMnCr is 1.96eV. This value is slightly larger than vacancy formation energy of pure Ni, and comparable to the average vacancy formation energy of Fe-10Ni-20Cr alloy. This is expected since the melting temperature of NiFeMnCr HEA (1220 ˚C) is also comparable to that of pure Ni (1455 ˚C) and conventional SS316 (1400 ˚C). Besides, the equilibrium vacancy concentration C_0 is determined by:

$$C_0 = \exp\left(\frac{S_f}{k}\right) \exp\left(\frac{-E_f}{kT}\right), \qquad \text{(Eq. 4.7)}$$

where S_f is vacancy formation entropy and E_f is vacancy formation energy. Thus, if vacancy formation entropy, which include mixing entropy, vibrational disorder and magnetic disorder from the introduction of vacancy, is not fundamentally different from conventional metals and alloys[146], the equilibrium vacancy concentration in NiFeMnCr HEA should be very similar to those in conventional metals and alloys.

Table 4.10 Comparison of vacancy formation energy spread and average between pure f.c.c metal, dilute Fe-Ni-Cr alloy, Fe-10Ni-20Cr, NiFeMnCr HEA and FeNiCoCr HEA[48, 115, 142, 145].

	Range (eV)	Average (eV)
Ni	N/A	1.79
Dilute Fe-Ni-Cr	1.82-1.95	N/A
Fe-10Ni-20Cr	1.76-2.19	1.96
NiFeMnCr HEA	1.59-2.35	1.96
FeNiCoCr HEA (256-atom supercell study)	1.55-2.25	N/A

Chen[144], Middleburgh[143] and Zhao[142] computed vacancy formation energies for another quaternary HEA, FeNiCoCr. While Zhao's computation was based on 256-atom supercells, both Chen and Middleburgh used much smaller, 20- to 30-atom supercells[143, 144] to perform the formation energy calculation. In addition, while Zhao computed chemical potentials for the FeNiCoCr system, both Chen and Middleburgh used pure metals as the reference. Vacancy formation energy ranges from 1.6 to 2.2eV from Zhao's study (listed in Table 4.10), but ranges from 0.7 to 3.1eV from Chen and -0.75 to 2.75eV from Middleburgh. The huge difference between the statistical distributions of these three studies shows the importance to use large supercells and reasonable chemical potentials for HEA's defect energetics computation, as explained in Section 4.9.1. As listed in Table 4.10, the range of vacancy formation energy is similar for NiFeMnCr and FeNiCoCr. Thus, replacing Mn with Co does not appear to significantly impact the total statistical spread of vacancy formation energy. However, while the distribution is independent of the chemical species for FeNiMnCr (discussed in Section 4.7), it was claimed that vacancies formed by removing Cr atoms (i.e. Cr vacancies) have a higher formation energy in FeNiCoCr than those formed at other three elements[142]. This difference can be understood by consideration of two different aspects: First changes in chemical and magnetic properties between Co and Mn may result in higher Cr vacancy formation energy in FeNiCoCr. On the other hand, the statistical sampling size is on the order of 20 for each element in the FeNiCoCr study[142], which is smaller than used (64 for each element) in this study. Given the fact that Cr's vacancy formation energy spread is only ~0.2eV larger than that of the other elements in the FeNiCoCr study[142], the discrepancy may only be a statistical artifact.

It is worth noting that the element-specific vacancy formation energy distribution can have important physical implications. If the vacancy formation energy distribution is the same for each element (i.e. NiFeMnCr), formation of vacancies does not have chemical bias. At a given temperature, each element has an equal chance to be removed and form a vacancy. This chance is described by one unique statistical distribution, which is determined by the atomic arrangement (i.e state of SRO) in the NiFeMnCr HEA. A vacancy formed in this HEA system can thus be generically named as "HEA vacancy" rather than "Cr vacancy" or "Fe vacancy". However, if there is chemical bias for removing a certain element to form a vacancy, the vacancy formed by this element needs

to be treated independently and there is no "unified" statistical distribution to describe vacancies formed by different elements.

4.9.3 Vacancy migration energy

The defect migration process is closely related with crucial radiation degradation phenomena, such as void swelling[147] and elemental segregation[67, 68]. Though the simulation of these degradation process needs comprehensive datasets of both vacancy and interstitial migration energies, and also needs a proper computational platform (such as kinetic Monte Carlo) to model the random walk process and compute correlation factors, vacancy migration energy statistics obtained from this study can still have implications for the kinetic processes that would occur in FeNiMnCr HEA. For FeNiMnCr, while there is a large spread of migration energy (0.55 – 1.68 eV), the average migration energy from the data is 1.07eV, which is similar to that in pure Ni (1.04eV[48]), and slightly larger than the Cr and Fe solute-vacancy exchange migration barrier in Ni (0.8eV for Cr, 0.95eV for Fe[148, 149]). Although a higher vacancy migration energy would generally indicate lower vacancy-atom exchange frequencies, suggesting slower diffusion in NiFeMnCr HEA that is consistent with reduced dislocation loop coarsening and low void swelling observed in ion irradiated HEA (Chapter 2), the slight difference in migration energy alone is not sufficient to cause pronounced sluggish diffusion that could lead to the observed order of magnitude reduction in void swelling between NiFeMnCr HEA and conventional austenitic Fe-Cr-Ni alloys. Zhao sampled vacancy migration energies in FeNiCoCr HEA, which ranges from 0.3 – 1.4 eV[142]. While the width of the spread is similar, the magnitude is moderately lower than that for FeNiMnCr. Thus, replacing Mn with Co can alter vacancy migration energy, suggesting certain chemical species can be as important as chemical disordering in studying defect migration process in HEAs.

The relative magnitude of vacancy migration energy for different elements, on the other hand, can have important implications for predicting the elemental segregation trend at grain boundaries. An element with a lower vacancy migration energy indicates that vacancy diffusion may preferentially couple with this species, resulting in depletion of that element at grain boundaries[68]. Similar to conventional austenitic Fe-Ni-Cr alloy, where Ni has a higher vacancy migration energy than Cr, a large fraction of the migration energy barrier distribution is found to be higher for Ni compared with Cr in NiFeMnCr. This is consistent with Ni enrichment and Cr depletion at grain boundary observed in ion irradiated HEA in Chapter 2, although the possible contribution of interstitial coupled diffusion[67] also needs to be considered to obtain a thorough model of elemental segregation for NiFeMnCr HEA. On the other hand, for dilute Fe-Ni-Cr austenitic alloy, *ab initio* studies by Malerba[148], Tucker[149] and Klaver[145] showed consistent ranking of the vacancy migration barrier height for Cr, Fe and Ni: Ni > Fe > Cr. Similarly, Zhao's study[142] of vacancy migration energy barriers in FeNiCoCr shows that the occurring frequency of large migration barrier is: Ni > Fe > Cr. However, in the case of NiFeMnCr

HEA, the occurring frequency of barrier height changes to: Fe > Ni > Cr. Thus, the migration barrier height sequence of NiFeMnCr HEA is not only different from conventional Fe-Cr-Ni alloys, but also compared to a HEA of different chemical composition (i.e. replacing Mn with Co). Thus, this difference in sequence may not only be related with the chemical disordering of HEA, but also with the chemical effect of certain elements, such as Mn or Co. Note that in dilute Fe-Ni-Cr alloy, vacancy migration is treated as solute (Cr and Ni) exchange with vacancy and solvent (Fe) exchange with vacancy, and the migration energy barrier sequence is explained by the size of the solute with respect to the matrix element. However, this categorization no longer applies for HEA since there is no dominant chemical environment.

The large range of values in the vacancy migration and formation energy in FeNiMnCr coincides with the lattice potential energy and saddle point energy fluctuation hypothesized by Tsai[21]. On the other hand, based on the sampled pathways in this study, the migration barrier may not be randomly distributed. The migration barrier is likely to be higher for diffusion via Fe than other elements. In general, a biased distribution of different migration barriers can lead to correlated diffusion, which can greatly alter the long-range transport of point defects and solutes. While Tsai claimed that the large fluctuation in migration energy can lead atoms to migrate to local "atomic traps" with anomalously large migration barriers and result in sluggish diffusion, the opposite can be true as well: by connecting a number of low migration energy pathways, a fast diffusing percolation path can be constructed to produce fast diffusion in certain directions. Without long range transport simulation based on a thorough database of defect migration energies at different kinds of local environments, whether or not this large spread of migration energy leads to sluggish diffusion remains uncertain.

4.10 Conclusions

Ab initio modeling is conducted to investigate the bulk and vacancy properties of FeNiMnCr HEA. The modeling study reveals:

(1) Little difference in DoS or band structure can be observed due to composition change. Thus, it is reasonable to model the near equimolar FeNiMnCr HEA as equimolar composition.

(2) Strong magnetic frustration is found due to the simultaneous presence of 3d elements of different magnetic behaviors. The calculated ground state can be strongly affected by magnetic frustration. For one vacancy configuration, magnetic frustration can lead to vacancy formation energy difference of ~0.3eV.

(3) For temperature of nuclear application interest, it is reasonable to neglect magnetic interactions. Both MC simulation and experiment shows no magnetic order to disorder

transition temperature. KKR-CPA calculation based on DLM theory shows all moments vanishes except for Fe, and the magnitude reduces to 1.1 μ_b.

(4) An efficient method for computing HEA's chemical potentials is proposed, implemented and validated. For this FeNiMnCr HEA, chemical potential from uniform environment is representative for all sites.

(5) Vacancy formation energy is evaluated as a statistical distribution. This statistical distribution is weakly dependent upon either the chemical species of the atom that the vacancy is from, or local chemical environment.

(6) 44 vacancy migration barriers are computed. Migration energy shows a large spread, from 0.55 to 1.68eV. Migration barrier height seems to be independent upon whether the local environment is uniform or biased around the vacancy. Finally, Fe has a higher occurring frequency of large migration barriers.

CHAPTER FIVE

AB INITIO POSITRON LIFETIME CALCULATION

5.1 Introduction

In Section 6 of Chapter 3, PAS measurements were presented to characterize the evolution of vacancy-type of defects for neutron irradiated HEA. Since no theoretical positron observable calculations have been reported in the literature for any HEA, the lifetime calculations for pure Fe was used as a reference for interpretation of the experimental results. In this chapter, NiFeMnCr HEA's positron lifetime is directly computed to compare with Fe and other pure metal positron lifetime to verify if it is reasonable to use Fe as the reference for NiFeMnCr lifetime studies. Accurate computation of lifetime values in this chapter can also facilitate other possible characterization work on this HEA and other HEA of similar composition.

Positron lifetime is computed by:

$$\tau = \frac{e^2}{\pi r_0^2 c} \int d^3r \, n^+(r) n(r) \Gamma(n(r)), \qquad \text{(Eq. 5.1)}$$

where $n^+(r)$ is positron density, $n(r)$ is electron density and Γ is the enhancement factor that accounts for the columbic interaction between positron and electron.

The HEA positron lifetime was calculated using a finite element code for modeling positron – electron wave function overlap developed at Lawrence Livermore National Laboratory[150, 151]. The code contains two subroutines: The first one is DESCLAUX. It calculates the atomic charge density of an atom using Hartree-Fock self-consistent field approach[152] and the code accommodates numerous exchange correlation functionals based on local density approximation (LDA)[153, 154], In addition, it includes an option to compute the positron distribution around the atom, and the resulting Doppler broadening spectrum[82, 155]. The second subroutine is FEPS. Based on user-provided lattice information, FEPS overlaps the atomic charge densities from DESCLAUX, generates the $n(r)$, and computes $n^+(r)$ and the corresponding lifetime τ. The positron density is determined by solving the positron wave function, ψ^+, in the positron Schrödinger equation:

$$\left[-\frac{1}{2}\nabla^2 - V_{ion}(r) - V_{Hartree}(r) + V_{corr}\big(n(r)\big)\right]\psi^+ = E^+\psi^+, \qquad \text{(Eq. 5.2)}$$

where $-\frac{1}{2}\nabla^2$ is the kinetic energy, $V_{ion}(r)$, $V_{Hartree}(r)$ are the Coulumb interactions between nuclei and electrons, and $V_{corr}\big(n(r)\big)$ is the correlation interaction between

electrons and positrons. Electrostatic interaction with electrons and with nuclei provide the dominant part of the potential, and the remaining correlation part of the potential is formulated based on the LDA[150]. For the enhancement function Γ, both LDA[150] and GGA[156] forms are provided by the code. Different from popular plane wave (PW) based methods to solve the Schrödinger equation, such as implementations used in VASP[127] and Quantum Expresso[157] code packages, this positron code package utilizes a finite element (FE) based method. While PW based methods involve time-consuming Fourier transform between real space and reciprocal space, computation is performed directly in real space in FE based methods. Thus, FE based method has the potential to treat large systems with thousands of atoms both efficiently and accurately[151, 158]. While the accuracy of computation is controlled by the number of k-points in reciprocal lattice in PW based method, it is controlled by the number of finite elements in real space in FE based method. Since no structural relaxation is performed within the code, atomic positions need to be optimized in VASP and then provided to the FEPS subroutine.

5.2 Bulk and vacancy lifetime for benchmarking

To test the accuracy of the code, the lifetime of several bulk materials (Cr, Fe, Ni, Cu and 3C-SiC) were computed for benchmarking. Since the crystal structure of all these materials is cubic, a 12x12x12 finite element mesh was used. Table 5.1 shows the benchmarking results in comparison with previous theoretical calculation results. Overall, the LLNL-Positron code shows good agreement with reference values for both metals and ceramic materials.

Mono-vacancy lifetimes were computed for Cu using three cells of different sizes: 4-atom unit cell, 2x2x2 32-atom and 3x3x3 108-atom supercells. To obtain the same computational accuracy in these three supercell sizes, the number of finite elements was increased proportionally with supercell size (12x12x12, 24x24x24 and 36x36x36 finite elements for 1x1x1, 2x2x2 and 3x3x3 supercell). Computational results are shown in Table 5.2. For comparison, a previous theoretical calculation reported that Cu mono-vacancy lifetime is 169ps[159].

Table 5.1 Comparison between results from LLNL-Positron code and those from references (unit in ps).

	BCC Cr	BCC Fe	FCC Ni	FCC Cu	3C-SiC
LLNL	109	103	99	109	137
Literature reference	104[159]	102[159]	96[159]	108[159]	141[160], 144[161]

Table 5.2 Mono-vacancy lifetime of Cu calculated by three cells of different sizes (unit in ps).

	Unit cell	2x2x2 supercell	3x3x3 supercell
Mono-vacancy lifetime	167	159	168

While calculations based on unit cell and 3x3x3 supercell agree with the reference value of 169 ps, this is not the case for 2x2x2 supercell. The discrepancy, which was observed in a previous study on pure Cu (Figure 5.1), can be explained by the two sources of errors resulting from finite supercell size[162]. First, the interaction of vacancies due to periodic boundary conditions can delocalize the positron wave function. Therefore, the vacancy interaction becomes stronger and the positron lifetime becomes shorter for the smaller supercells. Second, the positron wave function is required to terminate at the cell boundaries. Thus in insufficiently large calculations, the positron density at the cell boundary is finite and correspondingly, too large of a positron density results at the center of vacancy. So the smaller the computational supercell, the longer the calculated positron lifetime. For the smallest cell, the error from wave function termination may cancel the error from the high vacancy interaction, so the lifetime agrees with the expected reference. However, when supercell size increases, the wave function termination effect declines faster than the vacancy interaction effects, thus, the lifetime is somewhat shorter than the reference value. Finally, when the supercell size is large enough, both error sources are reduced and the lifetime converges to an accurate value comparable to the reference value. This indicates that for precise lifetime calculation, a sufficiently large supercell is needed to minimize the errors.

5.3 Bulk and vacancy lifetime for HEA

Bulk and vacancy lifetime were computed from the same 256-atom supercell generated by ATAT. This large supercell minimized errors from wave function termination and the vacancy interaction. The relaxed supercell volume and atomic coordinates from VASP were used as the input for the positron calculation. The finite element mesh consisted of either12x12x12 or 24x24x24 grid points to test the convergence of the lifetime with respect to finite element mesh size. The calculated bulk (perfect crystal) lifetime is 97 ps for both mesh sizes. Thus, the smaller 12x12x12 mesh has been used for the vacancy lifetime calculation. Compared with the bulk lifetime of pure metals listed in Table 5.1, the bulk lifetime of this HEA is closer to f.c.c Ni (99 ps) than b.c.c Fe (103 ps) or b.c.c Cr (109 ps)

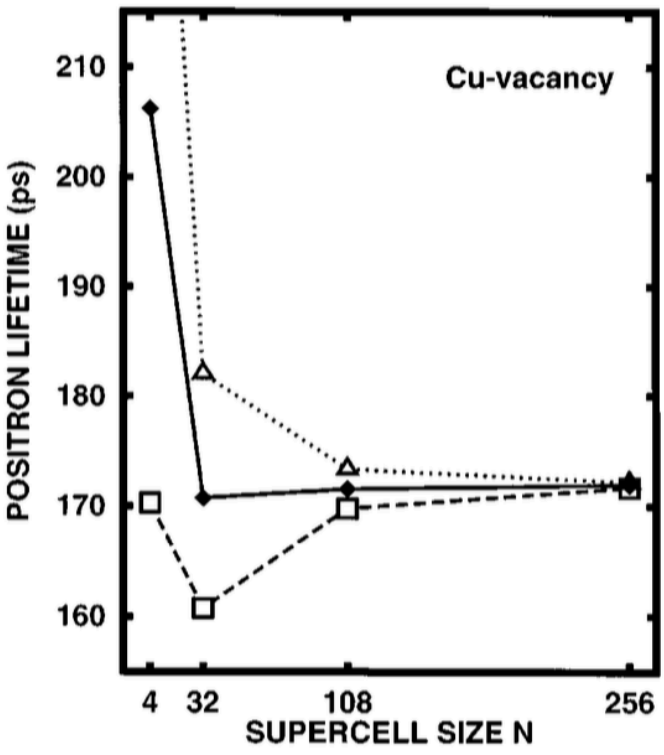

Figure 5.1 Convergence of positron lifetime with respect to supercell size for single Cu-vacancy, as reproduced from Ref[162].

While the study of supercell size effect of Cu Section 5.2 (Fig. 5.1) indicates that a 108-atom supercell is large enough to obtain convergence of positron lifetime, HEA may present unique effects different from a pure metal. Note that due to random atomic configuration on the NiFeMnCr lattice sites, supercells of different sizes will have local chemical configurations, and/or different SRO. This effect is not present in the supercell size effects for pure metals discussed in Section 5.2, so an independent supercell size effect study for HEA needs to be performed for both perfect supercells and supercells with a single vacancy. Table 5.3 lists the bulk positron lifetime as well as the lifetime of a single vacancy computed from supercells of different sizes. Bulk positron lifetime is computed based on supercells of four sizes: 1x1x1, 2x2x2, 3x3x3 and 4x4x4 (unit in cell parameter). Note that for supercells of size 2x2x2, 3x3x3 and 4x4x4, SQSs are used to construct random atomic configurations. On the other hand, for cell size of 1x1x1, the structure has to be perfectly ordered (since there is only one way to assign the atoms on the lattice sites) and thus the chemical ordering in 1x1x1 cell is very different from those in larger supercells (i.e. 2x2x2, 3x3x3, 4x4x4 supercells). For the single vacancy lifetime calculation, a vacancy was constructed by removing one Cr atom from the structure with no structural relaxation. The bulk lifetime was 96ps from the unit cell calculation and remains 97ps for all larger supercell calculations. Thus, the change in short range order

Table 5.3 Calculated bulk and single vacancy lifetime based on supercells of different sizes (unit: ps).

	Unit cell	2x2x2 supercell	3x3x3 supercell	4x4x4 supercell
Bulk	96	97	97	97
Single vacancy	157	163	169	164

does not affect the bulk positron lifetime in FeNiCrMn HEA. The weak effect of short range order on positron lifetime is also observed in Fe-Al alloys, where calculations show a ~2ps bulk lifetime variation between structures of different atomic arrangements on the same crystal lattice (DO3, B2 and A2 phases)[163]. This weak correlation between SRO and bulk positron lifetime can be understood by the fact that SRO does not change the metallic bonding in HEA. Thus, the electron density of the valance band, which largely determines the bulk positron lifetime, barely varies for supercells of different SRO.

On the other hand, the calculated single vacancy positron lifetime varies between 157ps for unit cell and 169ps for the 3x3x3 supercell. Unlike the mono-vacancy lifetime for Cu discussed in Section 5.2, the convergence of the lifetime is not observed in our calculations even for a 4x4x4 supercell. Since artifacts caused by periodic images should typically be small at this supercell size, the non-converging single vacancy lifetime can only be explained by a change in the local valence electron density at the vacant site due to a variation in local chemical ordering for the vacancy formed in different supercells. The effect of local chemical ordering will be discussed in more detail in Table 5.5 and the following paragraphs.

As discussed with respect to the PAS measurements in Chapter 3, and *ab initio* vacancy formation energy calculation in Chapter 4, the vacancy volume and local chemical environment vary greatly in HEA, and the positron is very sensitive to both effects. Thus, it is necessary to sample vacancies formed at different atomic sites, evaluate the spread of vacancy lifetime and compute their average positron lifetime, much as was done for considering the average vacancy formation energy. Also, it is important to use the relaxed atomic coordinates from VASP because local atomic displacements around the vacancy can have a large impact on vacancy lifetime. Table 5.4 shows the lifetime results of four vacancy samples, which compares the calculated lifetime values using fixed atomic coordinates versus relaxed ones. Structural relaxation around a vacancy decreases the positron lifetime at the vacancy by about 7ps for vacant Mn, Fe and Ni sites, and by 12ps for a vacant Cr site because atoms relax inward and increase electron density at the vacancy site. A theoretical analysis by Korhonen et al[162] on pure copper indicated that the single vacancy positron lifetime shortened by 9ps after structural relaxation, which is similar to the lifetime values calculated in this work for vacancies in the NiFeMnCr HEA.

Table 5.4 Calculated positron lifetime in 256 atom NiFeMnCr HEA containing a single vacancy based on fixed or relaxed coordinates (all units in ps).

	Cr site	Mn site	Fe site	Ni site
Fixed coordinates	164	165	166	167
Relaxed coordinates	152	158	159	160

To estimate the average value of the calculated positron lifetime, and the range of calculated values, 24 vacancy configurations were selected from the DFT calculations presented in Chapter 4. These 24 configurations provide a range of vacancy formation energies, different atomic species and different local chemical environments. The calculated positron lifetime of these samples spans from 150 to 164ps. The average is 158ps with a standard deviation of 3ps. Table 5.5 compares the computational result of this HEA with some typical pure metals. Single vacancy lifetime of this HEA is smaller than Cr, Fe and Ni, and is closest to that of Ni.

Figure 5.2 plots the calculated vacancy formation energy against the calculated positron lifetime to evaluate if there is any correlation between these two quantities. If we disregard several extreme lifetime values (150ps, 152ps and 164ps) and focus on the data closer to the mean value, both the formation energy and predicted positron lifetime appear randomly scattered around the average. Thus, there does not appear to be a correlation between these two quantities, suggesting that positron lifetime is not solely determined by vacancy formation energy within NiFeMnCr HEA.

Table 5.6 lists the calculated positron lifetime of single vacancies formed by different atomic species. Overall, the average and standard deviation for all elements are very close for all samples (158 ± 3ps). The lifetime associated with a Ni vacancy is a bit higher, but is within the scatter of the overall lifetime values calculated. Table 5.7 presents the positron lifetime computed at vacancies with different local environments, where the definition introduced in Section 4.6 is used for specifying the local environment. Average lifetime is basically the same for all environments. On the other hand, the standard deviation is 2ps for Op0, Op1 and Op2, but increases to 4ps for Op3 and to 6ps for Op4. On one hand, the general spread of the data indicate that variation in local chemical environment produces a large scatter in the mono-vacancy positron lifetime of an HEA even for a supercell size of 4x4x4. This helps explain the non-converging nature of the single vacancy lifetime presented in Table 5.3. On the other hand, to further investigate the correlation between the local volume and chemical environment around vacant sites and the magnitude of positron lifetime, more statistics are needed.

Positron lifetime calculations for di-vacancy, tri-vacancy and four-vacancy clusters were also performed to investigate the impact of the size of vacancy clusters formed in the sample. The atomic coordinates in these calculations, however, were not relaxed to account for local structural distortion around the vacancy clusters. Since the previous

Table 5.5 Comparison of mono-vacancy lifetime of HEA with pure metals. Lifetime values for metals are from Ref [159] (all units in ps).

	BCC Cr	BCC Fe	FCC Ni	HEA
Mono-vacancy lifetime	180	177	166	158±3

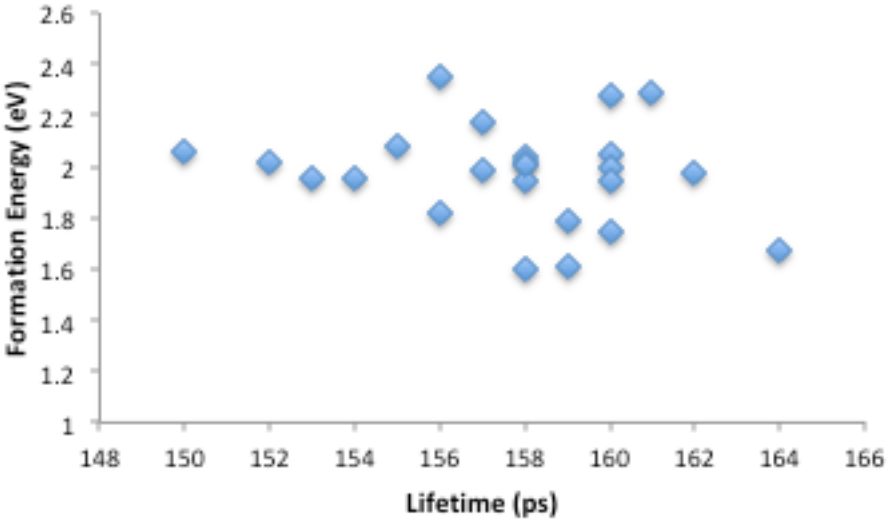

Figure 5.2 Formation energies plotted as a function of positron lifetimes. No clear correlation appears between these two parameters.

Table 5.6 Vacancy lifetime computed at vacancy formed by different element.

	Cr	Mn	Fe	Ni
Lifetime (ps)	158±4	156±4	157±2	160±2

discussion showed that un-relaxed coordinates will result in longer lifetime, these preliminary computational results of vacancy cluster lifetime should be treated as an upper bound for each cluster size when considering any comparison to experimental data. Table 5.8 presents the calculated results. For tri-vacancy clusters, two cluster configurations, in which the vacancies are arranged in a line or a triangle, are considered. For four-vacancy clusters, three cluster configurations, in which the vacancies are ordered along a line, a hat or a tetrahedron have been used. The graphical representation of these tri- and four-vacancy clusters are shown in Figure 5.3. Names such as 3Cr and 3Cr1Fe indicate the composition of the clusters, namely a tri-vacancy cluster composed of three Cr vacancies and a four-vacancy cluster composed of three Cr and one Fe vacancies.

Table 5.7 Vacancy lifetime computed at different local environment.

	Op0	Op1	Op2	Op3	Op4
Lifetime (ps)	158±2	156±2	159±2	157±4	159±6

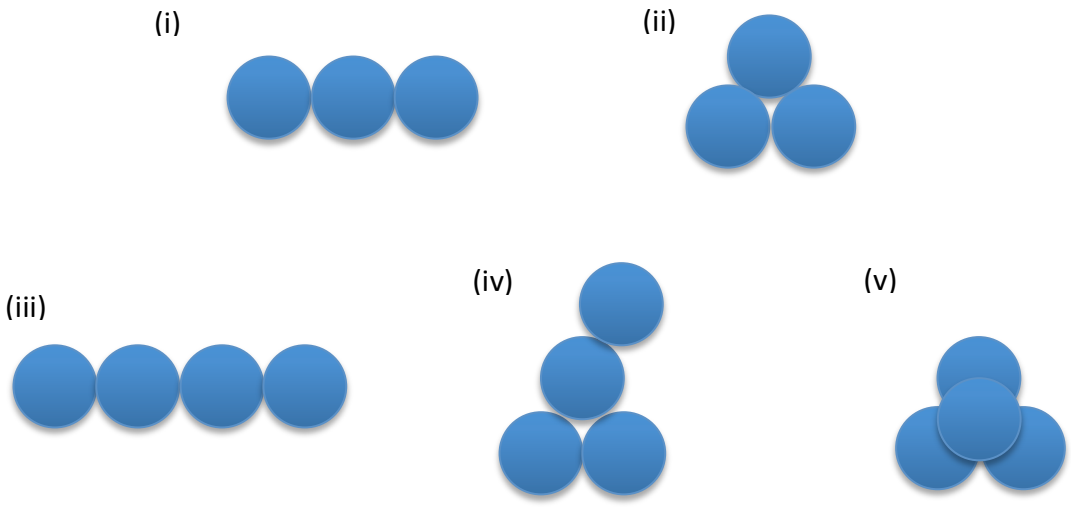

Figure 5.3 Graphical representation of tri- and four-vacancy clusters: (i) tri-vacancy line, (ii) tri-vacancy triangle, (iii) four-vacancy line, (iv) four-vacancy hat and (v) four-vacancy tetrahedron.

Table 5.8 Positron lifetime for vacancy clusters of different size and different configuration. Notice that all lifetimes here are computed form un-relaxed defect structures (All units in ps).

Di-vacancy		Tri-vacancy		Four-vacancy	
CrCr	185	3Cr (line)	185	4Cr (line)	197
CrFe	185	3Mn (line)	185		
CrMn	184	3Ni (line)	184	3Cr1Fe (hat)	210
CrNi	185				
		3Cr (triangle)	207	3Cr1Mn (tetrahetron)	225
		3Fe (triangle)	205		
		MnFeCr (triangle)	208		

Overall, the calculated positron lifetime increases as the vacancy cluster size increases. For a vacancy cluster of the same size and same configuration, such as a di-vacancy and line-type tri-vacancy, the calculated positron lifetime varies little between vacancy clusters formed by removing different atomic species. On the other hand, the calculated positron lifetime varies more significantly for clusters of the same size but different configuration, as expected. The effect of configuration can be even larger than cluster size. For example, the calculated positron lifetime barely increases from the di-vacancy to the linear cluster configuration of a tri-vacancy, but increases by ~20 ps by changing the tri-vacancy configuration from linear to a planar triangular arrangement. Similarly, for four-vacancy clusters, the lifetime increases from 197ps for a line configuration to 225ps for a tetra configuration. Thus, defect cluster configuration can be even more crucial than defect size for computation of vacancy cluster positron lifetime and identifying vacancy clusters from the PALS measurement. Finally, while the lifetime variation from PALS measurement in Chapter 3 is ~200ps – 250ps, the largest lifetime computed so far only reaches 225ps. Thus, vacancy clusters consisting of more than four vacancies are likely involved in the annealing process of the neutron irradiated HEA. Computation of positron lifetimes of larger-size clusters is needed to account for all possible defect cluster sizes in the experiment.

5.4 Conclusions

An *ab initio* positron code was used to compute positron lifetimes for a series of bulk materials, and also for bulk, single vacancy and vacancy cluster lifetimes of a NiFeMnCr HEA. The computational results show:

(1) Bulk positron lifetimes in elemental metals and silicon carbide ceramic computed by this LLNL-Positron code show good agreement with previous theoretical studies

(2) Compared with Cr and Fe, the computed bulk and single vacancy positron lifetimes of NiFeMnCr HEA are closest to those of Ni.

(3) In NiFeMnCr HEA, while bulk positron lifetime does not appear sensitive to SRO, the single vacancy lifetime is affected by vacancy formation as well as the local chemical ordering at vacancy site.

(4) For the positron lifetime of vacancy clusters, the geometrical configuration of clusters can be a very significant factor as well as local chemical ordering.

CHAPTER SIX

CLOSING PERSPECTIVES, FUTURE WORK AND CONCLUSIONS

6.1 High temperature ion irradiation

In Chapter 2, experimental characterization after heavy ion irradiation at temperatures between 400 and 700 ˚C, and doses up to 10dpa shows that the NiFeMnCr HEA has better void swelling resistance than conventional austenitic stainless steel for a moderate mid-range dose of ~10 dpa. This statement, however, is strictly limited within the damage dose and irradiation temperature in this study. The performance of this HEA under higher irradiation temperature and damage dose (and also examination of the effects of co-implanted He) remains to be investigated.

Void swelling in f.c.c metals and conventional austenitic alloys has been intensively studied over the past several decades. There are three critical parameters that define the void swelling behavior of a material: peak swelling temperature, incubation dose and swelling rate. Figure 6.1 shows the temperature dependence of void swelling behavior for neutron irradiated Cu[164]. The "bell-shaped" curve shows that void swelling is most pronounced at intermediate temperature. This "bell shape" behavior and peak swelling temperature is typical for f.c.c materials[30] and applies for both neutron and heavy ion irradiations. Note that the peak swelling temperature will shift higher for heavy ion irradiation due to higher dose rate for ion versus neutron irradiation[164, 165]. Thus, the peak swelling temperature is a signature of the temperature dependence of swelling behavior of HEA. On the other hand, this temperature is closely related with vacancy kinetics and thermodynamics, and thus can provide useful insights on the defect properties of HEA.

In addition to the peak swelling temperature, the incubation dose and swelling rate are also critical parameters to evaluate the swelling behavior of a material. Figure 6.2 shows the variation of the swelling due to thermo-mechanical treatment for SS316 after neutron irradiation at 540 ˚C[166]. Each of the swelling curves are composed of two stages: The first (transient) stage occurs at low doses and is associated with void nucleation and other transient microstructural evolution phenomena (e.g., dislocation network evolution); during this stage the magnitude of void swelling remains near zero with increasing neutron fluence. In the second (steady state) void growth stage, the void swelling magnitude is approximately proportional to neutron fluence. The transition dose between these two stages is often called "incubation dose", while the slope during the void growth stage is called the "swelling rate".

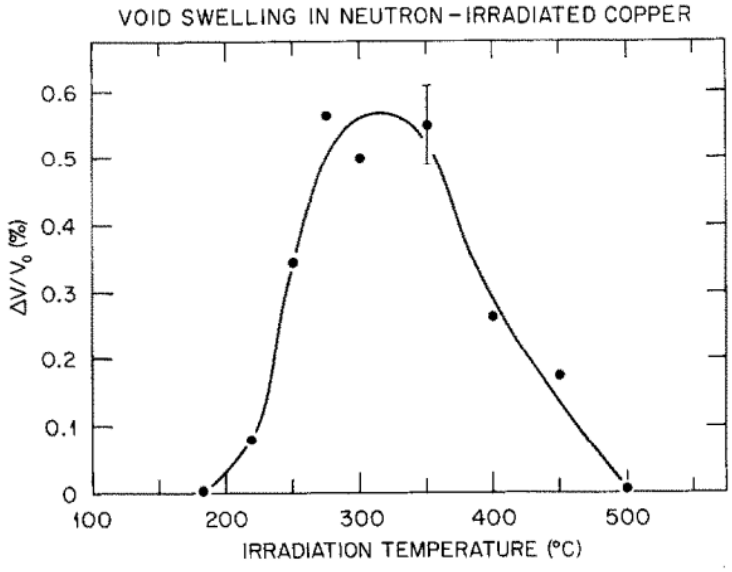

Figure 6.1 Void swelling in neutron irradiated Cu up to ~1dpa at different irradiation temperature. The "bell-shaped" curve shows that void swelling is most significant at intermediate temperature, as reproduced from Ref [164].

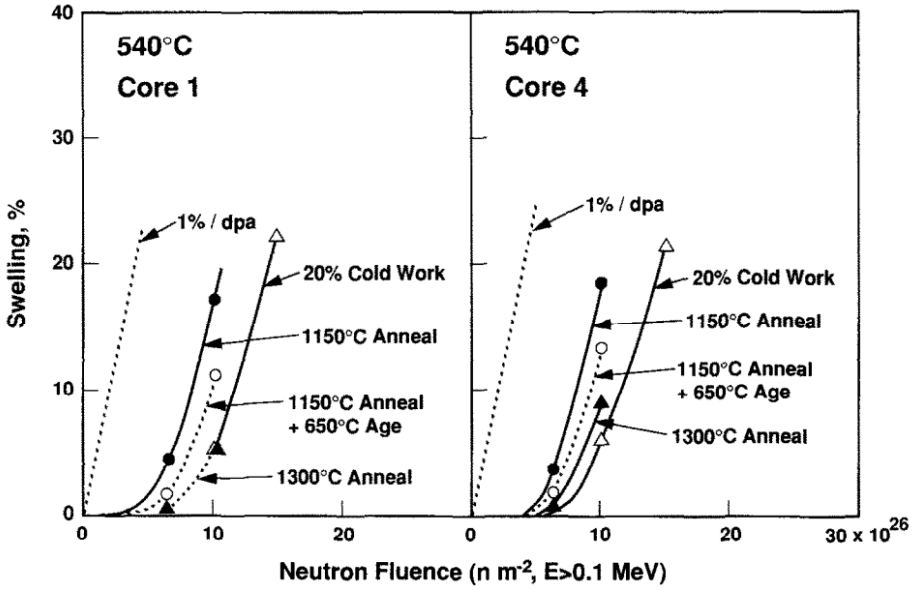

Figure 6.2 Void swelling behavior under neutron irradiation at 540 ˚C for a series of SS316 steels after different thermo-mechanical treatment, as reproduced from Ref [166]. Note that while the swelling rate is ~1%/dpa for all the alloys, incubation dose varies.

For nuclear energy applications, it is desirable to have materials with large incubation dose, small swelling rate and a peak swelling temperature outside the operation temperature window of the nuclear reactor. However, from the ion irradiation study in this work, we can only specify that the incubation dose for void swelling of NiFeMnCr HEA is larger than 10dpa (for the relatively high dose rate of the Ni ion irradiation), but we can not pinpoint its exact value. Similarly, the swelling rate and peak swelling temperature are not characterized in the present study due to the lack of any visible voids. Higher temperature (>700 ˚C) and higher dose (>10dpa) heavy ion irradiation study is needed to evaluate the void swelling resistance of this HEA at additional irradiation conditions. In particular, previous fast neutron irradiation studies on austenitic Fe-Cr-Ni alloys found that increasing solute content (i.e. fixed Cr and increasing Ni concentration) not only postponed the onset of void growth, but also reduced the swelling rate at the void growth stage[167]. Since both a solute effect and chemical disorder effect are present in NiFeMnCr HEA, comparison between HEA and concentrated Fe-Ni-Cr alloys can provide crucial insights on the role of chemical disorder on void nucleation and growth.

In addition to high temperature, high dose ion irradiation experiments for NiFeMnCr HEA, it would also be valuable to perform a parallel ion irradiation study of HEAs of similar chemical compositions. The *ab initio* calculation of vacancy energetics in Chapter 4 shows that HEAs with same number of elements can have different vacancy formation/migration energy statistics due to change in chemical composition (i.e. replace Mn with Co). Since defect properties are closely related with radiation effects, the role of specific chemical composition may be as important as that of chemical disorder in determining the radiation effects of HEA. A parallel ion radiation study of NiFeMnCr and NiFeCoCr HEAs could provide important insights on the role of chemical composition in the radiation effects of HEA. Finally, we also note the need to perform duel-ion beam studies to investigate whether co-implanted He markedly speeds up the void nucleation process in HEAs as typically occurs in conventional alloys[168, 169].

6.2 Probing preferred atomic arrangement in HEA

In Chapter 3, the inferred connection between electrical resistivity and local atomic re-arrangement was solely based on the indirect deduction from several pieces of experimental observations. While the ratio between high momentum fraction and low momentum fraction in the S-W plot does contain chemical environment information around the positron annihilation sites, the chemical information is a complex convolution of both positron affinity and defect microstructure. Since the positron affinity is different for all four alloying elements, and the defect microstructure is also evolving during the annealing process, change in the momentum ratio alone in S-W plots cannot be a direct measure of chemical ordering, and thus provides little detailed information on the chemical ordering near the annihilation sites.

On the other hand, a refined analysis of the orbital electron momentum spectrum (OEMS), such as normalized OEMS[170] could provide additional insight. This technique normalizes the whole momentum distribution with respect to that of a pure metal reference, such as Fe, and thus obtains more information than a single ratio in an S-W plot. Since positrons mainly interact with delocalized valence electrons at vacancies or vacancy clusters, the low momentum portion of the normalized OEMS is related with positron trapping and annihilation in vacancy-type defects. On the other hand, since positrons interact with primarily 3d electrons in Fe-series transition metals and the 3d electron configurations are unique for each 3d element, the peak shape within the high momentum part of the spectrum can provide information on the annihilation events for a specific element. Therefore, the change of peak shape can provide element-specific information on the chemical environment at the annihilation sites.

One other approach to directly measure the local atomic arrangement is through neutron scattering. Different from XRD and electron microscopy, neutrons scatter with the atomic nucleus instead of electrons, and thus neutron scattering is an effective tool to characterize the SRO of 3d transition metals[13], particularly since these metals have very similar electron scattering factors which impedes detailed characterization using x-ray scattering. Neutron scattering has been used to investigate the short-range order in a variety of single-phase solid solution alloys, including NiCoCr[114], FeNiCoCr[13, 171], ZrNbHf[172] and TaNbHfZr[173]. However, within these studies on HEAs, very limited work has been performed on how heat treatment would affect SRO, and none has investigated the effect of irradiation on SRO. The pair distribution functions (PDFs) obtained from neutron scattering for the un-irradiated control, as-irradiated and annealed FeNiCrMn HEA could provide direct evidence on the change in preferred atomic arrangements after low temperature neutron irradiation and after subsequent 700 ˚C annealing. Together with the data from normalized OEMS, the correlation between electrical resistivity and preferred atomic arrangements in HEA could be further clarified.

Similar to the ion irradiation study proposed in section 6.1, it is thus suggested to study the preferred atomic arrangement by conducting a parallel characterization of NiFeMnCr and FeNiCoCr HEAs to investigate the effect of chemical composition. Although neutron irradiation is not preferable to alter SRO in Co-containing HEAs due to high-induced radioactivity concerns, thermo-mechanical treatment can be an alternate pathway. It would be useful to measure the electrical resistivity of these two HEAs after different heat treatment. For example, quenching after a series of annealing temperature. If a change in resistivity is observed, a neutron scattering experiment could be performed to provide more details in the change of SRO.

6.3 Point defect thermodynamics in HEAs: interstitial formation and vacancy binding

Additional work to evaluate the formation energy of interstitials would be valuable in order to improve the understanding of point defect thermodynamics. However, it is important to emphasize that evaluation of the self-interstitial atom formation energy distribution in NiFeMnCr is more complex than that of vacancies. An explanation can be made based on the nature of vacancy and interstitial formation process: When an atom is removed in the vacancy formation process, the removed atom, whether it is Fe or Cr, can no longer exert any influence on the material system. However, when an atom is inserted to form an interstitial dumbbell, the direction-dependent stress field around the defect is strongly affected by the type of inserted atom as well as the crystallographic orientation. Thus, the statistical distribution of the interstitial formation energies in NiFeMnCr is not only determined by the local chemical environment, but also by the chemical identify of the atom pairs that form the dumbbell defect. While the displacement field around a vacancy is generally isotropic, the atomic displacements surrounding the dumbbell are not isotropic. Therefore, the treatment of vacancy formation energy can not be directly translated to interstitial formation energy. A separate *ab initio* computation study is needed to determine the thermodynamically stable geometric configuration (presumably dumbbell) and the preferred alignment of interstitial dumbbells in NiFeCrMn, statistically sample the formation energies formed by different atoms and for different local environments, and finally quantify the statistical distributions. The results would not only provide information on the preferred chemical composition and alignment of interstitial dumbbells in NiFeCrMn, but would also provide a foundation for the development and validation of multi-component EAM potentials for MD simulation of defect formation and evolution.

The fact that the defect energetics involve a statistical distribution may change important defect physical properties that are related with radiation effects. In the discussion of the PALS results in Chapter 3, the possible correlation between the distribution of vacancy binding energies and vacancy cluster thermal stability was discussed. Here, from the standpoint of vacancy and interstitial formation energy distribution, another question can be raised: How does the spontaneous recombination volume vary? As shown in Figure 6.3, this recombination volume determines the range for a vacancy and interstitial to spontaneously recombine without thermally-activated migration process. While both a vacancy and interstitial are involved in the spontaneous recombination process, the volume is primarily determined by the interstitial because interstitials have a much larger relaxation volume than vacancies and induce longer-range stress field in the crystal lattice. While the recombination volume is basically one value for typical metal and conventional dilute alloys, it is reasonable to expect that there are a variety of recombination volumes in HEAs due to their concentrated solute configurations and its fluctuation range is dependent upon the interstitial formation energy distribution. Interstitials with larger formation energy should have a larger recombination volume, and vice versa. The recombination volume directly affects low temperature defect

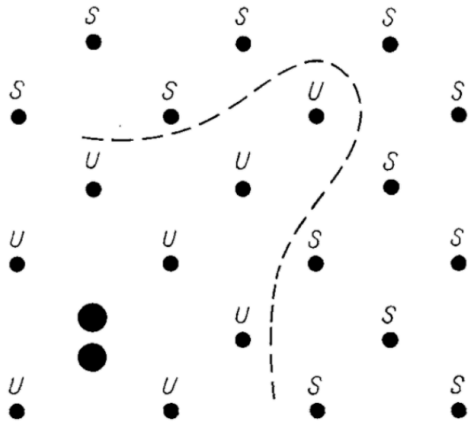

Figure 6.3 Schematic view of spontaneous recombination volume, as reproduced from Ref [174]. "U" and "S" stands for unstable and stable lattice sites, respectively. A vacancy formed at the lattice sites within the spontaneous recombination volume indicated by the dashed line will annihilate with the interstitial dumbbell without thermally activated diffusion.

accumulation (below temperature regime for thermally activated recombination processes) in which the dose dependence can be generally described by a standard rate theory analysis[175]:

$$C = \frac{1}{2v_0}(1 - e^{-2v_0 Pt}), \quad \text{(Eq 6.1)}$$

where C is the point defect concentration, v_0 is the recombination volume and Pt is the cumulative damage production (dpa) at a given time t. This equation shows that a larger recombination volume v_0 causes a lower defect concentration C. Qualitatively similar correlations between recombination volume and defect accumulation (in the form of clusters such as dislocation loops, etc.) are also relevant for elevated temperature irradiations that are important for energy applications. Computation of the interstitial formation energy distribution would also reveal any difference between recombination volumes of NiFeMnCr HEA and conventional alloys.

6.4 Point defect kinetics in HEAs: vacancy-mediated diffusion

The ordered sequence of migration barriers for atomic migration is generally explained by the relative size of solute atoms with respective to the matrix solvent atoms near the defect. However, in Chapter 4 it was pointed out that this particular sequence is different for Fe, Cr and Ni in NiFeMnCr HEA, and the conventional solute size theory does not apply to HEA anymore since there is no dominant matrix solvent element. A new methodology is needed to understand the relationship between atomic size and migration barrier height. Since the size of an atom is reflected by the stress field around that atom,

computing the atomic level stress in HEAs, which has been recently investigated by Egami et al[27, 28], can be a promising pathway to pursue for future work.

Near the end of the Chapter 4 discussion, it was mentioned that a simulation of the long range transport of a single vacancy is required to verify if the calculated large spread of migration barriers leads to sluggish diffusion or faster diffusion. To accomplish that, the first step would be to expand the current vacancy migration energy database to include more local chemical environments. The next critical challenge would be to find the correlation between migration barrier height and chemical environment. Local cluster expansion was previously used to resolve the dependence of migration energy on local chemical ordering in a binary alloy system[176]. However, this method has been so far only applied for binary systems[177-179] so it remains unknown if the methodology works for more complex systems. One other approach is to use the database as the training dataset for generic algorithms[180]. Once a certain migration energy barrier can be assigned to the corresponding local chemical environment with acceptable accuracy, KMC modeling can be implemented to track the physical process of single vacancy diffusion and compute the diffusivity of single vacancies.

6.5 Conclusions

In summary, this study characterized the radiation effects of both neutron and ion irradiated NiFeMnCr HEA through a comprehensive set if experimental techniques, and also modeled the vacancy defect properties through several *ab initio* techniques to establish the foundations for modeling radiation effects in multi-component, concentrated alloys and provide insights on reported unique radiation effects in HEA. The most significant research results include:

(1) NiFeMnCr has better radiation resistance upon heavy ion irradiation compared to conventional austenitic solid solution alloys. The alloy retains good phase stability at room temperature as well as 400 – 700 ˚C for irradiation doses in excess of 10 dpa. Compared with typical ~1% void swelling for conventional Fe-Cr-Ni alloys at similar elevated temperature irradiation conditions, no void formation was detected. While the radiation induced solute segregation trends for different elements at various temperatures are qualitatively similar to conventional alloys, the magnitude of solute segregation is suppressed in NiFeMnCr.

(2) Experimental observations are consistent with the proposed sluggish diffusion effect in HEA. NiFeMnCr has lower average defect cluster size and higher defect cluster density than conventional Fe-Cr-Ni alloys at 400 – 700 ˚C. Together with suppressed void swelling and RIS, these three experimental observations are consistent with reduced point defect diffusion for HEAs. However, we have not performed tracer diffusion or similar experiments to validate the existence of sluggish solute diffusion, and atomistic calculations of vacancy diffusion indicate a similar mean value for the vacancy diffusion

enthalpy (although with a significantly wider spread of energies compared to conventional alloys).

(3) NiFeMnCr retains fundamental phase stability after neutron irradiation. After room temperature irradiation from 0.1 to 1 dpa, the alloy remains single phase and has comparable mechanical performance as neutron irradiated SS316. Significant increase in yield strength and decrease in work hardening are observed after 0.1 and 1dpa irradiation. Large reduction of ductility is also observed, but the alloy still maintains >5% uniform elongation after 1dpa irradiation. Change in hardness qualitatively matches the change in tensile strength. Similarly, after heavy ion irradiation to doses in excess of 10 dpa at 400-700˚C there is no evidence for precipitation based on TEM and XRD examination.

(4) Collective evidence from the different experimental characterization techniques on neutron irradiated NiFeMnCr appear consistent with a radiation induced modification to the short range chemical ordering. In addition to radiation induced defect clusters, this change in short range chemical ordering may be critical for the understanding radiation effects in HEAs. Electrical resistivity measurement for as-irradiated HEAs shows that neutron irradiation induce a large resistivity change (>10 μΩ·cm). On the other hand, PIE after isochronal annealing shows that while most irradiation-induced defects anneal out, the change in electrical resistivity does not anneal out up to 700 ˚C, implying possible short range ordering effects during neutron irradiation process.

(5) This study establishes a feasible pathway to investigate the defect properties in NiFeMnCr HEA with respect to both magnetic and chemical disorder. The alloy is found to behave as paramagnetic material based on both experimental measurements and Monte Carlo modeling of magnetic susceptibility. DLM theory also reveals that local magnetic moment effects are not significant, further validating that magnetic interaction is not as important as chemical disordering in this alloy. As well, an efficient method to compute the chemical potential is proposed, implemented and validated, which is of fundamental importance for defect formation energy calculations.

(6) The statistical distribution of vacancy energetics has been evaluated. The statistical distribution of the vacancy formation energy is weakly dependent upon both the chemical species of the vacant site and the local chemical environment. For vacancy migration energy, the migration barrier height shows a large spread, from 0.55 to 1.68eV. The migration barrier height seems to be independent upon whether the local environment is uniform or biased around the vacancy. Finally, Fe has a higher occurring frequency of large migration barriers than the other three composing elements of the investigated HEA.

(7) Comparison is made between vacancy energetics from this alloy and those from pure metals, conventional alloys and HEAs of similar composition. For the vacancy formation energy, it appears that the increasing spread of the statistical distribution increases as the alloy composition becomes more concentrated and complex. The average formation

energy in HEA is slightly larger than the vacancy formation energy of pure Ni, and comparable to the average vacancy formation energy of an Fe-10Ni-20Cr alloy. Comparing with a NiFeCoCr HEA, the spread and average value of the vacancy formation energy is similar. For the migration energy, the migration barrier height sequence of FeNiMnCr (Fe > Ni > Cr) is different from either conventional austenitic Fe-Ni-Cr alloys or NiFeCoCr HEA (both are Ni > Fe > Cr). Furthermore, comparing with NiFeCoCr HEA, the width of the migration energy barrier statistical distribution is similar, but the magnitude of the migration barrier distribution is slightly higher.

(8) Calculations of the positron lifetime have been performed to facilitate interpretation of PALS measurements. In the NiFeMnCr HEA, the bulk positron lifetime does not appear to be sensitive to SRO, although the calculated single vacancy lifetime is affected by vacancy formation energy as well as the local chemical ordering. The geometrical configuration of vacancy clusters is shown to have a large effect on the calculated positron lifetime, in addition to the chemical ordering. Compared with Cr and Fe, the computed bulk and single vacancy positron lifetimes of NiFeMnCr HEA are closest to those of Ni.

LIST OF REFERENCES

1. S. Chu and A. Majumdar, Nature **488** (7411), 294-303 (2012).
2. S. J. Zinkle and G. S. Was, Acta Materialia **61** (3), 735-758 (2013).
3. S. J. Zinkle, K. A. Terrani and L. L. Snead, Current Opinion in Solid State and Materials Science **20** (6), 401-410 (2016).
4. S. J. Zinkle, in *Structural Materials for Generation IV Nuclear Reactors* (Woodhead Publishing, 2017), pp. 569-594.
5. L. K. Mansur and E. H. Lee, Journal of Nuclear Materials **179-181**, 105-110 (1991).
6. J. W. Yeh, S. K. Chen, S. J. Lin, J. Y. Gan, T. S. Chin, T. T. Shun, C. H. Tsau and S. Y. Chang, Advanced Engineering Materials **6** (5), 299-303 (2004).
7. B. Cantor, I. T. H. Chang, P. Knight and A. J. B. Vincent, Materials Science and Engineering a-Structural Materials Properties Microstructure and Processing **375**, 213-218 (2004).
8. O. N. Senkov, J. D. Miller, D. B. Miracle and C. Woodward, Nature Communications **6**, 10 (2015).
9. M. C. Troparevsky, J. R. Morris, P. R. C. Kent, A. R. Lupini and G. M. Stocks, Physical Review X **5** (1), 6 (2015).
10. F. Otto, Y. Yang, H. Bei and E. P. George, Acta Materialia **61** (7), 2628-2638 (2013).
11. D. B. Miracle, Materials Science and Technology **31** (10), 1142-1147 (2015).
12. D. C. Ma, B. Grabowski, F. Kormann, J. Neugebauer and D. Raabe, Acta Materialia **100**, 90-97 (2015).
13. M. S. Lucas, G. B. Wilks, L. Mauger, J. A. Munoz, O. N. Senkov, E. Michel, J. Horwath, S. L. Semiatin, M. B. Stone, D. L. Abernathy and E. Karapetrova, Applied Physics Letters **100** (25), 4 (2012).
14. Z. Wu, H. Bei, F. Otto, G. M. Pharr and E. P. George, Intermetallics **46**, 131-140 (2014).
15. O. N. Senkov, G. B. Wilks, J. M. Scott and D. B. Miracle, Intermetallics **19** (5), 698-706 (2011).
16. B. Zhang, M. C. Gao, Y. Zhang, S. Yang and S. M. Guo, Materials Science and Technology **31** (10), 1207-1213 (2015).
17. M. C. Gao, B. Zhang, S. M. Guo, J. W. Qiao and J. A. Hawk, Metallurgical and Materials Transactions a-Physical Metallurgy and Materials Science **47A** (7), 3322-3332 (2016).
18. C. J. Tong, Y. L. Chen, S. K. Chen, J. W. Yeh, T. T. Shun, C. H. Tsau, S. J. Lin and S. Y. Chang, Metallurgical and Materials Transactions a-Physical Metallurgy and Materials Science **36A** (4), 881-893 (2005).
19. J. W. Yeh, Jom **67** (10), 2254-2261 (2015).
20. Y. Zhang, T. T. Zuo, Z. Tang, M. C. Gao, K. A. Dahmen, P. K. Liaw and Z. P. Lu, Progress in Materials Science **61**, 1-93 (2014).
21. K. Y. Tsai, M. H. Tsai and J. W. Yeh, Acta Materialia **61** (13), 4887-4897 (2013).
22. S. Y. Chang and D. S. Chen, Applied Physics Letters **94** (23), 3 (2009).
23. M. H. Tsai, J. W. Yeh and J. Y. Gan, Thin Solid Films **516** (16), 5527-5530 (2008).

24. C. Lee, National Tsing Hua University, 2013.
25. W. Guo, W. Dmowski, J. Y. Noh, P. Rack, P. K. Liaw and T. Egami, Metallurgical and Materials Transactions a-Physical Metallurgy and Materials Science **44A** (5), 1994-1997 (2013).
26. A. J. Zaddach, C. Niu, C. C. Koch and D. L. Irving, Jom **65** (12), 1780-1789 (2013).
27. T. Egami, M. Ojha, O. Khorgolkhuu, D. M. Nicholson and G. M. Stocks, Jom **67** (10), 2345-2349 (2015).
28. T. Egami, W. Guo, P. D. Rack and T. Nagase, Metallurgical and Materials Transactions a-Physical Metallurgy and Materials Science **45A** (1), 180-183 (2014).
29. T. Nagase, P. D. Rack, J. H. Noh and T. Egami, Intermetallics **59**, 32-42 (2015).
30. G. S. Was, *Fundamentals of Radiation Materials Science: Metals and Alloys*. (Springer, 2007).
31. S. J. Zinkle and N. M. Ghoniem, Fusion Engineering and Design **51-52**, 55-71 (2000).
32. S. J. Zinkle and L. L. Snead, in *Annual Review of Materials Research, Vol 44*, edited by D. R. Clarke (Annual Reviews, Palo Alto, 2014), Vol. 44, pp. 241-267.
33. Y. Zhang, G. M. Stocks, K. Jin, C. Lu, H. Bei, B. C. Sales, L. Wang, L. K. Beland, R. E. Stoller, G. D. Samolyuk, M. Caro, A. Caro and W. J. Weber, Nature communications **6**, 8736 (2015).
34. G. D. Samolyuk, L. K. Beland, G. M. Stocks and R. E. Stoller, Journal of Physics-Condensed Matter **28** (17) (2016).
35. A. Caro, A. A. Correa, A. Tamm, G. D. Samolyuk and G. M. Stocks, Physical Review B **92** (14) (2015).
36. F. Gao, D. J. Bacon, P. E. J. Flewitt and T. A. Lewis, Modelling and Simulation in Materials Science and Engineering **6** (5), 543 (1998).
37. M. W. Finnis, P. Agnew and A. J. E. Foreman, Physical Review B **44** (2), 567-574 (1991).
38. R. S. Seth and S. B. Woods, Physical Review B **2** (8), 2961-2972 (1970).
39. J. H. Mooij, physica status solidi (a) **17** (2), 521-530 (2006).
40. K. Schroder, (1983).
41. D. S. Aidhy, C. Lu, K. Jin, H. Bei, Y. Zhang, L. Wang and W. J. Weber, Acta Materialia **99**, 69-76 (2015).
42. M. W. Ullah, D. S. Aidhy, Y. W. Zhang and W. J. Weber, Acta Materialia **109**, 17-22 (2016).
43. C. Y. Lu, K. Jin, L. K. Beland, F. F. Zhang, T. N. Yang, L. Qiao, Y. W. Zhang, H. B. Bei, H. M. Christen, R. E. Stoller and L. M. Wang, Scientific Reports **6**, 10 (2016).
44. K. Jin, C. Lu, L. M. Wang, J. Qu, W. J. Weber, Y. Zhang and H. Bei, Scripta Materialia **119**, 65-70 (2016).
45. C. Lu, L. Niu, N. Chen, K. Jin, T. Yang, P. Xiu, Y. Zhang, F. Gao, H. Bei, S. Shi, M.-R. He, I. M. Robertson, W. J. Weber and L. Wang, Nature Communications **7** (2016).
46. N. Kumar, C. Li, K. J. Leonard, H. Bei and S. J. Zinkle, Acta Materialia **113**, 230-244 (2016).

47. T. Yang, S. Xia, W. Guo, R. Hu, J. D. Poplawsky, G. Sha, Y. Fang, Z. Yan, C. Wang, C. Li, Y. Zhang, S. J. Zinkle and Y. Wang, Scripta Materialia **144** (Supplement C), 31-35 (2018).
48. W. G. Wolfer, in *Comprehensive Nuclear Material* (Elsevier, 2012), Vol. 1.01, pp. 1.
49. C. Lu, T. Yang, K. Jin, N. Gao, P. Xiu, Y. Zhang, F. Gao, H. Bei, W. J. Weber, K. Sun, Y. Dong and L. Wang, Acta Materialia **127**, 98-107 (2017).
50. M.-R. He, S. Wang, S. Shi, K. Jin, H. Bei, K. Yasuda, S. Matsumura, K. Higashida and I. M. Robertson, Acta Materialia **126**, 182-193 (2017).
51. M.-R. He, S. Wang, K. Jin, H. Bei, K. Yasuda, S. Matsumura, K. Higashida and I. M. Robertson, Scripta Materialia **125**, 5-9 (2016).
52. S. Zhao, Y. Osetsky and Y. Zhang, Acta Materialia **128** (Supplement C), 391-399 (2017).
53. F. Granberg, K. Nordlund, M. W. Ullah, K. Jin, C. Lu, H. Bei, L. M. Wang, F. Djurabekova, W. J. Weber and Y. Zhang, Physical Review Letters **116** (13), 135504 (2016).
54. S. J. Zhao, G. M. Stocks and Y. W. Zhang, Phys. Chem. Chem. Phys. **18** (34), 24043-24056 (2016).
55. Z. Wu and H. Bei, Materials Science and Engineering a-Structural Materials Properties Microstructure and Processing **640**, 217-224 (2015).
56. Y. Zhang, S. Zhao, W. J. Weber, K. Nordlund, F. Granberg and F. Djurabekova, Current Opinion in Solid State and Materials Science **21** (5), 221-237 (2017).
57. B. D. Wirth, G. R. Odette, J. Marian, L. Ventelon, J. A. Young-Vandersall and L. A. Zepeda-Ruiz, Journal of Nuclear Materials **329-333** (Part A), 103-111 (2004).
58. E. Getto, Z. Jiao, A. M. Monterrosa, K. Sun and G. S. Was, Journal of Nuclear Materials **465**, 116-126 (2015).
59. X. Wang, A. M. Monterrosa, F. Zhang, H. Huang, Q. Yan, Z. Jiao, G. S. Was and L. Wang, Journal of Nuclear Materials **462**, 119-125 (2015).
60. J. B. Whitley, P. Wilkes, G. L. Kulcinski and H. V. Smith, Journal of Nuclear Materials **79** (1), 159-169 (1979).
61. S. J. Zinkle and L. L. Snead, Scripta Materialia **143**, 154-160 (2018).
62. L. K. Mansur, Journal of Nuclear Materials **216**, 97-123 (1994).
63. N. H. Packan, K. Farrell and J. O. Stiegler, Journal of Nuclear Materials **78** (1), 143-155 (1978).
64. R. E. Stoller, M. B. Toloczko, G. S. Was, A. G. Certain, S. Dwaraknath and F. A. Garner, Nuclear Instruments & Methods in Physics Research Section B-Beam Interactions with Materials and Atoms **310**, 75-80 (2013).
65. N. Ghoniem and G. L. Kulcinski, Journal of Nuclear Materials **69-7** (1-2), 816-820 (1978).
66. J. M. Sanchez, F. Ducastelle and D. Gratias, Physica A **128** (1-2), 334-350 (1984).
67. G. S. Was, J. P. Wharry, B. Frisbie, B. D. Wirth, D. Morgan, J. D. Tucker and T. R. Allen, Journal of Nuclear Materials **411** (1-3), 41-50 (2011).

68. T. R. Allen, J. T. Busby, G. S. Was and E. A. Kenik, Journal of Nuclear Materials **255** (1), 44-58 (1998).
69. A. J. Ardell and P. Bellon, Current Opinion in Solid State and Materials Science **20** (3), 115-139 (2016).
70. A. Etienne, B. Radiguet, N. J. Cunningham, G. R. Odette, R. Valiev and P. Pareige, Ultramicroscopy **111** (6), 659-663 (2011).
71. L. E. Samuels and T. O. Mulhearn, Journal of the Mechanics and Physics of Solids **5** (2), 125-134 (1957).
72. S. J. Zinkle and W. C. Oliver, Journal of Nuclear Materials **141-143**, 548-552 (1986).
73. W. D. Nix and H. J. Gao, Journal of the Mechanics and Physics of Solids **46** (3), 411-425 (1998).
74. H. R. Higgy and F. H. Hammad, Journal of Nuclear Materials **55** (2), 177-186 (1975).
75. J. R. Cahoon, W. H. Broughton and A. R. Kutzak, Metallurgical Transactions **2** (7), 1979-1983 (1971).
76. J. T. Busby, M. C. Hash and G. S. Was, Journal of Nuclear Materials **336** (2-3), 267-278 (2005).
77. S. J. Zinkle and Y. Matsukawa, Journal of Nuclear Materials **329-333** (Part A), 88-96 (2004).
78. G. E. Lucas, Journal of Nuclear Materials **206** (2), 287-305 (1993).
79. X. Hu, D. Xu and B. D. Wirth, Journal of Nuclear Materials **442** (1, Supplement 1), S649-S654 (2013).
80. M. Eldrup and B. N. Singh, Journal of Nuclear Materials **251**, 132-138 (1997).
81. M. Eldrup and B. N. Singh, Journal of Nuclear Materials **276**, 269-277 (2000).
82. P. Asoka-Kumar, J. Hartley, R. Howell, P. A. Sterne and T. G. Nieh, Applied Physics Letters **77** (13), 1973-1975 (2000).
83. X. Hu, T. Koyanagi, Y. Katoh and B. D. Wirth, Physical Review B **95** (10), 104103 (2017).
84. X. Hu, T. Koyanagi, M. Fukuda, Y. Katoh, L. L. Snead and B. D. Wirth, Journal of Nuclear Materials **470** (Supplement C), 278-289 (2016).
85. M. Horiki and M. Kiritani, Journal of Nuclear Materials **239** (1-3), 34-41 (1996).
86. T. S. Byun and K. Farrell, Acta Materialia **52** (6), 1597-1608 (2004).
87. K. Farrell, T. S. Byun and N. Hashimoto, Journal of Nuclear Materials **335** (3), 471-486 (2004).
88. J. E. Pawel, A. F. Rowcliffe, G. E. Lucas and S. J. Zinkle, Journal of Nuclear Materials **239**, 126-131 (1996).
89. N. Hashimoto, T. S. Byun and K. Farrell, Journal of Nuclear Materials **351** (1), 295-302 (2006).
90. D. Tabor, British Journal of Applied Physics **7** (5), 159-166 (1956).
91. A. Vehanen, P. Hautojarvi, J. Johansson, J. Ylikauppila and P. Moser, Physical Review B **25** (2), 762-780 (1982).
92. M. Eldrup, O. E. Mogensen and J. H. Evans, Journal of Physics F-Metal Physics **6** (4), 499-& (1976).

93. J. W. Corbett, *Electron radiation damage in semiconductors and metals*. (Academic Press, 1966).
94. C. Dimitrov, M. Tenti and O. Dimitrov, Journal of Physics F-Metal Physics **11** (4), 753-765 (1981).
95. Y. N. Osetsky, D. J. Bacon, A. Serra, B. N. Singh and S. I. Golubov, Journal of Nuclear Materials **276** (1), 65-77 (2000).
96. K. Durst, B. Backes and M. Göken, Scripta Materialia **52** (11), 1093-1097 (2005).
97. D. L. Krumwiede, T. Yamamoto, T. A. Saleh, S. A. Maloy, G. R. Odette and P. Hosemann, Journal of Nuclear Materials **504**, 135-143 (2018).
98. J. R. Greer, W. C. Oliver and W. D. Nix, Acta Materialia **53** (6), 1821-1830 (2005).
99. C. A. Volkert and E. T. Lilleodden, Philos. Mag. **86** (33-35), 5567-5579 (2006).
100. C. Dimitrov, M. D. C. Belo and O. Dimitrov, Journal of Physics F-Metal Physics **10** (8), 1653-1664 (1980).
101. M. Nakagawa, Journal of Nuclear Materials **108-109**, 194-200 (1982).
102. R. C. Birtcher and T. H. Blewitt, Journal of Nuclear Materials **152** (2), 204-211 (1988).
103. O. Dimitrov and C. Dimitrov, Journal of Physics F-Metal Physics **16** (8), 969-980 (1986).
104. C. Dimitrov and O. Dimitrov, Journal of Physics F: Metal Physics **14** (4), 793 (1984).
105. A. Benkaddour, C. Dimitrov and O. Dimitrov, Journal of Nuclear Materials **217** (1), 118-126 (1994).
106. W. Schilling and K. Sonnenberg, Journal of Physics F: Metal Physics **3** (2), 322 (1973).
107. S. Takaki, J. Fuss, H. Kuglers, U. Dedek and H. Schultz, Radiation Effects **79** (1-4), 87-122 (1983).
108. M. Nakagawa, K. Böning, P. Rosner and G. Vogl, Physical Review B **16** (12), 5285-5302 (1977).
109. S. Zhao, G. Velisa, H. Xue, H. Bei, W. J. Weber and Y. Zhang, Acta Materialia **125**, 231-237 (2017).
110. T. M. Williams, Journal of Nuclear Materials **79** (1), 28-42 (1979).
111. O. Dimitrov and C. Dimitrov, Journal of Nuclear Materials **105** (1), 39-47 (1982).
112. C. Niu, A. J. Zaddach, A. A. Oni, X. Sang, J. W. Hurt, J. M. LeBeau, C. C. Koch and D. L. Irving, Applied Physics Letters **106** (16), 4 (2015).
113. A. Tamm, A. Aabloo, M. Klintenberg, M. Stocks and A. Caro, Acta Materialia **99**, 307-312 (2015).
114. F. X. Zhang, S. Zhao, K. Jin, H. Xue, G. Velisa, H. Bei, R. Huang, J. Y. P. Ko, D. C. Pagan, J. C. Neuefeind, W. J. Weber and Y. Zhang, Physical Review Letters **118** (20), 205501 (2017).
115. J. B. Piochaud, T. P. C. Klaver, G. Adjanor, P. Olsson, C. Domain and C. S. Becquart, Physical Review B **89** (2) (2014).
116. S. Choudhury, L. Barnard, J. D. Tucker, T. R. Allen, B. D. Wirth, M. Asta and D. Morgan, Journal of Nuclear Materials **411** (1-3), 1-14 (2011).

117. J. Marian, B. D. Wirth and J. M. Perlado, Physical Review Letters **88** (25), 255507 (2002).
118. H. F. Deng and D. J. Bacon, Physical Review B **53** (17), 11376-11387 (1996).
119. S. J. Zinkle, Phys. Scr. **T167**, 10 (2016).
120. G. M. Stocks, W. M. Temmerman and B. L. Gyorffy, Physical Review Letters **41** (5), 339-343 (1978).
121. J. S. Faulkner and G. M. Stocks, Physical Review B **21** (8), 3222-3244 (1980).
122. B. L. Gyorffy, A. J. Pindor, J. Staunton, G. M. Stocks and H. Winter, Journal of Physics F-Metal Physics **15** (6), 1337-1386 (1985).
123. A. Zunger, S. H. Wei, L. G. Ferreira and J. E. Bernard, Physical Review Letters **65** (3), 353-356 (1990).
124. A. van de Walle, P. Tiwary, M. de Jong, D. L. Olmsted, M. Asta, A. Dick, D. Shin, Y. Wang, L. Q. Chen and Z. K. Liu, Calphad-Computer Coupling of Phase Diagrams and Thermochemistry **42**, 13-18 (2013).
125. S. Zhao, W. J. Weber and Y. Zhang, JOM **69** (11), 2084-2091 (2017).
126. D. Hobbs, J. Hafner and D. Spisak, Physical Review B **68** (1) (2003).
127. G. Kresse and J. Furthmuller, Computational Materials Science **6** (1), 15-50 (1996).
128. G. Kresse and D. Joubert, Physical Review B **59** (3), 1758-1775 (1999).
129. J. P. Perdew, K. Burke and M. Ernzerhof, Physical Review Letters **77** (18), 3865-3868 (1996).
130. J. Yin, M. Eisenbach, D. M. Nicholson and A. Rusanu, Physical Review B **86** (21) (2012).
131. B. Widom, The Journal of Chemical Physics **39** (11), 2808-2812 (1963).
132. J. S. Wróbel, D. Nguyen-Manh, S. L. Dudarev and K. J. Kurzydłowski, Nuclear Instruments and Methods in Physics Research Section B: Beam Interactions with Materials and Atoms **393** (Supplement C), 126-129 (2017).
133. G. Henkelman, B. P. Uberuaga and H. Jonsson, Journal of Chemical Physics **113** (22), 9901-9904 (2000).
134. P. Haas, F. Tran and P. Blaha, Physical Review B **79** (8), 085104 (2009).
135. Y. Tateyama and T. Ohno, Physical Review B **67** (17), 174105 (2003).
136. R. Hafner, D. Spišák, R. Lorenz and J. Hafner, Physical Review B **65** (18), 184432 (2002).
137. W. M. Haynes, *CRC handbook of chemistry and physics*. (CRC press, 2014).
138. T. Yamada, N. Kunitomi, Y. Nakai, D. E. Cox and G. Shirane, Journal of the Physical Society of Japan **28** (3), 615-627 (1970).
139. Y. W. Zhang, K. Jin, H. Z. Xue, C. Y. Lu, R. J. Olsen, L. K. Beland, M. W. Ullah, S. J. Zhao, H. B. Bei, D. S. Aidhy, G. D. Samolyuk, L. M. Wang, M. Caro, A. Caro, G. M. Stocks, B. C. Larson, I. M. Robertson, A. A. Correa and W. J. Weber, Journal of Materials Research **31** (16), 2363-2375 (2016).
140. J. Staunton, B. L. Gyorffy, A. J. Pindor, G. M. Stocks and H. Winter, Journal of Magnetism and Magnetic Materials **45** (1), 15-22 (1984).
141. H. Akai and P. H. Dederichs, Physical Review B **47** (14), 8739-8747 (1993).

142. S. Zhao, T. Egami, G. M. Stocks and Y. Zhang, Physical Review Materials **2** (1), 013602 (2018).
143. S. C. Middleburgh, D. M. King, G. R. Lumpkin, M. Cortie and L. Edwards, Journal of Alloys and Compounds **599**, 179-182 (2014).
144. W. Chen, X. Ding, Y. Feng, X. Liu, K. Liu, Z. P. Lu, D. Li, Y. Li, C. T. Liu and X.-Q. Chen, Journal of Materials Science & Technology (2017).
145. T. P. C. Klaver, D. J. Hepburn and G. J. Ackland, Physical Review B **85** (17) (2012).
146. Z. Wang, C. T. Liu and P. Dou, Physical Review Materials **1** (4), 043601 (2017).
147. G. R. O. Y. Dai, in *Comprehensive Nuclear Materials*, edited by R. J. M. Konings (Elsevier, 2012), Vol. 1, pp. 141.
148. L. Malerba, G. J. Ackland, C. S. Becquart, G. Bonny, C. Domain, S. L. Dudarev, C. C. Fu, D. Hepburn, M. C. Marinica, P. Olsson, R. C. Pasianot, J. M. Raulot, F. Soisson, D. Terentyev, E. Vincent and F. Willaime, Journal of Nuclear Materials **406** (1), 7-18 (2010).
149. J. D. Tucker, R. Najafabadi, T. R. Allen and D. Morgan, Journal of Nuclear Materials **405** (3), 216-234 (2010).
150. P. A. Sterne and J. H. Kaiser, Physical Review B **43** (17), 13892-13898 (1991).
151. P. A. Sterne, J. E. Pask and B. M. Klein, Appl. Surf. Sci. **149** (1-4), 238-243 (1999).
152. J. P. Desclaux, Computer Physics Communications **1** (3), 216-222 (1970).
153. U. von Barth and L. Hedin, Journal of Physics C: Solid State Physics **5** (13), 1629 (1972).
154. J. P. Perdew and A. Zunger, Physical Review B **23** (10), 5048 (1981).
155. K. M. Flores, D. Suh, R. H. Dauskardt, P. Asoka-Kumar, P. A. Sterne and R. H. Howell, Journal of Materials Research **17** (5), 1153-1161 (2002).
156. B. Barbiellini, M. J. Puska, T. Korhonen, A. Harju, T. Torsti and R. M. Nieminen, Physical Review B **53** (24), 16201 (1996).
157. P. Giannozzi, S. Baroni, N. Bonini, M. Calandra, R. Car, C. Cavazzoni, D. Ceresoli, G. L. Chiarotti, M. Cococcioni and I. Dabo, Journal of physics: Condensed matter **21** (39), 395502 (2009).
158. J. E. Pask, B. M. Klein, C. Y. Fong and P. A. Sterne, Physical Review B **59** (19), 12352-12358 (1999).
159. J. M. C. Robles, E. Ogando and F. Plazaola, Journal of Physics-Condensed Matter **19** (17) (2007).
160. G. Brauer, W. Anwand, P. G. Coleman, A. P. Knights, F. Plazaola, Y. Pacaud, W. Skorupa, J. Stormer and P. Willutzki, Physical Review B **54** (5), 3084-3092 (1996).
161. J. Wiktor, X. Kerbiriou, G. Jomard, S. Esnouf, M.-F. Barthe and M. Bertolus, Physical Review B **89** (15) (2014).
162. T. Korhonen, M. J. Puska and R. M. Nieminen, Physical Review B **54** (21), 15016-15024 (1996).
163. O. Melikhova, J. Čížek, J. Kuriplach, I. Procházka, M. Cieslar, W. Anwand and G. Brauer, Intermetallics **18** (4), 592-598 (2010).
164. S. J. Zinkle and K. Farrell, Journal of Nuclear Materials **168** (3), 262-267 (1989).

165. L. Glowinski, C. Fiche and M. Lott, Journal of Nuclear Materials **47** (3), 295-310 (1973).
166. F. A. Garner, J. F. Bates and M. A. Mitchell, Journal of Nuclear Materials **189** (2), 201-209 (1992).
167. F. Garner, Journal of Nuclear Materials **122** (1-3), 459-471 (1984).
168. Y. Katoh, M. Ando and A. Kohyama, Journal of nuclear materials **323** (2-3), 251-262 (2003).
169. H. Ogiwara, H. Sakasegawa, H. Tanigawa, M. Ando, Y. Katoh and A. Kohyama, Journal of nuclear materials **307**, 299-303 (2002).
170. S. C. Glade, B. D. Wirth, G. R. Odette and P. Asoka-Kumar, Journal of Nuclear Materials **351** (1-3), 197-208 (2006).
171. U. Dahlborg, J. Cornide, M. Calvo-Dahlborg, T. Hansen, Z. Leong, L. Asensio Dominguez, S. Chambreland, A. Cunliffe, R. Goodall and I. Todd, Acta Physica Polonica, A. **128** (4) (2015).
172. W. Guo, W. Dmowski, J.-Y. Noh, P. Rack, P. K. Liaw and T. Egami, Metallurgical and Materials Transactions A **44** (5), 1994-1997 (2013).
173. S. Maiti and W. Steurer, Acta Materialia **106**, 87-97 (2016).
174. J. Gibson, A. N. Goland, M. Milgram and G. Vineyard, Physical Review **120** (4), 1229 (1960).
175. G. Lück and R. Sizmann, physica status solidi (b) **5** (3), 683-691 (1964).
176. A. Van der Ven, G. Ceder, M. Asta and P. D. Tepesch, Physical Review B **64** (18) (2001).
177. A. Van der Ven and G. Ceder, Physical Review Letters **94** (4), 4 (2005).
178. A. Van der Ven and G. Ceder, Physical Review B **71** (5) (2005).
179. A. A. Belak and A. Van der Ven, Physical Review B **91** (22) (2015).
180. H. Wu, A. Lorenson, B. Anderson, L. Witteman, H. Wu, B. Meredig and D. Morgan, Computational Materials Science **134** (Supplement C), 160-165 (2017).

VITA

Congyi Li received his B.S. in Nuclear Engineering and Radiological Science from University of Michigan in 2012. After that, he came to University of Tennessee, Knoxville (UTK) to pursue his PhD in Energy Science and Engineering with a concentration in Nuclear Energy. During his six years of graduate career at UTK, He was co-advised by Dr. Steve Zinkle and Dr. Brian Wirth to study radiation effects in novel alloys for structural applications in advanced nuclear power reactors. His PhD research project is to characterize and model radiation effects in a NiFeMnCr high entropy alloy (HEA) by integrating comprehensive experimental techniques and state-of-art modeling tools. His research is presented in multiple international conferences such as *TMS Annual Meeting & Exhibition*, *MRS Annual Meeting & Exhibition* and *International Conference on Fusion Reactor Materials*. His research is published in *U.S. Department of Energy Fusion Materials Semiannual Progress Reports, Acta Materialia,* and *Scripta Materialia*.